

Controlled Manipulation of Nanoparticles : Scanning  
Probe Measurements and Modelling of Trajectories  
and Dissipative Effects

Inauguraldissertation

zur

Erlangung der Würde eines Doktors der Philosophie  
vorgelegt der  
Philosophisch–Naturwissenschaftlichen Fakultät  
der Universität Basel

von

Akshata Rao  
aus Indien

Basel, 2011

Genehmigt von der Philosophisch-Naturwissenschaftlichen Fakultät  
auf Antrag von:

Prof. Dr. Ernst Meyer (Fakultätsverantwortlicher)

Dr. André Schirmeisen (Korreferent)

Dr. Enrico Gnecco (Experte)

Basel, den 08. December 2009

Prof. Dr. Eberhard Parlow  
Dekan



*To my parents*



# ABSTRACT

Unintentional displacement of tiny nanoparticles, while imaging them on a surface, is a common experience in atomic force microscopy (AFM). Understanding how to control and turn this effect into a powerful method for studying the mobility of nano-objects is the main objective of this thesis. This has several applications from fields ranging from environmental control to drug delivery, besides the fundamental interest in nanomechanics. Therefore, the starting point was the preparation of different kinds of nanoparticles on a variety of bare and treated substrates. Nanoparticles and/or agglomerates of nanoparticles were prepared on surfaces and characterized by AFM. The goal was to determine the shape, size and/or size distribution of nanoparticles and the influence of the surface chemistry and the morphology on the density of the particles. Besides the geometrical properties, attempts were made to determine the forces between nanoparticles and surfaces. For this purpose, a preparation process was developed to transfer and then characterize particles on sensors. Also, Kelvin force imaging was done on the samples of nanoparticles in order to determine the contact potential of the particles. Nanoparticles with important commercial applications for e.g.  $\text{TiO}_2$ ,  $\text{Al}_2\text{O}_3$ ,  $\text{SiO}_2$ ,  $\text{ZrO}_2$  and Au were used for this study.

The next part of the thesis focuses on the manipulation of Au nanoparticles. A new technique for controlled manipulation of nanospheres and asymmetric nanoparticles was developed in the course of the thesis. The pathway of the tip was related to the trajectories of the nanoparticles by an original collision model. In order to verify the model, experiments were done by manipulating gold nanospheres on bare and nano-patterned  $\text{SiO}_2$  surfaces in tapping-mode AFM. Detailed analysis of particle trajectories due to impact between the oscillating tip and particle (within one scan frame) was done. This model was then extended for studying the effect of friction on the trajectories of the nanospheres. Whenever the tip collides with the particle, the particle is displaced by a certain distance, which depends upon the friction force between the particle and the surface. Modeling was done to reproduce the trajectories of the nanoparticles at different values of friction. The fluctuations, (and the apparent discontinuities) of the trajectories of the nanoparticles were related to friction.

The effect of surface chemistry, temperature and environment on manipulation of the nanoparticles is discussed in the third chapter of the thesis. For these studies, manip-

ulation of Au nanoparticles either raw or coated with self-assembled monolayers ending with a hydrophobic (methyl, -CH<sub>3</sub>) or hydrophilic group (hydroxyl, -OH) was done to investigate the influence of the hydrophobicity of the coatings on the mobility of the nanoparticles. The role of the environment and thermal activation was studied by performing manipulation experiments in UHV and at different temperatures, ranging from 20 up to 150°C. By measuring the phase shift while scanning, the threshold value of the power dissipation needed for translating a single nanoparticle could be determined.

Lastly, the manipulation of asymmetric nanoparticles e.g. nanorods and flower shaped nanoparticles was done. The main objective was to study the effects of external torques on the motion of the nanoparticles. The collision model was extended to relate the rotational and translational motion of these asymmetric structures to the pathway of the probing tip. The trajectories of these particles were also simulated in this case. Corresponding, AFM experiments were done by manipulating Au nanorods on Si. To study the case of nanoflowers, antimony islands on HOPG were used.

In summary, preparation procedures for homogeneous nanoparticle samples are discussed. AFM was used to determine the geometric characteristics and adhesion forces of the nanoparticles. A new technique for controlled manipulation of nanoparticles was deduced for spherical and asymmetrical particles where the focus was to try to understand how to induce a well-defined direction of motion of the nanoparticles by adjusting the scan pattern. Also, the factors effecting the manipulation of nanoparticles were studied.

# Contents

<b>1 Atomic Force Microscopy: A tool for characterization and manipulation of nanoparticles</b>	<b>1</b>
1.1 Atomic Force Microscopy . . . . .	2
1.1.1 Contact Force microscopy . . . . .	3
1.1.2 Dynamic AFM . . . . .	3
1.1.3 Tapping mode force microscopy . . . . .	4
1.1.4 Phase imaging . . . . .	4
1.1.5 Kelvin probe force microscopy . . . . .	5
1.2 Relevant forces . . . . .	7
1.2.1 Van der Waals Forces . . . . .	7
1.2.2 Electrostatic Forces . . . . .	7
1.2.3 Capillary Forces . . . . .	8
1.2.4 Short-range forces . . . . .	9
1.3 How to measure energy dissipation in DFM . . . . .	9
1.4 AFM as a Nanomanipulator . . . . .	11
1.4.1 Feedback - off contact mode . . . . .	11
1.4.2 Feedback - on contact mode . . . . .	12
1.4.3 Manipulation by using electrostatic force . . . . .	12
1.4.4 Manipulation using Tapping mode AFM . . . . .	13
1.5 Discussions . . . . .	13



<b>2</b>	<b>Preparation and Characterization of nanoparticles</b>	<b>15</b>
2.1	Synthesis of nanoparticles . . . . .	16
2.1.1	Top-Down Approach . . . . .	16
2.1.2	Bottom-Up Approach . . . . .	17
2.2	Conventional methods of deposition . . . . .	20
2.2.1	Self assembly . . . . .	20
2.2.2	Dip coating . . . . .	20
2.2.3	Spin Coating . . . . .	21
2.2.4	Boil deposition . . . . .	22
2.2.5	Simple deposition . . . . .	22
2.3	Characterization of nanoparticles by AFM . . . . .	22
2.3.1	Substrates . . . . .	23
2.3.2	Instruments . . . . .	24
2.4	Experimental Results . . . . .	26
2.4.1	Preparation techniques for spherical nanoparticles . . . . .	26
2.4.2	Imaging nanospheres on different substrates . . . . .	27
2.4.3	Accurate determination of particle size . . . . .	31
2.5	Determination of the adhesion of nanoparticles . . . . .	33
2.6	Determination of the contact potential of nanoparticles . . . . .	35
2.6.1	Conclusions . . . . .	37
<b>3</b>	<b>Analytic relations between particle and probe trajectories in atomic force microscope nanomanipulation</b>	<b>39</b>
3.1	Manipulation of gold nanoparticles . . . . .	39
3.1.1	The Model . . . . .	40
3.1.2	Experimental Results . . . . .	45
3.1.3	Manipulation of a nanoparticle mixture . . . . .	51

---

3.1.4	Angle of deflection in case of zigzag scanning path . . . . .	52
3.2	Trajectory fluctuations accompanying the manipulation of spherical nanoparticles . . . . .	54
3.2.1	Simulations . . . . .	55
3.2.2	Experimental Results . . . . .	59
3.3	Conclusions . . . . .	60
<b>4</b>	<b>Manipulation of Gold Nanoparticles: Influence of Surface Chemistry, Temperature, and Environment</b>	<b>63</b>
4.1	Nanoparticles Used : Raw vs Functionalized nanoparticles . . . . .	63
4.2	Nanoparticle Adsorption : Random vs Geometrical organization . . . . .	65
4.3	Manipulation Setup : Air vs UHV . . . . .	66
4.4	Experimental Results . . . . .	66
4.4.1	Effect of surface chemistry on the manipulation of nanoparticles . . . . .	66
4.4.2	Temperature Effects . . . . .	69
4.4.3	Organization Effects . . . . .	70
4.4.4	Vacuum Effects . . . . .	70
4.5	Power dissipation : Moving vs Fixed nanoparticle . . . . .	72
4.6	Conclusion . . . . .	73
<b>5</b>	<b>Controlled Manipulation of asymmetric nanoparticles by Atomic Force Microscopy</b>	<b>75</b>
5.1	Manipulation of rigid gold nanorods . . . . .	75
5.1.1	The Model . . . . .	76
5.1.2	Experimental Results . . . . .	80
5.2	Manipulation of asymmetric “Nanoflowers” . . . . .	81
5.3	The Model . . . . .	81
5.3.1	Sample Preparation . . . . .	84
5.3.2	Experimental Results . . . . .	85

**6 Conclusions and Outlook****87**

# Chapter 1

## Atomic Force Microscopy: A tool for characterization and manipulation of nanoparticles

In this chapter, a brief introduction of the working principle of the atomic force microscopy (AFM) is given. Operation principle of the AFM in different modes is discussed. A brief review of manipulation of nanoparticles by AFM is given.

### Historical background of Scanning Probe Microscopy

The world of scanning probe microscopy (SPM) was opened by the invention of the scanning tunneling microscope (STM) in 1982 by G. Binnig and H. Rohrer [1, 2]. They were awarded the Nobel prize in 1986. In the STM, a sharp needle is scanned over the surface at a distance of less than 1 nm. This distance is controlled by the tunneling current between the tip and the conducting surface. The tunneling current is a quantum mechanical effect, with two properties important for STM - it flows between two electrodes through a thin insulator or a vacuum gap, and it decays on the length scale of one atomic radius. In the STM the tunneling current flows from the very last atom of the tip apex to single atoms at the surface, providing atomic resolution. In 1983, Binnig and Rohrer presented Si(111)  $7 \times 7$  surface reconstruction with atomic resolution. They also presented the first metal surfaces, the Au(110)  $2 \times 1$  and Au(110)  $3 \times 1$  reconstructions. However, the first atomic resolution of a close-packed metal was presented by Hallmark *et al.* [9]. In spite of these advantages, the main drawback of the STM was that its use is restricted to conducting surfaces. Most of the conductors, except HOPG and few others, are not suitable to examine in ambient conditions since they change frequently in time due to adsorption and oxidation. Therefore, the measurements have to be performed in UHV conditions where the sample-surfaces can be cleaned and kept in a defined state for several hours.

This drawback was overcome by the invention of the scanning force microscope (SFM), which is the first and most important extension of the STM, invented in 1986 by Binnig, Quate and Gerber[3]. In this instrument, the tip height is controlled in such a way that the force between the tip and the sample is constant. Based on the assumption that forces between the atoms at the tip apex and the atoms of the surface determine the resolution of this instrument, it is commonly called the atomic force microscope (AFM). The AFM offers visualization in 3D with a lateral resolution from hundreds of nanometers to the picometer range. Surfaces of solids can be mapped with atomic resolution, revealing not only the structure of perfect crystalline surfaces but also the distribution of point defects, adsorbates and structural defects [9]. The family of scanning force microscopy has several other members, based on measurements of other quantities, i.e. electric and magnetic properties of surfaces, friction forces, and chemical potentials. In addition to imaging surfaces STM and AFM give the opportunity to manipulate atoms, molecules and nanoparticles etc in a controlled manner and perform various types of spectroscopy. With the invention of these new types of microscopes the doors to study all kinds of phenomena on the nanometer scale have been opened, and tremendous progress has been achieved in nanoscience.

## 1.1 Atomic Force Microscopy

The basic concept of force microscopy is the measurement of forces between a sharp tip and a sample surface. Most commonly, the tip is mounted on the end of the cantilever which serves as a force sensor. Either the static deflection of the cantilever or the change in its dynamic properties due to tip-sample forces can be exploited. There are different techniques to detect the small bending of the cantilever due to tip-sample forces. Most instruments use the beam deflection method. A light beam is reflected at the rear side of the cantilever and the deflection is monitored by a position-sensitive photodiode (see fig. 1.1 )

### Operation modes in force microscopy

Several modes of operation have been introduced in force microscopy, with a variety of names describing their characteristic features. The operational modes can be divided into static and dynamic modes, where the static bending of the cantilever or its dynamic properties are measured, respectively. The operation modes are often distinguished with respect to whether the tip is in contact with the surface or not. For dynamic modes however, the tip may be temporarily in contact during each oscillation cycle.

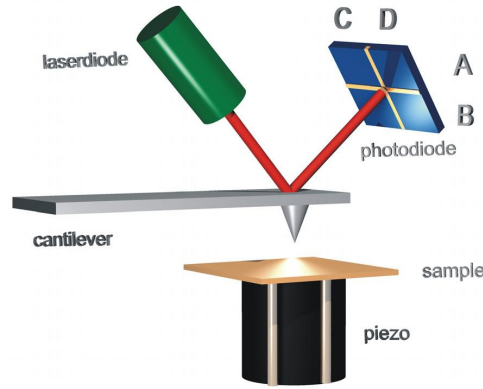


**Figure 1.1:** Principle of the beam deflection method

### 1.1.1 Contact Force microscopy

Contact force microscopy is based upon static measurement of deflection of the cantilever. Topographic images are recorded by scanning the tip over the sample surface at constant cantilever deflection. The deflection corresponds to a normal force which can be calculated by multiplying with the spring constant. In this mode of operation, the probing tip is brought into the repulsive force regime. The net force on the cantilever must be zero if the cantilever deflection stays constant at  $z$  (positive for an upward deflection and negative for a downward deflection) in contact with the sample. The total force on the cantilever is a sum of the restoring force  $F_k$ ,  $F_k = -kz$ , where  $k$  is the cantilever spring constant. From this it is easy to understand that a small value of  $k$  increases the force sensitivity. Instabilities are likely to occur due to the use of low  $k$  cantilevers. In the contact mode the cantilevers should be much softer than the bonds between bulk atoms in the tip and sample. The typical values for  $k$  in the contact mode are  $0.01^{-5}$  N/m. Even though it has been demonstrated that atomic resolution is possible with the contact mode AFM[10], the method can be applied in certain cases for e.g. working at low temperatures where the coefficients of thermal expansions are very small etc. Even with these restrictions, static AFM does not produce atomic resolution on reactive surfaces like  $Si$ , since chemical bonding of the AFM tip and the sample poses a problem.

### 1.1.2 Dynamic AFM

In the dynamic operation modes, the cantilever is deliberately vibrated. There are two basic methods of dynamic operation, i.e amplitude modulation (AM) and the frequency modulation (FM). In AM-AFM [11], the actuator is driven by a fixed amplitude  $A_{drive}$  at a fixed frequency  $f_{drive}$ , where  $f_{drive}$  is close to the resonance frequency of the free

cantilever  $f_0$ . When tip approaches the sample, elastic and inelastic interactions cause a change in both the amplitude and the phase of the cantilever. These changes are used as the feedback signal. While the AM mode was initially used in a noncontact mode, it was later implemented very successfully at a closer distance range in ambient conditions involving tip-sample interactions (tapping mode)[12]. The AM mode is slow with high-  $Q$  cantilevers. However, the use of high  $Q$ -factors reduces noise. Albrecht *et al.* found a way to combine the benefits of high  $Q$  and high speed by introducing the frequency modulation (FM mode) [13]. Using the FM mode, the resolution was improved drastically[14, 15] and finally atomic resolution [16] was obtained by reducing the tip-sample distance and working in vacuum. Therefore it is the preferred technique for atomic studies in vacuum. Although, it was believed that initially that the net force between the front atom of the tip and the sample has to be attractive when the atomic resolution is desired, this view has been completely changed recently[17]. The dynamic mode is useful for the measurement of soft samples and loosely bound structures on the surface e.g. nanoparticles on a surface because as opposed to contact mode the dynamic mode can be used to image the surface without causing deformations or wear to the tip or the sample during imaging.

### 1.1.3 Tapping mode force microscopy

The amplitude of the cantilever oscillations serves as a control parameter in atomic force microscopy. A detailed description and analysis of this technique is given by Garcia and Perez [18]. This technique was first presented by Zhong et al. [19]. A tip oscillation of 20 to 100 nm is excited close to the cantilever resonance frequency, and the root mean square value of the deflection detector is used as control parameter for the tip-sample distance. The amplitude is reduced due to an intermittent contact during each cycle and this scheme was therefore named tapping mode force microscopy. The advantage of this mode is that lateral forces are greatly reduced compared to the contact mode, while the resolution is limited only by the tip shape. Large oscillation amplitudes are required for the tapping mode in air, in order to overcome the capillary forces by the restoring force of the cantilever spring.

### 1.1.4 Phase imaging

In this technique, the oscillation amplitude is detected with a lock-in amplifier. Therefore, additional information can be obtained from the phase shift between excitation and oscillation of the cantilever. Phase imaging can resolve material inhomogeneities at surfaces in great detail. Maganov et al. have reported a superior contrast in phase images as compared to topographic images. However, the enhanced contrast of phase images may arise from the dependence of adhesion on the surface curvature[20]. Determination of the

phase shift can help to identify the respective interaction regime. Conditions that produce a phase shift above  $90^\circ$  are characteristic of an attractive regime, while phase shifts below  $90^\circ$  indicate a repulsive regime[21]. These findings can help in avoiding bistability conditions. The best contrast in phase images is found for situations where attractive and repulsive interactions contribute similarly to the total interaction. Even slight changes in adhesion or stiffness will greatly affect the oscillation parameters. This is the regime of bistabilities which result in sudden changes in the phase contrast which are difficult to quantify.

### 1.1.5 Kelvin probe force microscopy

Kelvin probe force microscopy (KPFM), also known as surface potential microscopy, is a noncontact variant of atomic force microscopy (AFM) that was invented in 1991[25]. With KPFM, the work function of surfaces can be observed at atomic or molecular scales. The work function relates to many surface phenomena, including catalytic activity, reconstruction of surfaces, doping and band-bending of semiconductors, charge trapping in dielectrics and corrosion. The map of the work function produced by KPFM gives information about the composition and electronic state of the local structures on the surface of a solid.

In KPFM, the potential offset between a probe tip and a surface can be measured using the same principle as a macroscopic Kelvin probe. The cantilever in the AFM is a reference electrode that forms a capacitor with the surface, over which it is scanned laterally at a constant separation. The cantilever is not piezoelectrically driven at its mechanical resonance frequency  $\omega_0$  as in normal AFM although an alternating current (AC) voltage is applied at this frequency.

When there is a direct-current (DC) potential difference between the tip and the surface, the AC+DC voltage offset will cause the cantilever to vibrate. The origin of the force can be understood by considering that the energy of the capacitor formed by the cantilever and the surface is

$$E = \frac{1}{2}C[V_{DC} + V_{AC}\sin(\omega_0 t)]^2 = \frac{1}{2}C[2V_{DC}V_{AC}\sin(\omega_0 t) - \frac{1}{2}V_{AC}^2\cos(2\omega_0 t)]$$

plus terms at DC. Only the cross-term proportional to the  $V_{DC} \cdot V_{AC}$  product is at the resonance frequency  $\omega_0$ . The resulting vibration of the cantilever is detected using usual scanned-probe microscopy methods (typically involving a diode laser and a four-quadrant detector). A null circuit is used to drive the DC potential of the tip to a value which minimizes the vibration. A map of this nulling DC potential versus the lateral position coordinate therefore produces an image of the work function of the surface. In KPFM, the determination of the work function is based on the measurement of the electrostatic forces between the small AFM tip and the sample. The conducting tip and the sample are characterized by (in general) different work functions. When both elements are brought in contact, a net electric current will flow between them until the Fermi levels are aligned.



The potential is called the contact potential (difference) denoted generally with  $V_{CPD}$ . An electrostatic force between tip and sample builds up, resulting from the net charge transfer. For the measurement a voltage is applied between tip and sample, consisting of a DC-bias  $V_{DC}$  and an AC-voltage  $V_{AC} = \sin(\omega_2 t)$  of frequency  $\omega_0$  at the second resonance frequency of the AFM cantilever

$$V = (V_{DC} - V_{CPD}) + V_{AC} \cdot \sin(\omega_2 t)$$

Tuning the AC-frequency to the second resonance frequency of the cantilever results in an improved sensitivity and allows the independent and simultaneous imaging of topography and the contact potential. As a result of these biasing conditions, an oscillating electrostatic force appears, inducing an additional oscillation of the cantilever with the characteristic frequency  $\omega_2$ . The general expression of such electrostatic force not considering coulomb forces due to charges can be written as

$$F = -\frac{1}{2} \frac{dC}{dz} V^2$$

The electrostatic force can be split up into three contributions, as the total electrostatic force  $F$  acting on the tip has spectral components at the frequencies  $\omega_2$  and  $2\omega_2$ .

$$F = F_{DC} + F_{\omega_2} + F_{2\omega_2}$$

The DC component,  $F_{DC}$ , contributes to the topographical signal, the term  $F_{\omega_2}$  at the characteristic frequency  $\omega_2$  is used to measure the contact potential and the contribution  $F_{2\omega_2}$  can be used for capacitance microscopy.

$$\begin{aligned} F_{DC} &= -\frac{dC}{dz} \left[ \frac{1}{2} (V_{DC} - V_{CPD})^2 + \frac{1}{4} V_{AC}^2 \right] \\ F_{\omega_2} &= -\frac{dC}{dz} [V_{DC} - V_{CPD}] V_{AC} \sin(\omega_2 t) \\ F_{2\omega_2} &= +\frac{1}{4} \frac{dC}{dz} V_{AC}^2 \cos(2\omega_2 t) \end{aligned}$$

For contact potential measurements a lock-in amplifier is used to detect the cantilever oscillation at  $\omega_2$ . During the scan  $V_{DC}$  will be adjusted so that the electrostatic forces between the tip and the sample become zero and thus the response at the oscillation frequency  $\omega$  becomes zero and at the same time response at frequency  $\omega_2$  become maximum. Since the electrostatic force at  $\omega_2$  depends on  $V_{DC} - V_{CPD}$ ,  $V_{DC}$  corresponds to the contact potential. Absolute values of the sample work function can be obtained if the tip is first calibrated against a reference sample of known work function. Apart from this, one can use the normal topographic scan methods at the resonance frequency  $\omega$  independently of the above. Thus, in one scan, the topography and the contact potential of the sample are determined simultaneously.

## 1.2 Relevant forces

In this section, a short review of the relevant forces acting between the tip and the sample is given. The interaction range of the different types of force is of great importance for force microscopy, since different parts of the tip contribute differently to the total force which is measured.

### 1.2.1 Van der Waals Forces

Van der Waals forces are dipole-dipole forces. The most important forces are not those between permanent dipoles but dispersion forces. They act between dipoles that arise between fluctuations and dipoles induced in their electric field. They are always present and attract even chemically inert noble atoms. The van der Waals forces decay at short distances as  $F$  proportional  $1/r^7$  whereas beyond  $r \sim 5\text{nm}$  this power law reduces to  $F$  proportional  $1/r^8$ . The range of the van der Waals forces is limited, the tip-sample geometry of the force microscope can be approximated as a sphere approaching a semi-infinite body. For this configuration, the van der Waals force is given by

$$F_{vdW} = HR/6D^2$$

where  $H$  denotes the material dependent factor called Hamaker constant,  $R$  is the radius of the tip and  $D$  is the distance between the tip and the sample surface. For a tip of radius  $R = 30\text{nm}$ , the van der Waals force in vacuum at a distance  $D = 0.5\text{nm}$  is of the order of  $F_{vdW} = 2\text{nN}$ .

### 1.2.2 Electrostatic Forces

Electrostatic forces act between localized charges on insulating tips and samples. Their strength and distance dependence obey Coulomb's law. Charges can be easily trapped at the sample surfaces during surface preparation. Contact electrification can charge tip and sample after their contact is broken. Even in air, such charge can persist for hours and in vacuum for days. Charges on the surface also attract conductive tips. Electrostatic forces also act between conductive tips and conductive samples when they are at a different potential. The tip-sample system can be considered as a capacitor with distance dependence capacitance  $C$ , the force is given by

$$F_{ex} = \frac{1}{2} \frac{\partial C}{\partial z} (V_{bias} - V_{cpd})^2,$$

where  $V_{bias}$  is the voltage applied between tip and sample and  $V_{cpd}$  is the contact potential difference caused by the difference in the work functions of tip and sample. A minimum

electrostatic force at the nonzero bias voltage has also been found for insulating surfaces. For such materials, the electrostatic force follows changes in the bias voltage with a delay proportional to the resistivity of the sample [4]. The term  $\frac{\partial C}{\partial z}$  depends on the tip geometry which can be modelled as a half sphere on a truncated cone as suggested [5]. For small distances the dominating term is

$$F_{el} = \pi\epsilon_0 \frac{R}{Z} (V_{bias} - V_{cpd})^2.$$

Assuming a tip radius of  $R = 30\text{nm}$ , a tip-sample distance of  $z = 5\text{\AA}$  and a potential difference of  $V_{bias} - V_{cpd} = 1\text{V}$ , the electrostatic force is about  $F_{es} = 0.5\text{nN}$ . It is worth to notice that electrostatic forces not only contain a long range term. In ionic crystals where the neighbouring atoms have alternating charge signs, the electrostatic field has a short range exponential dependency [6].

### 1.2.3 Capillary Forces

In air, water vapor plays a dominant role. If the radius of curvature of the microcontact is below a critical radius, a meniscus will be formed. This critical radius is defined approximately by the size of Kelvin radius  $r_K = \frac{1}{(1/r_1 + 1/r_2)}$ , where  $r_1$  and  $r_2$  are the radii of curvature of the meniscus. The Kelvin radius is connected with the partial pressure  $p$  by the equation

$$r_K = \rho V / RT \log(p/p_s), \quad (1.1)$$

where  $\rho$  is the surface tension,  $R$  the gas constant,  $T$  the temperature,  $V$  the molar volume and  $p_s$  is the saturation pressure [7]. The surface tension of water is  $0.074\text{N/m}$  at  $T = 20^\circ\text{C}$ , which gives the parameter  $\rho V / RT = 0.54\text{nm}$ . Therefore,  $p/p_s = 0.9$ , Kelvin radius of  $100\text{nm}$  is obtained. For smaller vapor pressures the Kelvin radius becomes comparable to the dimensions of the molecules and the Kelvin equation is no longer applicable. In AFM, typical tips with radii less than  $100\text{nm}$  are possible nuclei for condensation. If a meniscus is formed, an additional capillary force acts on the tip. A simple estimate is given by

$$F = \frac{4\pi R\gamma \cos\theta}{1 + D[R(1 - \cos\phi)]},$$

where  $R$  is the radius of curvature,  $\theta$  the contact angle,  $D$  the distance between tip and sample and  $\phi$  the angle of the meniscus. For a tip radius of  $100\text{nm}$ , we obtain a force  $F_{max} = 9.3 \times 10^{-8}\text{N}$  which is stronger than the corresponding van der Waals force. Typical force vs distance curves in ambient conditions reveal adhesion forces of the order of  $10^{-8}$  to  $10^{-7}\text{N}$ , which mainly originate from capillary forces. Capillary forces can determine the size of the contact and play an essential role in the force microscopy measurements in air. Depending on the humidity, the presence of a meniscus has to be taken into account. The finite time of capillary formation can influence AFM results in the form of a modified velocity dependence[8].

### 1.2.4 Short-range forces

Short range chemical forces arise from the overlap of electron wave functions and from the repulsion of ion cores with ranges comparable to the extension of electron wave functions. These forces can be both attractive and repulsive. Model potentials like Lennard-Jones or the Morse-potential can be used to describe the short range forces. The Lennard-Jones potential is an empirical model consisting of two terms which combine the attractive Van der Waals and repulsive atomic potential

$$V_{Lennard-Jones} = -E_{bond} \left( \frac{2\sigma^6}{Z^6} - \frac{\sigma^{12}}{Z^{12}} \right),$$

where  $E_{bond}$  describes the binding energy and  $\sigma$  the equilibrium separation. However, their applications is limited to the pairwise interaction of atoms. For the tip-sample interaction, at least the interaction with the nearest neighbor atoms has to be included and the displacement of atoms by the action of the short range force has to be taken into account. Due to the variation of short-range forces on the atomic scale, atomic resolution becomes possible in atomic force microscopy.

## 1.3 How to measure energy dissipation in DFM

Most of the forces acting between tip and surface are conservative forces. However, when part of the work done by these forces is converted into heat, the damping of the cantilever oscillation can be exploited to measure dissipation.

In dynamic mode AFM, the oscillation parameters like amplitude, frequency and phase must contain information about the dissipation per energy cycle. For the dissipation it is useful to treat the system from the energy conservation point of view. Assuming a dynamic system is in equilibrium the average energy input must be equal to the average energy output or dissipation. Applying this rule to an AFM running in dynamic mode means that the average power fed into the cantilever oscillation by an external driver, denoted  $\overline{P_{in}}$ , must equal the average power dissipated by the motion of the cantilever beam  $\overline{P_0}$  and by the tip-sample interaction  $\overline{P_{tip}}$ ,  $\overline{P_{in}} = \overline{P_0} + \overline{P_{tip}}$ . The term  $\overline{P_{tip}}$  gives a direct physical quantity to characterize the tip-sample interaction. First, the input power  $\overline{P_{in}}$  is calculated for a cantilever with spring constant  $k$  whose base position  $z_d(t)$  is driven sinusoidally with amplitude  $A_d$  and a frequency  $\omega$ . Assuming a sinusoidal steady response, the deflection from equilibrium of the end of the cantilever,  $z(t)$  can be written as  $A \cos(\omega t + \phi)$  where  $A$  is the amplitude of the cantilever and  $\omega$  is the phase of the cantilever relative to the driver. The instantaneous power delivered by the driver is the force on the driver times the velocity of the driver:  $P_{in} = F \dot{z}_d = k[z(t) - z_d(t)] \dot{z}_d$ . Integrating over a complete cycle, the average power yields

$$\overline{P_{in}} = \frac{1}{2} k A_d A_\omega \sin \phi \quad (1.2)$$

This contains the familiar result that the maximum power is delivered to an oscillator when the response is  $90^\circ$  out of phase with the drive. Now, the power leaving the cantilever is addressed. Assuming that the background dissipation  $\overline{P}_0$  is well modeled by viscous damping of the cantilever body,  $F_{damping} = b\dot{z}$ , a similar analysis yields the average background power

$$\overline{P}_{in} = \frac{1}{2}bA^2\omega^2. \quad (1.3)$$

The power dissipated by the tip could now be solved, since experimentally, it was easiest to measure  $b$  by measuring the cantilever spring constant  $k$ , and then measuring the quality factor  $Q_{cant}$  and natural resonant frequency  $\omega_0$  from the shape and frequency of the free-cantilever resonance,  $Q_{cant} = k/(b\omega_0)$  was used to get

$$\overline{P}_{in} = \frac{1}{2} \frac{kA^2\omega}{Q_{cant}} \left[ \frac{Q_{cant}A_d \sin \phi}{A} - \frac{\omega}{\omega_0} \right] \quad (1.4)$$

It has to be noted that the reason that  $Q_{cant}$  and  $\omega_0$  appear in Eq. 1.4 is to express the viscous damping coefficient  $b$  in terms of experimentally accessible quantities. Eq. 1.4 does not imply that the resonant frequency or  $Q$  of the interacting cantilever remains the same, it only assumes that the viscous damping coefficient describing the damping of the body of the lever remains unchanged. It must be noted that so far no assumptions have been made regarding how the AFM is operated, except that the motion of the oscillating cantilever has to remain sinusoidal to a good approximation. Therefore eq 1.4 is applicable to a variety of different AFM modes. For example, in FM- mode AFM the oscillation frequency  $\omega$  changes due to the tip-sample interaction, while at the same time the oscillation amplitude  $A$  is kept constant by adjusting the drive amplitude  $A_d$ . By measuring these quantities, one can apply eq. 1.4 to determine average power dissipation related to tip-sample interaction.

Now, for AM-AFM mode or tapping mode, the cantilever is driven at a fixed frequency and with a constant drive amplitude, while the oscillation amplitude and phase shift may change when the probing tip interacts with the sample surface. Assuming that, the oscillation amplitude is chosen to be  $\omega_0$  eq. 1.4 can be simplified for the free oscillation amplitude  $A_0$

$$\overline{P}_{tip} = \frac{1}{2} \frac{kA^2\omega}{Q_{cant}} \left[ \frac{A_0}{A} \sin \phi - 1 \right] \quad (1.5)$$

One of the most important consequences of Eq. 1.5 is that, if the tip loses no energy, then the amplitude and the phase are not independent. Experimentally, phase imaging is performed with the amplitude held constant by a feedback loop, so it is only when the tip-sample interaction losses vary that phase contrast will be observed. Some recent modeling by Tamayo and Garcia [22] agrees with this. The one exception in which phase contrast is not due to dissipation arises because it is the  $\sin \phi$  rather than  $\phi$  itself that appears in Eq. 1.5. Since sine is a symmetric function about  $90^\circ$ , phase changes symmetric about  $90^\circ$  are allowed even if there are no losses in the tip-sample interaction. Such symmetric jumps from attractive ( $> 90^\circ$ ) to repulsive phases ( $< 90^\circ$ ) are observed in the modeling data

when conservative tip-sample interactions are used[22]. In standard phase imaging, the phase angle is plotted, so phase contrast observed where the phase jumps from attractive phases to repulsive phases is not due to dissipation, but is instead due to competition between the attractive and repulsive forces. Eq. 1.5 tells how we can interpret phase images taken on resonance at constant amplitude. The  $\sin \phi$  is simply proportional to the power being lost by the tip plus a constant. As long as the phase stays on one side of  $90^\circ$  the microscope is always operating in the attractive or the repulsive regime, then any changes in the phase image are directly due to changes in the energy being dissipated in the tip-sample junction. In fact, if a few parameters are measured, a phase image can be directly converted into a quantitative image of dissipation.

This method has been used in chapter 4 to calculate the amplitude threshold necessary to induce particle motion of different coated Au nanoparticles during surface scanning.

## 1.4 AFM as a Nanomanipulator

**Overview of manipulation of nanostructures by SPM** The introduction of SPM opened the path to the manipulation of nanoparticles, i.e. objects with the typical size of  $10^{-9} - 10^{-7}$  m. Numerous methods exist for the manipulation of nanostructures by scanning probe microscopy (SPM). This is extremely important for applications in control engineering and robotics etc. A brief summary of a few important results of the past decade where controlled positioning of single metal and semiconducting particles have been achieved is presented below. One of the first works on the manipulation was done by the Eigler group where a scanning-tunneling-microscope (STM)-based (as opposed to an atomic-force-microscope (AFM)-based) instrument was used[39], to arrange single atoms on surfaces into patterns. This extremely impressive work allowed them to observe the quantum nature of electrons, i.e., interference patterns of quantum waves [40] and other phenomena [41]. An STM-based instrument was also used to push or move individual molecules by Lyo [42], Jung et al. [43], Maruno et al. [44], and Beton et al. [45]. Single C<sub>60</sub> molecules were manipulated along the steps of a Cu(111) surface using a STM in ultrahigh vacuum (UHV) [47]. Unfortunately, despite the accurate level of control obtained with STM, the energy dissipated in the manipulation process cannot be estimated with this technique. Other groups began using AFM-based instruments since they could be used on nonconductive samples, operated in liquid and the forces required to manipulate molecules could be easily measured. Following is the list of the working principles of these manipulation techniques.

### 1.4.1 Feedback - off contact mode

A modified AFM to push nanometer-sized particles over surfaces was used by Junno et al. [47], Schaefer et al. [48], and Requicha et al. [49]. In these experiments, the sample

was imaged in noncontact mode to minimize the lateral force acting on the sample and it was manipulated in contact or non-contact mode [50] with the microscope feedback switched off. The problem with this process was that the normal force could not be controlled during manipulation, as the feedback was switched off. This would result either in damaged tips due to too much normal force or insufficient force to keep the tip on the surface.

### 1.4.2 Feedback - on contact mode

Hansen et al. [51] applied a scheme in which they imaged nanoparticles in tapping mode and pushed the particles over a surface in contact mode. Unlike the above mentioned methods, during pushing in contact mode, the feedback loop in the microscope was active. During image acquisition and tip positioning, the proportional, integral and differential gains of the feedback loop were set to the values normally used for image acquisition. During the pushing step, in contact mode, the proportional and differential gains were set to zero while the integral gain was set to about 1/20 th of the value used for image recording. This allowed the tip to follow the tilt and the topography of the sample applying a moderate vertical force but keeps the feedback response sufficiently low so a horizontal force high enough to cause movement was applied to the particle. A few groups developed instruments which had force feedback mechanisms, which allowed the user to feel the molecules under investigation in addition to visualizing it. Sitti and Hashimoto [52] described an instrument, which had three-dimensional (3-D) virtual reality visual feedback and a one-degree-of-freedom (1 DOF) haptic device for nano-scale haptic sensing. The system can also be used to manipulate molecules; however, the normal force feedback is switched off during manipulations. Using this setup, they have imaged and manipulated InAs quantum dots. Later Falvo et al. showed that the normal force could be controlled during manipulations, i.e., the microscope feedback was always on. Manipulation of large C60 islands on NaCl was performed by Lüthi et al. using contact atomic force microscopy (AFM) [54]. Even if the shear between the islands and crystal surface can be derived from the frictional forces experienced by the AFM tip while scanning, the applicability of contact AFM to nanomanipulation is limited to relatively large objects (tens of nanometers in size). Ritter et al. [63] as well as Dietzel et al. [23, 24] have also manipulated antimony nanoparticles grown on HOPG, in contact mode using two strategies: a push one and an tip-on-top manipulation applied for respectively large and intermediate-sized particles. Particularly the second mode was developed to move nanoparticles over large distances.

### 1.4.3 Manipulation by using electrostatic force

Here, the principle was to catch a nanocrystal with the AFM tip and deposit it elsewhere; the tip is used as an electrostatic nano-crane[55]. To catch a nanocrystal, the 2D dis-

placement of the tip was stopped above it, brought into contact with the nanocrystal. Negative and positive voltages (typically -3 and +3 V) were then successively and repeatedly applied between the tip and the sample. Once caught, the nanocrystal remained strongly pinned to the tip since it was possible to image the sample without depositing it. This is due to adhesion force. To deposit the nanocrystal, the tip was again brought into contact with the substrate. Negative and positive voltages (typically -3 and +3 V) were furthermore alternatively and repeatedly applied between the tip and the sample.

#### 1.4.4 Manipulation using Tapping mode AFM

A compromise between the manipulation by STM and contact AFM is tapping mode AFM. One way of manipulation by NC-AFM is the set-point reduction method [55]. Here, the NC-AFM tip approaches the nanoparticle with the amplitude  $A_{set}$ . When the tip is in close proximity to the nanoparticle, the computer is programmed to reduce  $A_{set}$  to another value say  $A_1$ . This value is chosen such that it is sufficient to induce tip-nanoparticle contact.  $A_1$  is at least a few nm below the value of  $A_{set}$  at the transition point between positive and negative contrast for the nanoparticle. The tip is moved laterally with  $A_{set}$  equal to  $A_1$  for a predetermined time/distance as shown in and the nanoparticle is pushed to a new location. Once this is accomplished, the computer resets the amplitude to  $A_{set}$ , such that the tip returns to the imaging mode.

## 1.5 Discussions

In this chapter, the different operation modes of the AFM were discussed. The techniques described will be applied for the characterization of nanoparticles. The application of AFM not only as an imaging tool but also as a tool to measure the adhesion forces and contact potential is demonstrated. Different techniques of nanoparticle manipulation by AFM were described. The technique which was used in this thesis was the manipulation in tapping mode as it provides accurate manipulation and also indirect access to dissipation. Manipulation of spherical and asymmetric nanoparticles will be discussed in the coming chapters.





## Chapter 2

# Preparation and Characterization of nanoparticles

Nanoparticles are becoming increasingly important in many areas, including catalysis, biomedical applications, and information storage. Their unique physical and chemical properties which are significantly different from the corresponding bulk or microcrystalline materials make these materials superior. Nanoparticles are often produced and stored in the colloidal form, and hence a dispersed deposition is necessary to study the individual properties of surface-bound nanostructures.

In this chapter, we focus on the preparation techniques of nanospheres and nanorods. The goal was to achieve a homogenous distribution of nanospheres/rods on different substrates and then determine the shape, size and/or size distribution of nanoparticles by using the AFM in dynamic mode. Different dilutions of nanospheres/rods were applied on various substrates e.g. clean silicon, mica and chemically treated silicon and imaged at ambient conditions. Influence of the nature of the substrate/ particles on the deposition rate was studied. Relative adhesive forces between nanoparticle agglomerates and hard surfaces were measured with the help of the force distance spectroscopy. AFM tips were also prepared, such that a small nanoparticle aggregate was glued to the tip, which then contributed mainly to the force interaction. With the parallel development of a phase locked loop electronics, which permits the simultaneous operation of several modes for distance and contact potential regulation, the Kelvin force microscopy could be applied to nanoparticle samples. On conducting substrates the local contact potential of silicon or gold particles could be mapped at the same time with their topography. Further planned measurements are to supply absolute values of electrical conductivity of the materials.

## 2.1 Synthesis of nanoparticles

Synthesis methods for nanoparticles are typically grouped into two categories : top-down and bottom-up approach. The first involves division of a massive solid into smaller portions. This approach may involve milling or attrition, chemical methods, and volatilization of a solid followed by condensation of the volatilized components. The second, bottom-up method of nanoparticle fabrication involves condensation of atoms or molecular entities in a gas phase or in solution. The latter approach is far more popular in the synthesis of nanoparticles. The most common particle synthesis techniques are solid-state processes, vapor phase and solution precipitation. There are a handful of processes that combine aspects of one or more of these broad categories of processes. Although vapor-phase processes have been in vogue in the early days of nanoparticles development, the other two processes mentioned above are widely used in the industry for production of micron sized particles, predominantly due to cost considerations. A description of nanoparticles synthesis techniques follows.

### 2.1.1 Top-Down Approach

#### Solid-state synthesis of nanoparticles

This technique generally involves a heat treatment step (in order to achieve the desired crystal structure), which is followed by media milling. High energy ball milling is one of the methods that fall under this category. A ball mill, a type of grinder, is a cylindrical device used in grinding (or mixing) materials like ores, chemicals, ceramic raw materials and paints. Ball mills rotate around a horizontal axis, partially filled with the material to be ground plus the grinding medium. Different materials are used as media, including ceramic balls, pebbles and stainless steel balls. An internal cascading effect reduces the material to a fine powder. Industrial ball mills can operate continuously, fed at one end and discharged at the other end. Large to medium-sized ball mills are mechanically rotated on their axis, but small ones normally consist of a cylindrical capped container that sits on two drive shafts (pulleys and belts are used to transmit rotary motion). High-quality ball mills are potentially inexpensive and can grind mixture particles to as small as 5nm, enormously increasing surface area and reaction rates. The grinding works on principle of critical speed. The critical speed can be understood as that speed after which the steel balls (which are responsible for the grinding of particles) start rotating along the direction of the cylindrical device; thus causing no further grinding.

However, there are some disadvantages of this techniques, due to issues pertaining to impurity pick up, lack of control on the particle size distribution, and inability to tailor precisely the shape and the size of particles, as well as the surface characteristics to name a few.

### 2.1.2 Bottom-Up Approach

- **Vapor-Phase synthesis of nanoparticles :** Nanoparticles can be synthesized by vapor phase reactions. Reactions and synthesis are carried out at elevated temperatures and under vacuum. Vacuum is needed to ensure a low concentration of growth species so as to promote diffusion-controlled subsequent growth. Grown nanoparticles are normally collected on a non-sticking substrate placed down stream at a relatively low temperature. Obviously, only a small fraction of nanoparticles settle on the substrate surface and moreover these particles may not represent the true particle size - distribution. It is also difficult to introduce stabilization mechanism during synthesis to prevent the formation of agglomerates.
- **Spray Pyrolysis :** Spray pyrolysis combines aspects of gas-phase processing and solution precipitation, it has been widely used in the preparation of metal and metal oxide powders. The process can be simply described as converting micro-sized liquid droplets of precursor or precursor mixture into solid particles through heating. In practice, spray pyrolysis involves several steps:
  - (i) generating micro-sized droplets of liquid precursor or precursor solution,
  - (ii) evaporation of solvent,
  - (iii) condensation of solute,
  - (iv) decomposition and reaction of solute,
  - (v) sintering of solute particles.

Nanoparticles synthesized by this route are found to exhibit smooth surface and spherical shape.

- **Synthesis inside micelles or using microemulsions :** The synthesis of nanoparticles can be achieved by confining the reaction in a restricted place. This method is exemplified by the synthesis of nanoparticles inside micelles or in microemulsion. In micelle synthesis, reactions proceed among the reactants that are available only inside the micelle and the particle stops growing when the reactants are consumed. When surfactants or block polymers, typically consisting of two parts : one hydrophilic and the other hydrophobic, are dissolved into a solvent, they preferentially self-assemble at air/aqueous solution or hydrocarbon/solution interfaces. The hydrophilic part is turned towards the aqueous solution. When the concentration of the surfactants exceeds a critical level, they self-assemble in such a way to form micelles. Surfactants or block polymers will reside at the interface separating hydrocarbon and aqueous solution. A microemulsion is a dispersion of fine liquid droplets of an organic solution in an aqueous solution. Such a microemulsion system can be used for the synthesis of nanoparticles. The chemical reactions can take place either at the interface between the organic droplets and the aqueous solution, when the reactants are introduced separately into two non-mixable solutions, or inside

the organic droplets when all the reactants are dissolved into organic droplets.

- **Chemical synthesis :** In this thesis, all the particles used were prepared by this technique. Reduction of metal complexes in dilute solutions is the general method in the synthesis of metal colloidal dispersions, and a variety of methods have been developed to initiate and control the reduction reactions. The formation of monosized nanoparticles is achieved in most cases by a combination of a low concentration of solute and polymeric monolayer adhered onto the growth surfaces. Both a low concentration and a polymeric monolayer would hinder the diffusion of growth species from the surrounding solution to the growth surfaces, so that the diffusion process is likely to be the rate limiting step of subsequent growth of initial nuclei, resulting in the formation of uniformly sized nanoparticles. In the synthesis of colloidal nanoparticle dispersion, various types of precursors, reduction reagents, other chemicals are used to promote or control the reduction reactions, the initial nucleation and the subsequent growth of the initial nuclei. Described below is an example of chemical synthesis of gold nanospheres and nanorods.
  - **Gold Nanosphere Synthesis by Citrate Reduction :** The method reported by Turkevich et al.[26] in 1951 is widely used to prepare aqueous solutions of gold nanospheres. Hydrogen tetrachloroaurate ( $HAuCl_4$ ) solution is brought to boil, and at that point sodium citrate ( $Na_3C_6H_5O_7$ ) solution is added. Citrate ions reduce  $Au^{3+}$  ions, producing gold atoms and other oxidation products (e.g. acetone dicarboxylate) [27]. Upon reaching the supersaturation limit, the gold atoms precipitate out as gold nanospheres. Chloride ( $Cl^-$ ) ions and the remaining citrate ions adsorb on the gold nanoparticle surface, making the nanospheres negatively charged. Average gold nanoparticle size can be controlled from 5 nm to 100 nm by varying the sodium citrate - gold ratio [28].

**Stabilization** Gold nanoparticle colloid prepared by the Turkevich method (ref. fig. 2.1) is generally stable. An electrical double layer forms around a nanoparticle due to the adsorbed chloride and citrate ions, and the Coulombic repulsion between the electrical double layers is strong enough to prevent agglomeration [27]. For a long-term stability, we can further cap the nanospheres with ligand molecules (e.g. 3-mercaptopropionate ions). Stable nanoparticle colloids can be stored up to a few months. While the chemical route allows a facile and cost-effective synthesis of monodisperse nanospheres, the physicist, who is interested in the properties of individual particles, faces the practical problem of particle deposition. The liquid-suspended particles must be transferred onto a suitable support without aggregation. The preparation method required for such a transfer is discussed in the following section.

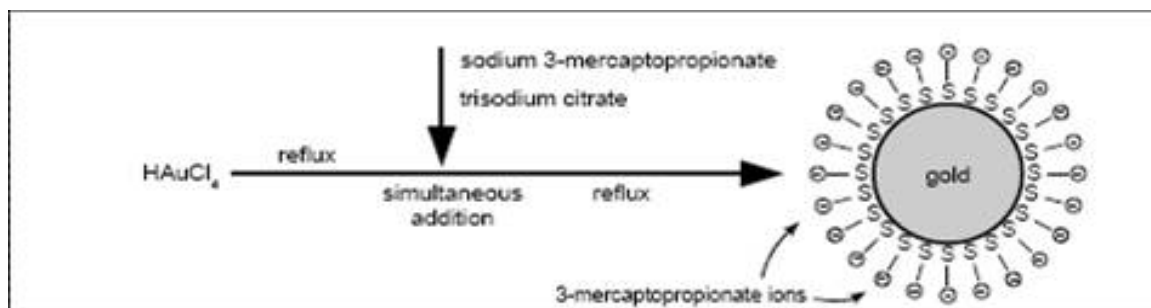


**Figure 2.1:** One-step synthesis of ligand-stabilized gold nanoparticles

- **Gold nanorod synthesis** A variety of methods have been used to prepare gold nanorods. For example: the template directed method by Martin and others [29] the electro chemical method introduced by Wang [30] the photochemical reduction method reported by Yang [31], and seed mediated growth method shown by Murphy which is discussed below [32, 33]. Metal salts are reduced in water, at room temperature, with a strong reducing agent (sodium borohydride) to yield 3.5 – 4 nm spherical seed particles. These faceted nanospheres can be capped with a variety of surface groups that could be present during the reaction. Ascorbic acid is used as a weak reducing agent. Ascorbic acid by itself and at room temperature is not capable to fully reduce the metal salt all the way to the elemental metal; but upon addition of the seeds, the reaction is thought to take place on the seed surface and be autocatalytic, to produce larger nanorods. The presence of the structure-directing agent is crucial for obtaining nanorods. Cetyltrimethylammonium bromide (CTAB) is uniquely suited to produce rods. The concentration of CTAB is critical for nanorod growth. CTAB functions as a soft rodlike micellar template for gold nanorod growth. The surfactants make rodlike micelles in water. The formation of the surfactant bilayer on the gold nanorods as they grow is quite important. The dynamic formation of a bilayer of surfactant on gold surfaces via the hydrocarbon tails may indeed provide enough stabilization during gold nanorod growth, in a zipper fashion, to lead to the formation of longer nanorods (see fig. 2.2).

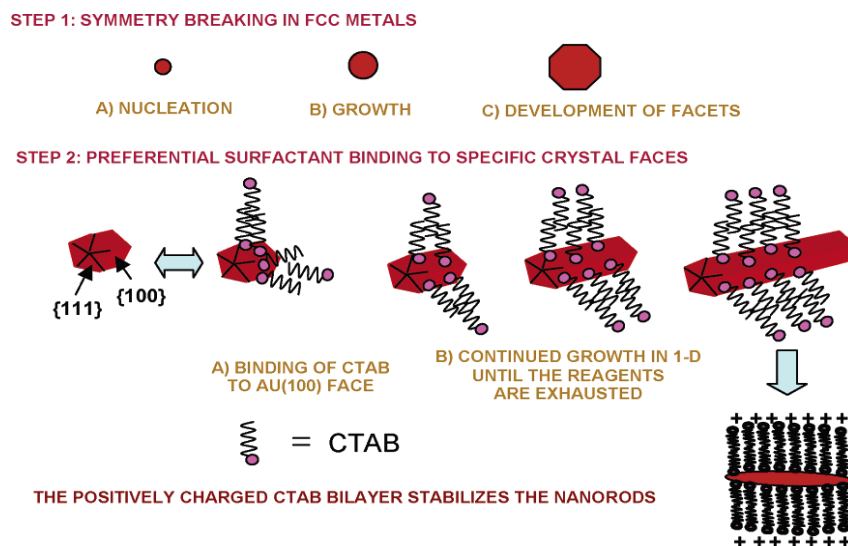


**Figure 2.2:** Mechanism of surfactant-directed Au nanorod growth

## 2.2 Conventional methods of deposition

### 2.2.1 Self assembly

Self-assembly is a widely used technique that relies on silanization or dendrimer modification of the sample surface. For particle deposition, the modified substrate is immersed in a colloidal solution for a few hours or days, after which the substrate is taken out and dried. The deposited particles are bound strongly to the modified surface and do not aggregate upon drying. Lithography is possible with various techniques that limit the surface modification to predefined areas. A very uniform deposition with practically no aggregation is possible with stable colloids, but the surface preparation requires a lot of practice, and the method needs to be tailored differently for different substrates and colloids.

### 2.2.2 Dip coating

Dip coating techniques can be described as a process where the substrate to be coated is immersed in a liquid and then withdrawn with a well-defined withdrawal speed under

controlled temperature and atmospheric conditions. The coating thickness is mainly defined by the withdrawal speed, by the solid content and the viscosity of the liquid. More recently, an angle-dependent dip coating process has been developed. Control of layer thickness is important for optical coatings. The coating thickness is dependent on the angle between the substrate and the liquid surface. Layer thickness can be calculated including the dipping angle and different layer thickness can be obtained on the top and bottom side of the substrate.

### 2.2.3 Spin Coating

Spin coating involves the acceleration of a liquid puddle on a rotating substrate. The coating material is deposited in the center of the substrate either manually or by a robotic arm. The physics behind spin coating involves a balance between centrifugal forces controlled by spin speed and viscous forces which are determined by solvent viscosity. The spin coating technique consists of three basic stages:

- (a) The solution is dispersed onto the wafer,
- (b) The solution is spread across the wafer (by spinning at approximately 500 rpm),
- (c) The wafer is then spun at a higher speed (2000 – 4000 rpm)

Some variable process parameters involved in spin coating are:

- Solution viscosity
- Solid content
- Angular speed
- Spin Time

The film-forming process is primarily driven by two independent parameters viscosity and spin speed. The range of film thicknesses easily achieved by spin coating is 1-200nm. For thicker films, high material viscosity, low spin speed, and a short spin time are needed. However, these parameters can affect the uniformity of the coat. Multiple coatings are preferred for a film thickness greater than 15nm .



### 2.2.4 Boil deposition

A rather interesting deposition technique was introduced by K. Lee et al.[34] The substrate is heated up to a temperature of  $150^{\circ} - 180^{\circ}$  C and then a drop of the solution was put onto it. The solution evaporates immediately resulting in a homogenous distribution of nanospheres/ rods. The boil deposition to gives better results with fewer aggregates, and the results are less sensitive to solvent viscosity.

### 2.2.5 Simple deposition

A simple deposition method was used for our measurements. A drop of the solution was left on the substrate for 10-30 minutes depending on the density of the nanoparticles required. It was then blown by a stream of nitrogen till dry. The sample can be used immediately after this procedure. In this process, bare substrates can be used, and basic cleaning procedures are often sufficient. The method can be applied to different substrates and colloids with little or no change in the details. While self-assembly typically takes a few hours to a few days. This deposition technique thus allows a faster preparation with significantly less effort. The boiling technique was introduced by Lee et al. at a later stage of this thesis, therefore, most of the experiments were done by using the simple deposition technique. Although, this is not the best technique for deposition, a homogeneous distribution of nanoparticles could be achieved.

## 2.3 Characterization of nanoparticles by AFM

Using the Atomic Force Microscope (AFM), individual particles and groups of particles can be resolved and unlike other microscopy techniques, the AFM offers visualization and analysis in three dimensions. Titanium oxide, zirconium oxide, alumina, silicon dioxide, gold nanospheres and gold nanorods and/or agglomerates were prepared on different surfaces and characterized them by AFM in the dynamic mode. Given below is a brief description of the particles, substrates and instruments used for measurements. It was mentioned in Chapter 1 that two different projects were undertaken during the course of this thesis. The particles used are classified by the project in which they were used.

- **Characterization of nanoparticles - *Nanosurf Project***

Both nanospheres in the form of solid powders as well as nanospheres suspended in a liquid medium were used for this project. Solid alumina ( $Al_2O_3$ ) nanopowder was provided by QinetiQ Nanomaterials (Great Britain). Aqueous suspensions of titanium oxide ( $TiO_2$ ) particles and zirconium oxide ( $ZrO_2$ ) particles were brought from Bühler GmbH (Germany). The surface of these particles was chemically modified

with a specific surface treatment (e.g. carboxylic acid) in order to prevent aggregation in the liquid. The average size of  $TiO_2$  and  $ZrO_2$  particles estimated by optical characterization techniques was  $8 \pm 3$  nm and  $11 \pm 3$  nm, respectively. Furthermore, we investigated plain ( $SiO_2$ ) or modified silicon oxide (Si-COOH) nanospheres (size 50nm) provided by G. Kisker GbR (Germany).

- **Manipulation of nanoparticles - *Nanoparma Project***

Gold nanoparticles (50 and 100nm diameter) provided by G. Kisker GbR (Germany), were used for the manipulation experiments. These particles are mainly spherical and were in the form of liquid suspensions wherein specific ingredients are added to guarantee the stability of the suspensions. Gold nanospheres (25 nm diameter) were also used which was provided by the group of Dr. Karine Mougine, CNRS, Mulhouse. Gold nanorods (axial diameter 10nm, length 29nm) in DI water with  $< 0.1\%$  ascorbic acid and  $< 0.1\%$  CTAB surfactant capping agent from Nanopartz™ were also used for the manipulation of asymmetric nanoparticles.

### 2.3.1 Substrates

For the experiments bare and modified silicon oxide surfaces, Mica and HOPG were used as substrates for the nanoparticles. Surface treatments included :

- (a) *Chemical treatment* : In case of modifying the clean Si surface of the substrate before depositing nanospheres, APTES (3-Amino Propyl Triethoxy Silane) (Fluka, Switzerland) was used for the silanization process. The goal of this treatment was to increase hydrophobicity of the substrate. The untreated Si substrates were cleaned with ethanol in an ultrasonic bath for 10 minutes, dried with nitrogen and then left in an ozone chamber for 5 minutes. The cleaned substrates were then exposed to an APTES atmosphere by suspending them in a glass desiccator which contained a small amount of APTES and toluene in a ratio of 1:10 for 1 hour [37, 38].
- (b) *Patterning of the substrates using FIB* : Patterns were prepared on the very smooth (RMS = 0.19 nm) surface of a Si(0 0 1) wafer by FIB milling, using a dual beam system FEI DB235M combining a Ga+ FIB and a thermal field emission scanning electron microscope (SEM) (see fig. 2.3), working at coincidence on the sample. In the FIB milling technique a 5-50 keV energy ion beam is focused on a spot of few nanometers. Energetic ion impact causes the ejection of the target atoms with a sputtering rate proportional to the current density of the beam. Focusing the beam enables surface milling with a spatial resolution down to 5 nm. The ion beam can be scanned across areas as wide as few hundreds of micrometers by an electromagnetic deflection system; therefore surface can be directly modified without the need of resists or masks [35, 36]. Square-patterned ( $10m \times 10m$ ) arrays of parallel grooves and pits of different width and periodicity were realized by FIB sculpting (1 pA

ion beam current, 6 nm nominal spot size) following the corresponding bitmap files instructions.

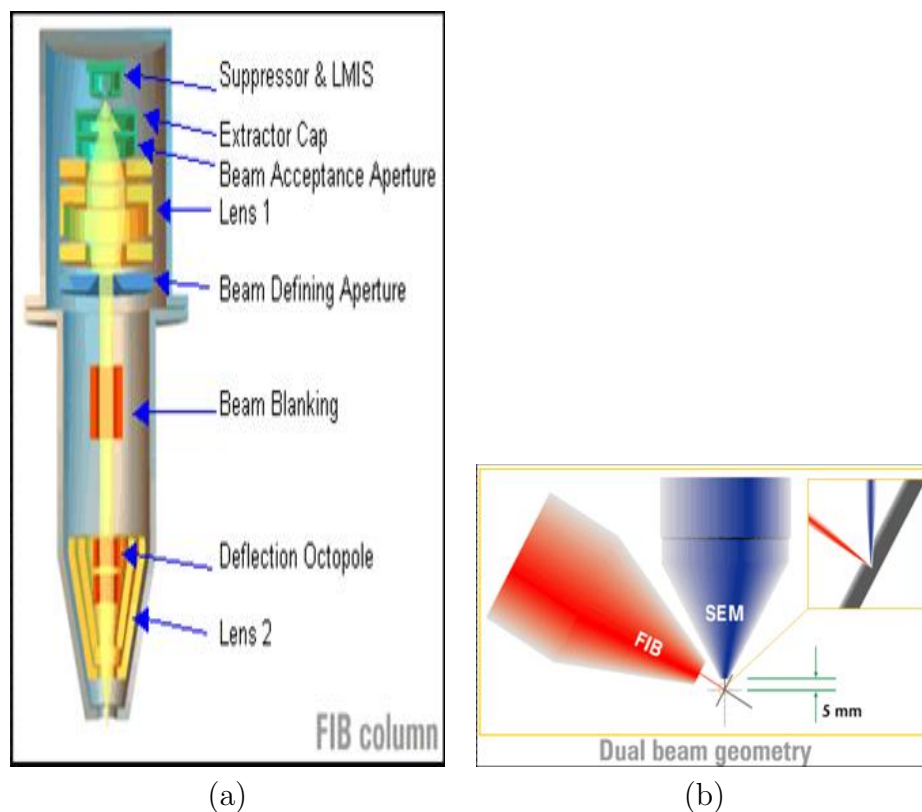


**Figure 2.3:** (a) FIB column, (b) dual beam geometry.

The surface morphology and overall shape of the features were studied by *in situ* high resolution SEM and by *ex situ* AFM, operating in tapping mode and equipped with a commercial silicon tip. Samples prepared by this method were used for manipulation experiments described in Chapter 3. The goal of using the patterned substrates was to study the "trapping" effects during manipulation. However, since the grooves were only 5nm deep, the particles easily crossed over instead of getting trapped by them.

### 2.3.2 Instruments

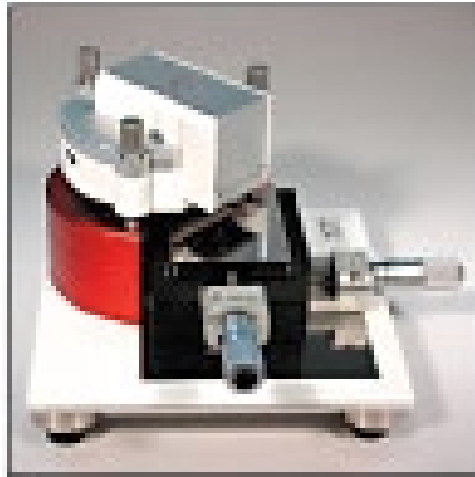


**Figure 2.4:** Nanosurf Mobile S



(a)



(b)

**Figure 2.5:** (a) Nanosurf Nanite, (b) the stage of the Nanite AFM was placed inside the temperature and humidity controllable box.

The AFM equipment used for this project was provided by Nanosurf AG (Switzerland). The maximum scan range of the Nanosurf<sup>TM</sup>Mobile S (fig. 2.4) is  $110\mu\text{m}$  in X and Y direction and  $22\mu\text{m}$  in height (Z-direction). The Nanosurf<sup>TM</sup>Mobile S system is expanded with a micrometer translation stage for precise positioning. However, in the course of the project, an automatic XYZ-stage was built by Nanosurf and composed with a mountable AFM of the latest high resolution technique, the so called Nanite. Nanosurf<sup>TM</sup>Nanite (fig. 2.5(a)) is equipped with a scanner of  $10\mu\text{m}$  maximum scan range and a maximum Z-scale of  $1.8\mu\text{m}$ . Dimension 3100 (Veeco, USA) was also used. Few measurements were performed on the UHV system (Omicron Nanotechnology, Germany) from the group of Dr André Schirmeisen.

### **Building of a temperature and humidity controllable box**

The measurement of very small structures by AFM in air implies a relatively constant environment in terms of temperature and humidity. The slightest air drift or temperature shift during the measurement can cause a drift in the image. Therefore, an isolating box was built around the microscope which maintains a constant humidity inside and keep the temperature fluctuations to a minimum. In addition, the box containing the microscope was put on top of an active damping table for vibration isolation (fig. 2.5(b)). Humidity was reduced by placing silica gel inside the box. Humidity and Temperature was monitored by a Lab-view programme. Imaging was done in the non-contact dynamic mode at ambient conditions with humidity of 30 – 40%. All images have been processed for better quality.

## **2.4 Experimental Results**

### **2.4.1 Preparation techniques for spherical nanoparticles**

**Preparation/Deposition techniques** For all the nanospheres the following method was used. The nanospheres were first diluted in deionized water to an appropriate concentration and then ultrasonicated. An appropriate amount of the dilution was put on a cleaned substrate (From a silicon (100) wafer small pieces of approx.  $0.25\text{cm}^2$  were cut, cleaned with a Q-tip and analytical pure ethanol, rinsed with ethanol and dried in a stream of pure nitrogen ; Mica and HOPG were freshly cleaved before use), incubated for 5 – 20 minutes depending on the density of particles required, and then the residual solution was blown by a stream of nitrogen. This general method was followed for all samples. This method will be referred to as **method 1** in the following chapter. Though this is a general method used for nanospheres, some alterations in the time of incubation, solution concentration etc had to be done. Described below is a detailed description of the preparation method for different nanospheres.

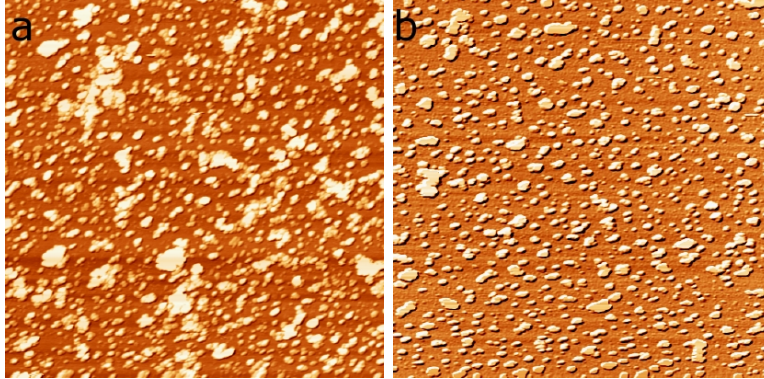


**Figure 2.6:** Phase images of  $ZrO_2$  nanospheres on (a) mica and (b) Si.

- (A) To get a sample of evenly distributed, relatively well separated particles on silicon (100), the stock solution of the particle suspension needs to be appropriately diluted. For  $TiO_2$  and  $ZrO_2$  suspensions, the stock solutions (20 % wt) were diluted 500 times in pure water to a particle concentration of 0.04g /100g suspension.  $20\mu l$  of this dilution was placed by a micro liter pipette on a clean silicon piece. After an incubation time of about 20 minutes - 1 hour, the remaining droplet was then dried by a stream of pure nitrogen. The sample could be used for measurement by the AFM right away.
- (B) For the  $Al_2O_3$  nanopowder, a stock solution of 0.02 wt % had to be preliminary prepared. The powder was weighed accurately into a glass beaker, which was then filled up with nanopure water until the desired dilution is reached. This suspension needs to be thoroughly mixed in an ultrasonic bath for 10 minutes before further dilution or use.  $20\mu l$  of the final dilution was placed by a microliter pipette on a clean silicon piece. After an incubation time of about 40 to 60 minutes, the sample was dried by a stream of pure nitrogen.  $Al_2O_3$  nanospheres were also prepared by vapour deposition and this process resulted in spherical particles in the form of agglomerates having a mean size of  $100 \pm 50nm$  and/or agglomerates having a size of  $5 - 200\mu m$ .
- (C) Suspensions of gold and silica particles were treated in the same way as titania and zirconia particles. The gold suspension (concentration unknown) was used without preliminary dilution while the silica suspension (25mg/ml) was 10 times diluted beforehand. Using this preparation method, the nanospheres were relatively well distributed over the substrate.

### 2.4.2 Imaging nanospheres on different substrates

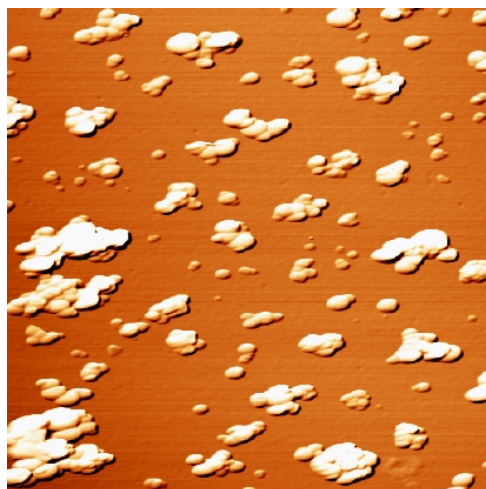


**Figure 2.7:**  $Al_2O_3$  (0.02%) nanospheres deposited on Silicon. Height of the nanospheres is about 50nm.

Fig. 2.6 shows  $ZrO_2$  nanospheres deposited on two different substrates. The nanospheres on mica (figure 2.6(a)) appear coagulated whereas those on Si (figure 2.6(b)) appear more separated. Mica which is very hydrophilic may have traces of the solution even after it was blow dried. This may cause the nanospheres to form agglomerates. Although the density of nanospheres was the same on both Si and mica.

- **Imaging of  $Al_2O_3$  nanospheres :** Fig. 2.7 shows an AFM image of  $Al_2O_3$  nanospheres on a clean Si substrate. It seems that the  $Al_2O_3$  nanospheres which are bare tend to agglomerate easily as compared to the  $TiO_2$  and  $ZrO_2$  nanospheres. This may be because the surfaces of the latter are chemically modified so that they remain well separated. Imaging of  $Al_2O_3$  nanospheres was relatively difficult because the tip easily picks up loosely bound  $Al_2O_3$  agglomerates.
- **Imaging nanospheres on chemically treated *Si* substrate :**

Nanoparticles were also imaged on chemically treated substrates. Clean Si was modified with APTES, a silanizing reagent, thereby increasing the hydrophobicity of the surface. The density of  $TiO_2$  nanospheres on clean Si surface (fig. 2.8(a)) is very high as compared to that of chemically treated Si (fig. 2.8(b)). Chemical treatment on a Si surface has increased the hydrophobicity of the surface thereby reducing adhesion of nanospheres. Despite the same concentration in the solution, fig. (a) shows 707 particles and fig. (b) shows only 11 particles. It was seen that chemical treatment (silanization) increases the hydrophobicity of the Si substrate. When an

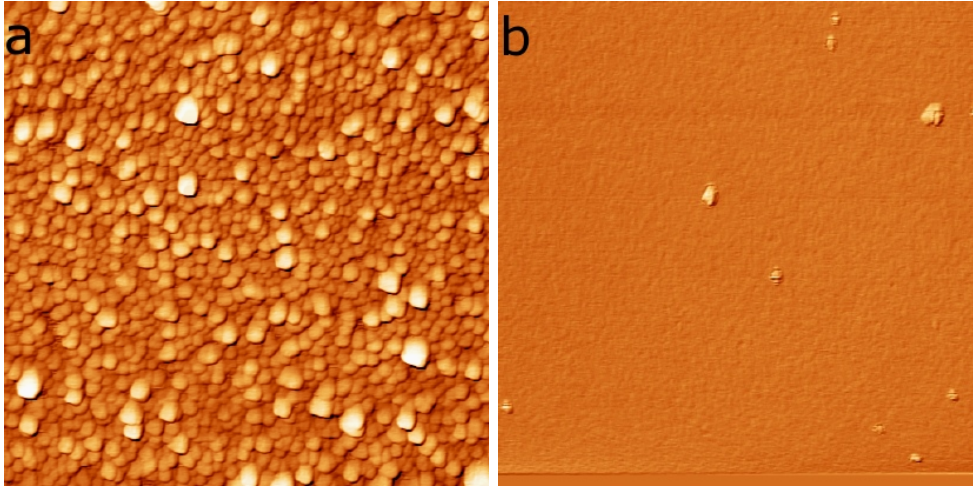


**Figure 2.8:**  $TiO_2$  nanospheres (from a suspension of 0.04%) on (a) Si (001) substrate and (b) chemically treated Si. Heights of the nanospheres are about 11 nm.

aqueous suspension of nanospheres is deposited on this substrate, the surface repels the suspension and hence the nanospheres do not adhere to the surface. This is why there is a reduced density of  $TiO_2$  nanospheres on a chemically treated Si substrate.

- **Imaging gold nanospheres :** No agglomeration of particles was observed for 50 and 100nm gold particles delivered by Kisker GbR. For example 50 nm gold particles deposited on a clean silicon substrate as described above, provided images of clearly separated single nanospheres of equal size and shape (Fig. 2.9).

**Sample preparation technique for nanorods :** Different preparation methods were tried for the deposition of nanorods, but the nanorods always seemed to be covered/surrounded by a thick surfactant layer, causing problems in the imaging and manipulation by AFM. To overcome this problem, the sample was first prepared by using the boiling technique [34] and then a drop of DI water was put on the surface and immediately blow dried by nitrogen. This procedure resulted in quite homogeneous (though some nanorods still existed in small bundles) and easily mobile sample of nanorods. This preparation method can be used for any kind of substrate. Fig. 2.10(a) shows the nanorods covered with a surfactant layer and fig. 2.10(b) shows that the washing has resulted in the absence of the surfactant layer. This preparation method would be referred as **method 2** in the following chapters.



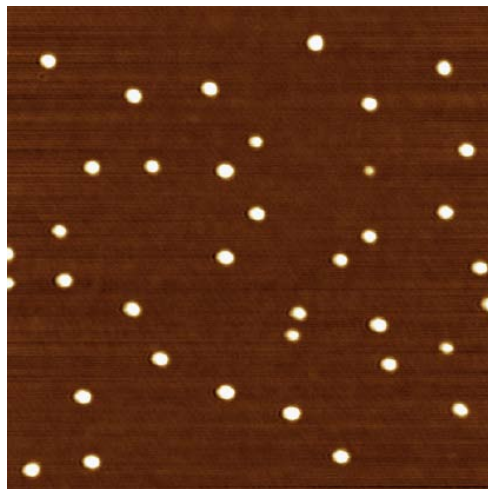


**Figure 2.9:** Topography image of 50nm gold particles.

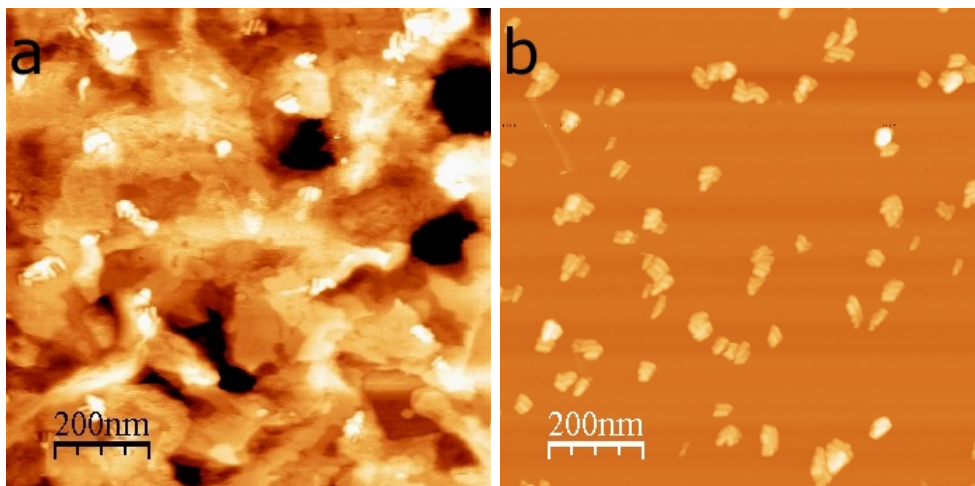


**Figure 2.10:** AFM images of nanorods, (a) Nanorods deposited on Si by boiling technique and (b) Nanorods deposited on Si by boiling technique and then washed with water.

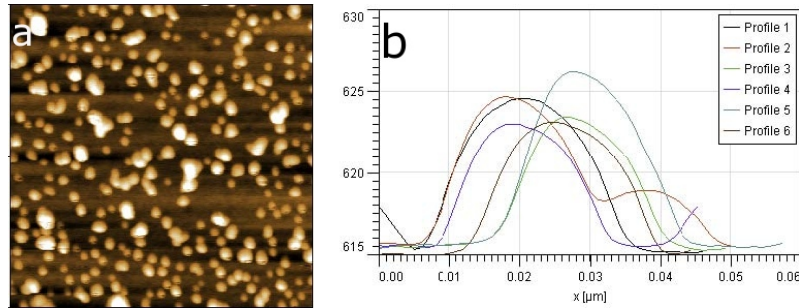


**Figure 2.11:** Topography image of  $TiO_2$  on silicon (left) and line profiles through different particles selected thereof (right).

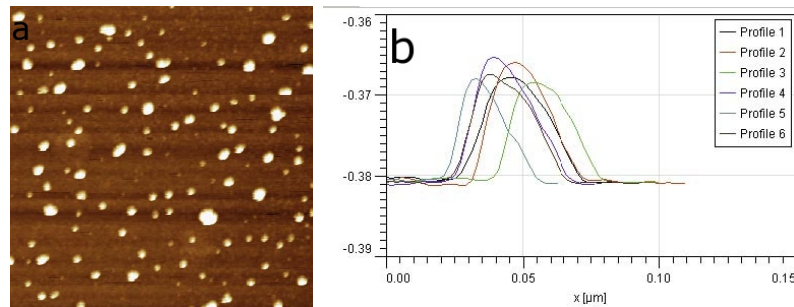


**Figure 2.12:** (a) Topography image (left) of  $ZrO_2$  on silicon ( $1 \times 1 \mu m$ ) and (b) line profiles through different particles selected thereof (right).

**Determination of geometrical characteristics of nanoparticles :** A sample of  $TiO_2$  nanospheres, prepared as described above (method 1), was imaged by AFM on a cleaned silicon substrate (fig. 2.11(a)). The particles are well separated and equally distributed over the surface. The lateral size of the nanospheres may vary because of the variation in the tip shape. However, in this image, the height of the most prominent features was found to be relatively constant between 8 and 11 nm (fig. 2.12(b)).

### 2.4.3 Accurate determination of particle size

A sample of  $ZrO_2$  nanospheres, prepared as described above (method 1), was imaged by AFM on a cleaned silicon substrate fig 2.12(a). The particles are again well separated and equally distributed over the surface. The lateral size of the  $ZrO_2$  nanospheres appears bigger than the size of the  $TiO_2$  nanospheres. However, the height of the most prominent features is comparable to that of the  $TiO_2$  particles and was found to be relatively constant between 11 and 14 nm fig 2.12(b).

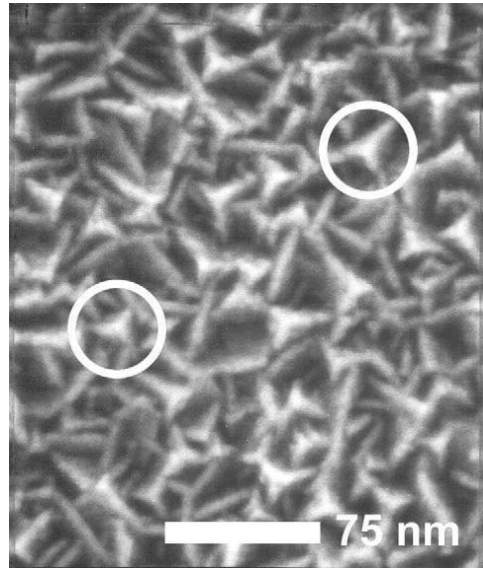


**Figure 2.13:** SEM image of NioProbe

From the previous AFM images of nanospheres on a plain and flat silicon surface, it can be seen that the lateral sizes of the particles not always correspond to the true size of the particles. An appropriate tip characterization measurement prior to the particle imaging should be performed in order to determine the influence of the actual tip size on the lateral particle size.

This was realized by reverse imaging of a special grating, the so called NioProbe (Electron Microscopy Sciences, USA) (fig. 2.13), which permits qualitative and quantitative information on the actual tip size. Reverse imaging of the probe is the most convenient means of obtaining the effective radius of the probe. For this purpose, the ideal characterization sample would consist of small, stiff, spiked features. The surface structure of the NioProbe film is densely populated by tiny peaks. Feature peaks exhibit imaging radii of less than 5 nm, as sharp as anything else available. This permits one to obtain the accurate apex radius. The new automatic XYZ-stage of the Nanite microscope is best suited to exchange automatically between two or more samples without changing the tip or opening the system. Once the scan is completed on the NioProbe, a quick estimate of the upper bound of the tip radius may be made by using a simple formula:

$$r_T = \frac{(w/2)^2 + h^2}{2h} \quad (2.1)$$

Several features of the NioProbe should be analyzed in the same manner to obtain an average value for  $r_T$ . In the image below (fig. 2.14), a scan of  $515 \times 515$  nm was performed

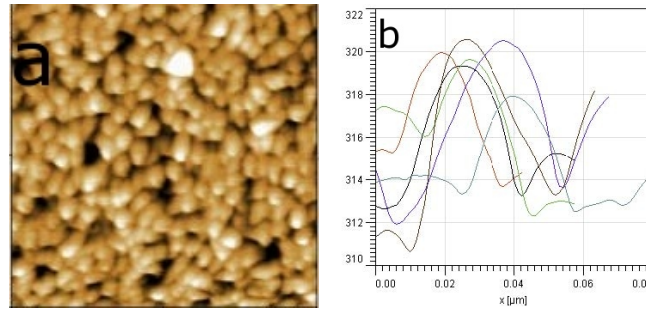
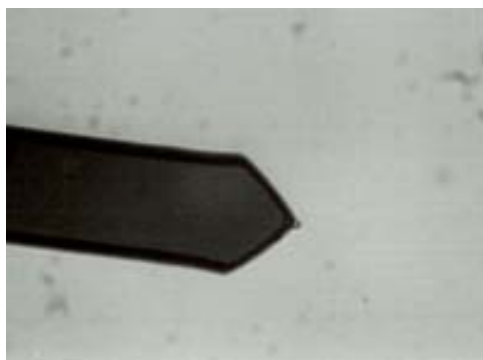


**Figure 2.14:** Topography image (left) of the NioProbe and line profiles through different particles selected thereof (right).

on the NioProbe with the same tip as the one used for the  $TiO_2$  image shown above (Figure 2.11). The approximate tip apex concluded from six prominent features on the NioProbe gives a value of 19.7 nm. This value is double than the guaranteed tip apex of a fresh and unused tip. This is quite surprising, since the tip was only used for 2 scans on  $TiO_2$  before the image on NioProbe was performed (only 20 minutes later!). In other words, the tip radius was altered by more than 10 nm in a very short time during the measurement. The tip could have either picked up something from the  $TiO_2$  nanospheres on the previous surface or it has become blunt by contact forces with the sample surface. Determining the true size of particles by measuring the NioProbe with the same tip beforehand or afterwards, is a very effective and fast procedure. However, we encountered discrepancy when the nanoparticle sample exhibits a different density than the NioProbe peaks. Particles or peaks obtained from line profiles through single features which are closely packed appear smaller than particles which are clearly separated. Therefore, we believe that the above formula cannot always be used to calculate both, an estimate of the tip apex and an estimate of the radii of the features, if the peak densities of the two samples are differing.

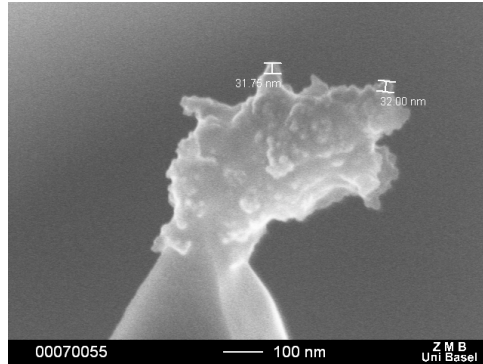
## 2.5 Determination of the adhesion of nanoparticles

In order to determine adhesive forces between nanoparticles and different surfaces, the particles had to be fixed on the sensor beforehand. As first trial, we used glass microbeads ( $1\mu\text{m}$  in diameter) which we glued manually at the far end of a tipless cantilever by using a micromanipulator (fig. 2.15). The micromanipulator was built in house by the group of Dr. Simon Rast and is well suited to fix microparticles onto cantilevers.



**Figure 2.15:** Microbead attached to a tipless cantilever (Leitz Aristomet, light microscope, 500 $\times$  magnifications)

However, since the nanoparticles are too small in order to be seen under the light microscope, we had to approach the tip against an agglomeration of particles. This was more easily achieved by using the AFM as manipulator. The resolution of the video camera integrated in the AFM scan head was almost as good as the highest resolution achieved under the light microscope and the movement of the approach motor was even more accurate and precise than the manual manipulator. Nevertheless, the success rate to fix an agglomerate of particles to the sensor tip, was only about 50%. It was found that the amount of glue and the size of the agglomerate picked up are crucial and have to be found experimentally. All experiments were done with aluminium oxide nanopowder and soft silicon oxide tips (PPP-CONT cantilevers from Nanosensors). A small amount of powder was spread out with a piece of thin paper on silicon or glass. The same was done with the glue (Araldite Rapide, two component epoxy glue). Once an agglomerate of nanoparticles was attached to the tip of the cantilever, the cantilever was placed in the oven at 100 $^{\circ}$ C for at least 4 hours for hardening of the epoxy glue. Then, the functionalized tip was ready to use (fig. 2.16).

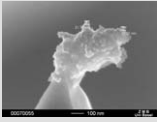
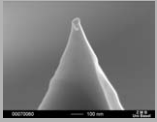
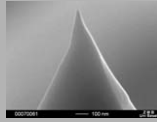
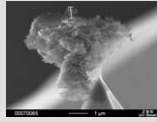
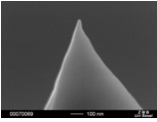
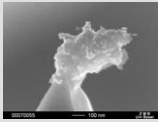
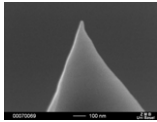
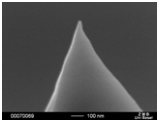


**Figure 2.16:** Alumina oxide agglomerate glued at the tip apex (SEM image)

The attractive forces between the nanoparticles and the surface were quantitatively determined by force-distance curves (see table in fig.2.17). It was found that the nanoparticles had higher adhesion force to the substrate as compared to that between the tip and the substrate. Also, adhesion forces between the tip and silicon surface was lower than the forces between the tip and either of Mica and HOPG surfaces. In some cases, it was difficult to judge whether there were nanoparticles on the tip or just plain glue as the adhesion forces between glue and the surface was similar to that between the nanoparticles and the substrate. The relative humidity inside the box was kept constant at 20 to 30% whilst measuring. The adhesion force was calculated by multiplying the length of the rupture in nanometers with the spring constant of the cantilever. In order to compare force values of different cantilever preparations, the adhesion force was always put in relation to the approximate contact radius of the tip which was determined from the SEM images.

## 2.6 Determination of the contact potential of nanoparticles

Since the new electronics to conduct non-contact AFM together with Kelvin Probe Force Microscopy was not yet ready to implement in the Nanite system, a commercial Lock-in and a Kelvin Controller was used, which was built earlier for our high vacuum AFM system. Silica and gold particles were deposited on Indium Tin Oxide surfaces (ITO). Indium Tin Oxide is electrical conductive and transparent when deposited as thin layers on glass, for instance. ITO is mainly used to make transparent conductive coatings for liquid crystal displays, flat panel displays, plasma displays, touch panels, solar cells etc. The cantilevers used have an overall metallic coating (PtIr5) on both sides of the cantilever increasing the electrical conductivity of the tip (PPP-EFM, Nanosensors). The force constant of this type is specially tailored for the electrostatic force microscopy yielding very high force sensitivity while simultaneously enabling tapping mode and lift mode operation. The nominal value given for the resonance frequency is 75 kHz. The frequency

Tip No.	No.3	No. 4	No. 5	No. 6	Plain tip
Functionalization	Aluminium oxide	Aluminium oxide or glue?	Glue	Aluminium oxide	Si
SEM image of tip					
Approx. contact radius of the tip (nm)	31	70	30	50	25
<b>Surface</b>	<b>Silicon (100)</b>	<b>Silicon (100)</b>	<b>Silicon (100)</b>	<b>Silicon (100)</b>	<b>Silicon (100)</b>
Measured rupture (nm)	115 +- 5	331 +- 54	354 +- 40	115 +- 68	37 +- 9
Spring constant	0.09764	0.09877	9.01234	8.342	0.06758
Calculated adhesion force (nN)	11.3	32.7	35.4	11.5	2.5
<b>Adhesion force per square size of the tip (nN/nm)</b>	<b>0.37</b>	<b>0.47</b>	<b>1.18</b>	<b>0.23</b>	<b>0.10</b>
Tip No.	No.3	Plain tip			Plain tip
Functionalization	Aluminium oxide	Si			Si
SEM image of tip					
Approx. contact radius of the tip (nm)	31	25			25
<b>Surface</b>	<b>Mica</b>	<b>Mica</b>			<b>HOPG</b>
Measured rupture (nm)	391 ± 37	68 +- 7			62 +- 3
Spring constant	0.09764	0.06758			0.06758
Calculated adhesion force (nN)	38.1	4.6			4.2
<b>Adhesion force per square size of the tip (nN/nm)</b>	<b>1.23</b>	<b>0.18</b>			<b>0.17</b>

**Figure 2.17:** functionalized tips used for force distance curves on different surfaces

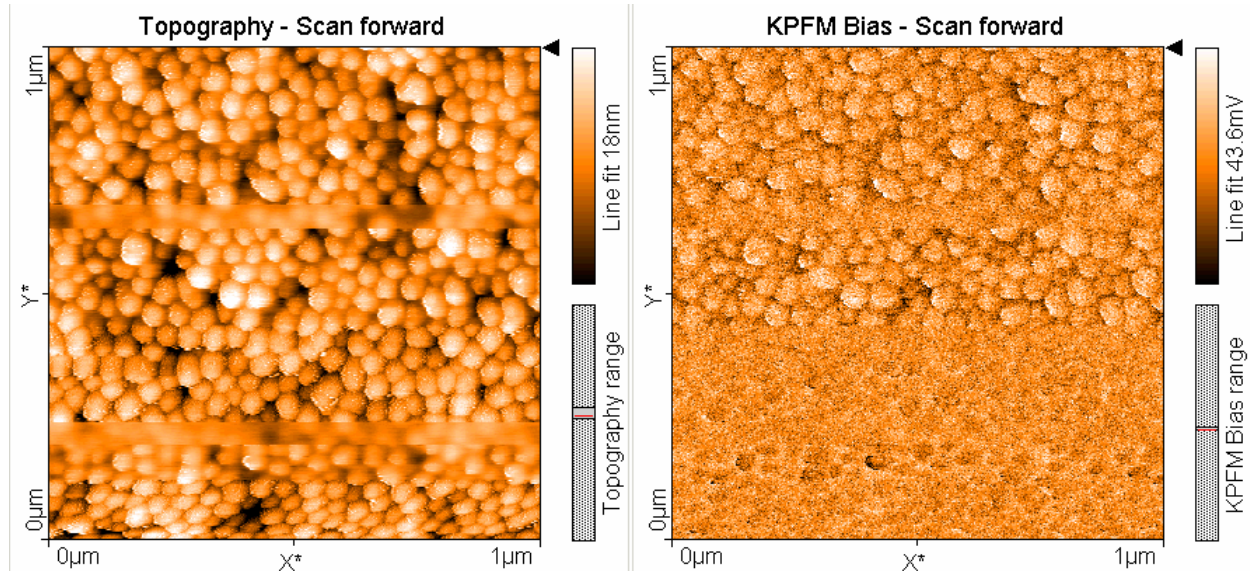


**Figure 2.18:** Topography (left) and KPFM (right) image of silica particles (50nm, Kisker) on ITO with changing tip voltages.

used for simultaneous KPFM measurement is 6.28 times higher than the first resonance and was found around 460 kHz. In fig. 2.18, the tip voltage was stepwise adjusted from +2V to -3V in order to follow the change in contrast. The best topography contrast was found at 0V to -2V while the best KPFM contrast was found at -2V. This shows clearly that the contact potential can be influenced independently from the topography and that the KPFM contrast is improved by adjusting the applied DC voltage to the tip.

## 2.6.1 Conclusions

Behavior of nanoparticles was studied by the use of different kinds of substrates, chemically altering the nature of the substrate by using nanoparticles with bare or chemically modified surfaces.  $TiO_2$ ,  $ZrO_2$  and  $Al_2O_3$  nanospheres were applied on different kinds of substrates, in different concentrations and were imaged by AFM in dynamic mode. The resultant images were found to be influenced by the kind of substrate used, the nature of the surface of the nanoparticle and also the dilution of the nanoparticle suspension. The nature of the substrate plays a very important role; it influences the density of the nanoparticles and the distribution of the particles that are deposited onto its surface. It was seen that  $ZrO_2$  nanospheres when deposited on mica appear to form agglomerates whereas on Si substrate they appear well distributed. This may be due to the hydrophilic nature of mica. It was also seen that chemical treatment (silanization) of Si increases the hydrophobicity of its surface. When an aqueous suspension of nanoparticles is deposited



on this substrate, the surface repels the suspension and hence the nanoparticles do not adhere to the surface. This is why there was a reduced density of  $TiO_2$  nanospheres on a chemically treated Si substrate as compared to that on clean Si. It seems that the adhesion of the nanoparticles to the substrate decreases with the increase in the hydrophobicity of the surface and vice versa. The nature of the nanoparticle surface also influences the distribution on the substrate.  $TiO_2$  and  $ZrO_2$  nanospheres have a chemically treated surface which prevents them from forming agglomerates. Whereas  $Al_2O_3$  nanospheres are bare and therefore have a tendency to adhere better to each other than to the substrate and tend to coagulate. On a silicon surface, the biggest adhesion forces measured were achieved when the tip was functionalized with glue only. Smaller adhesion forces were determined when the tip was functionalized with nanoparticles. A similar interaction force was measured with a plain, untreated silicon tip. The adhesion force of a tip functionalized with aluminium oxide on mica was bigger than the same measurement performed on silicon, which is explained by the strong capillary forces existing on a hydrophilic surface like mica. Therefore, it is very important that a constant environment is established and that especially ambient humidity is reduced. An alternative way to ensure that the measurement is not negatively influenced by a remaining water film on the surface is when a reference measurement is performed in liquid. These first measurements of the contact potential difference between different materials do not yet deliver absolute values but they are quite promising and with better resolution of the AFM scan head and the new and more sensitive electronic hardware, the contact potential can be accurately measured even under ambient conditions. Hence, some more measurements need to be planned for determining the adhesion forces and the contact potential of the nanoparticles.

## Chapter 3

# Analytic relations between particle and probe trajectories in atomic force microscope nanomanipulation

Nanomanipulation is a complex problem, where mechanical and chemical properties of substrates, probing tools, and nano-objects (particles) are combined and different results are expected depending on the geometry of the tip, sample and environmental conditions. Despite the fundamental and practical interest of this problem, systematic investigations on nanomanipulation are still scarce. A reason for that is the difficulties in quantifying the dynamical processes occurring while manipulation, that is, collisions between probing tips and particles, friction between particles and substrates, electrostatic interactions among all of them, and so forth.

In this chapter, a simple model is deduced to relate the trajectories of spherical nanoparticles pushed by an atomic force microscope tip to the scan pattern of the tip. Manipulation of gold nanoparticles on silicon surfaces in ambient conditions confirm the predictions of this model. In the second part of the chapter, the model is extended to address the relation between the frictional forces acting on spherical nanoparticles to the trajectories of the particles. This model is also used to interpret the trajectory fluctuations and the apparent discontinuities observed when spherical gold particles are manipulated on a silicon oxide surface by atomic force microscopy.

### 3.1 Manipulation of gold nanoparticles

In this thesis, the manipulation of nanoparticles was done using tapping mode AFM. The advantage of this technique is that one can measure the phase shift of the cantilever

oscillations with respect to the external periodic excitation and estimate the energy dissipation using the method described in Chapter 1. This method was recently used by Ritter and co-workers to manipulate antimony particles on a graphite surface in air [57]. During manipulation, the oscillation amplitude of the tip,  $A_{set}$ , was kept constant by a feedback loop. The area was repeatedly scanned by increasing excitation amplitude until a critical amplitude is reached by the oscillations of the probing tip. Beyond that threshold, the particles start to follow different directions. These trajectories depend on the geometry of the tip, particle and adhesion to the substrate. Controlling the trajectory of a nanoparticle sliding on a solid surface is extremely important in applications ranging from drug delivery to environmental control, hence analytical expressions relating the trajectories of spherical nanoparticles pushed by an atomic force microscope tip to the scan pattern of the tip are derived. Two different scan patterns were examined: (a) the raster scan path and (b) the zigzag scan path (fig. 3.1), since, in the Nanosurf AFM the tip follows the raster scan while in Veeco systems the tip follows the zig-zag path. Using the model which will be described in the following section we predicted that the angle of deflection  $\theta$  increases when the spacing decreases, approaching  $90^\circ$  in the limit case of infinitely close scan lines. The exact value of  $\theta$  depends on the size of tip and particle, but not on the position of the particle within the scan pattern.

### 3.1.1 The Model

#### Tip particle collision

In this sub-section the elastic collision between a spherical nanoparticle and an AFM tip operated in tapping mode is discussed. In the following equations,  $m$  and  $v$  are respectively the mass and the velocity of the particle,  $M$  and  $V$  are the effective mass and the average velocity of the cantilever, and the apex refers to quantities measured immediately after the tip particle collision. For the sake of simplicity, it is assumed that  $M = 10^{-10}$  kg,  $m = 10^{-18}$  kg, and  $V = 10^{-2}$  m/s. If the collision between tip and particle is supposed to be elastic, the total kinetic energy is conserved:

$$\frac{1}{2}MV^2 = \frac{1}{2}mv'^2 + \frac{1}{2}MV'^2 \quad (3.1)$$

Neglecting the interaction between particle and surface, the conservation of momentum along  $x$  and  $z$  direction implies

$$0 = mv'_x + MV'_x \quad (3.2)$$

$$MV = mv'_z + MV'_z \quad (3.3)$$

Here, it can be assumed that the  $x$  component of the cantilever velocity is negligible compared to its  $z$  component, so that  $V_z \approx V$ . According to the geometry in the figure,

the components of the particle velocity (after the collision) are related by

$$\frac{v'_z}{v'_x} = \tan \gamma \quad (3.4)$$

It is also assumed that the velocity gained by the particle in the  $z$  direction is much higher than that of the cantilever, i.e.  $V \ll v'_z$  (the validity of this hypothesis is confirmed by the results). From the previous equations, considering also that  $M \gg m$ , we easily get

$$v'_x = \frac{2 \tan \gamma}{1 + \tan^2 \gamma} V \quad (3.5)$$

for the velocity gained by the particle in the  $x$  direction. Assuming that  $V \sim 10^{-2}$  m/s we found that  $v \sim 10^{-3}$  m/s, independently of the particle and cantilever mass. This (apparently high) value has to be interpreted as follows. During the collision, the tip transmits a force  $F \sim mv/\tau$  impact to the particle, where  $\tau$  is the time duration of the collision. The value of  $\tau$  is in the order of the period of the cantilever oscillations, i.e.  $10^{-5}$  s. Thus,  $F_{\text{impact}} \sim 10^{-16}$  N, which is several orders of magnitude lower than the static friction to overcome in order to start the particle motion. Despite the limitations in the above discussion, it can be safely assumed that the particle displacement is purely a *geometric effect due to the shape of tip and particle and the direction of motion of the tip, and no dynamic effects are involved*. Based on this assumption a simple model is derived below.

### Estimation of the Particle trajectories

An AFM tip follows a certain scan path driven by piezoelectric or electromagnetic scanners connected to the surface or the tip itself. In standard setups, the tip moves forwards and backwards along the so-called *fast scan direction* ( $x$ ), then is translated along the *slow scan direction* ( $y$ ) over a certain distance  $b$ , scanned again forth and back along the  $x$  direction and so on (fig. 3.1(a)). It was assumed that the tip has a conical shape (with semi-aperture angle  $\gamma$ ), and is terminated by a spherical cap with radius  $R_t$ . Along the scan path, the tip encounters spherical particles of radius  $R_p$  (fig. 3.2(a)). The sections of tip and particle parallel to the  $x - y$  plane at their point of contact are circles with radii  $R_1$  and  $R_2$  respectively (fig. 3.2(b)). The centers of the two circles will be denoted  $O$  and  $P$ . In order to describe the collision between tip and particle, some assumptions are necessary.

- (1) First assumption is that the AFM is operated in tapping mode [58].
- (2) The oscillation amplitude of the tip is large enough to displace the particles [59]. In such cases, the tip hits the particle almost vertically, and momentum is transferred only along the line  $OP$  in fig. 3.2(b).

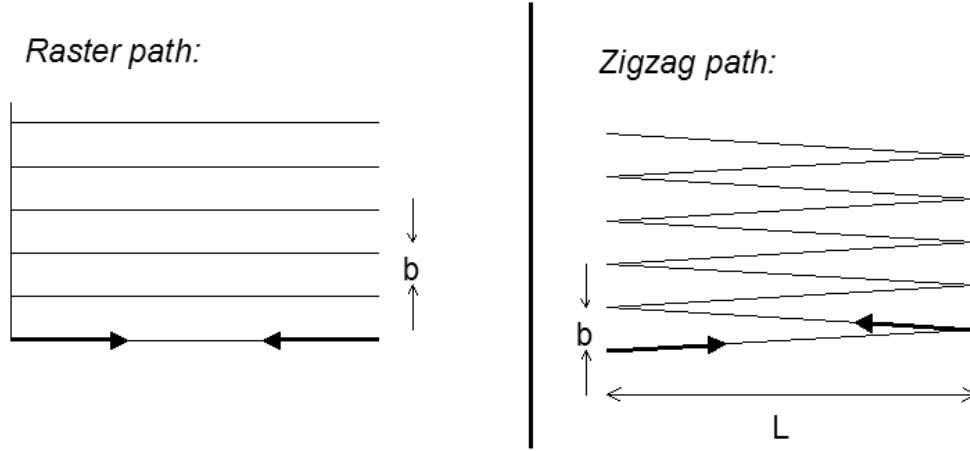


**Figure 3.1:** (a) Most typical scan patterns adopted in AFM: raster scan path (left) and (b) zigzag scan path (right).

- (3) It is also assumed that the adhesion between substrate and particles is strong enough to prevent any further displacement of the particle at the end of the tip-particle interaction.
- (4) The particle slides without rolling.

In tapping mode, with characteristic frequencies in the order of 100 kHz, the tip-particle interaction process consists of several collision events. At each collision, the displacement of the nanoparticle is determined by the relations

$$\frac{dy}{dx} = \tan \alpha, \quad \frac{dy}{d\alpha} = (R_1 + R_2) \cos \alpha$$

where  $\alpha$  is the angle between  $OP$  and the fast scan direction (fig. 3.2(b)). Dividing the equations by each other the displacement of the particle along the  $x$  direction is related to the variation of the angle  $\alpha$ . The total displacement  $\Delta x$  resulting from the tip-particle interaction process along a scan line is obtained by integrating between the initial and the final values of  $\alpha$ , which we will denote  $\alpha_0$  and  $\alpha_f$  respectively. The quantity  $\alpha_0$  depends on the initial position of the particle, and its value is not defined on the first scan line. In the further scan lines, it is easy to see that  $\alpha_0$  is always the same and is equal to (To derive this expression, note that the particle is shifted up of the quantity  $b$  between the upper sides of the 'corridors' described by the tip in two consecutive scan lines.)

$$\alpha_0 = \arcsin \left( 1 - \frac{b}{R} \right) \quad (3.6)$$

After interacting with the tip, the line  $OP$  forms an angle  $\alpha_f = \pi/2$  with respect to the  $x$  direction. The total displacement of the particle in the fast scan direction is thus given

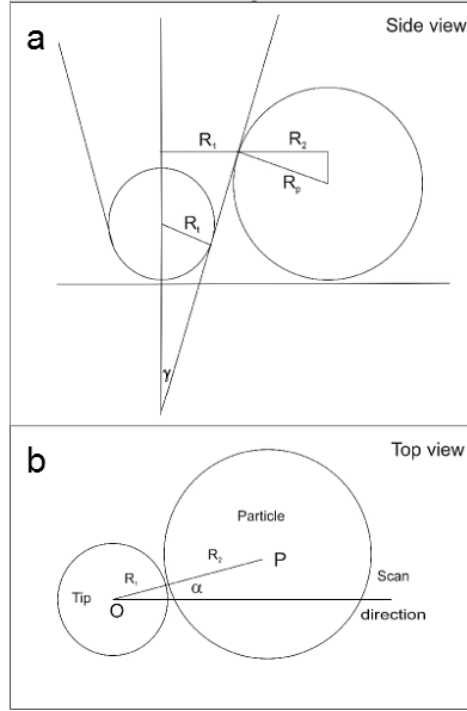


**Figure 3.2:** (a) Side view and (b) top view of a conical AFM tip colliding with a spherical particle.

by

$$\begin{aligned}\Delta x &= R \int_{\alpha_0}^{\pi/2} \frac{\cos^2 \alpha}{\sin \alpha} d\alpha \\ &= -R \left( \cos \alpha_0 + \log \tan \frac{\alpha_0}{2} \right)\end{aligned}\quad (3.7)$$

i.e. it is a function of the spacing  $b$  between two consecutive scan lines (for a given shape of tip and particle). With the exception of the first scan line, the corresponding displacement along the slow scan direction is  $\Delta y = b$ . Thus, the angle of deflection of the particle  $\theta$  (with respect to the  $x$  direction) is given by

$$\tan \theta \equiv \frac{\Delta y}{\Delta x} = -\frac{b}{R \left( \cos \alpha_0 + \log \tan \frac{\alpha_0}{2} \right)}\quad (3.8)$$

In order to conclude our derivation, we have to consider the 3D shape of tip and particle. With the geometry in fig. 3.2(a), two cases need to be distinguished. If  $R_p < R_t(1 - \sin \gamma)$ , the particle interacts with the spherical part of the tip and we get from geometric considerations:

$$R_1 = \frac{2\sqrt{R_t R_p}}{1 + R_p/R_t}, \quad R_2 = \frac{2\sqrt{R_t R_p}}{1 + R_t/R_p}\quad (3.9)$$

On the other side, if  $R_p > R_t(1 - \sin \gamma)$ , the particle interacts with the conical part of the tip, and

$$R_1 = R_t \cos \gamma + R_p \frac{1 + \sin \gamma}{1 - \sin \gamma} \frac{\sin 2\gamma}{2}, \quad R_2 = R_p \cos \gamma\quad (3.10)$$

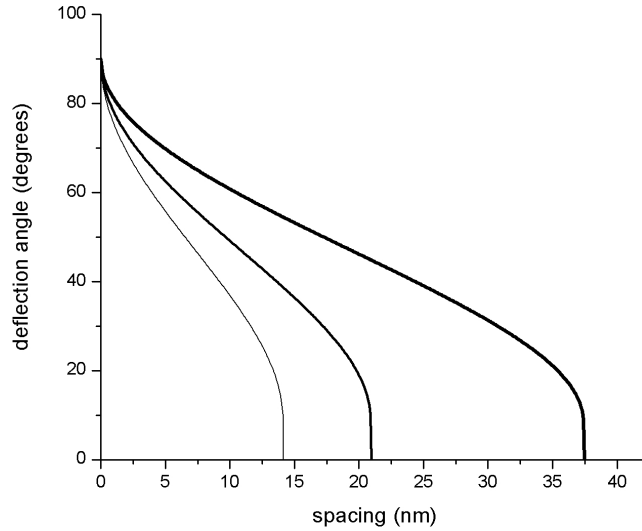


**Figure 3.3:** Theoretical angle of deflection of spherical particles with different radii (5, 10, and 25 nm, left to right curves) as a function of the spacing between consecutive scan lines in AFM manipulation. It was assumed that the tip has a radius of curvature of 10nm, and a semi-aperture of  $5^\circ$ .

By substituting the expressions (3.9) or (3.10) in the quantity  $R_1$  and  $R_2$  in (3.6) and (3.8), finally a relation between the deflection of the particle and the “spacing”  $b$  is obtained, which depends on the following parameters: the tip radius  $R_t$ , the particle radius  $R_p$ , and the semi-aperture angle  $\gamma$  of the tip. One can note that, if  $R_p < R_t(1 - \sin \gamma)$ , the quantity  $R$  is simply equal to two times the geometric average of the tip and particle radii,  $2\sqrt{R_t R_p}$ . In fig. 3.3, the angle of deflection expected for particles of different size (5, 10, 25 nm radii) is plotted as a function of the spacing  $b$ . As reference, a commercial tip with radius  $R_t = 10$  nm and semi-aperture  $\gamma = 5^\circ$  was considered. The angle of deflection approaches  $90^\circ$  for infinitely close scan lines ( $b \rightarrow 0$ ) and continuously decreases, becoming 0 when  $b = R$ , i.e. when a frontal collision between tip and particle occurs. By Taylor expansions of equations (3.6) and (3.8), the limit expression was derived:

$$\theta \simeq 90^\circ - \frac{2}{3}\sqrt{\frac{2b}{R}}, \quad (b \rightarrow 0). \quad (3.11)$$

It is also interesting that this model is analogous to the scattering theory. It can be assumed that a particle interacts with a center of scattering according to the classical scattering theory and by analytical or numerical integration a relation between the angle of scattering and the minimum distance (impact parameter) that the particle would maintain from the center of scattering, if its motion would not be perturbed, is established[57]. In the case of a raster scan path, the tip plays the role of the center of scattering (in a frame of reference solidal with the tip), whereas the role of the impact parameter is taken by the

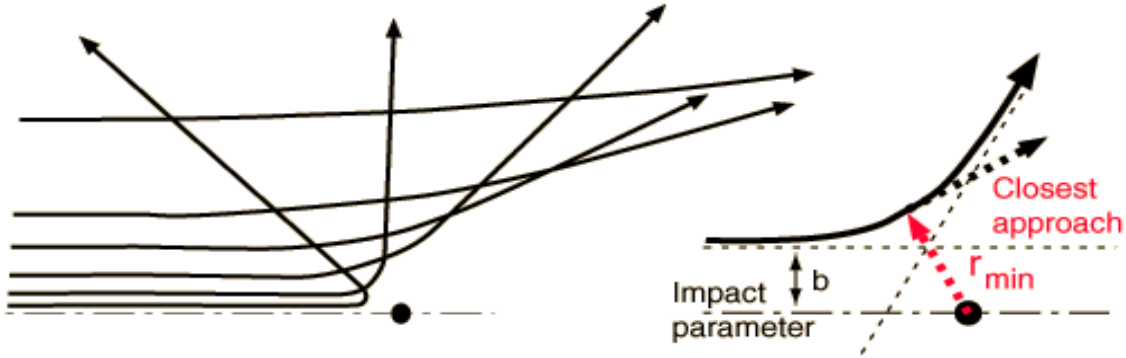


**Figure 3.4:** Rutherford scattering : Analogy of the impact parameter to the spacing in AFM manipulation.

spacing  $b$  (more precisely, by the distance  $R - b$  between the center of the particle and the scan direction). This is not the case for a zigzag scan path. In such a case the angle of deflection  $\theta$  increases with the position of the particle along the fast scan direction, and an almost symmetrical distribution of the particles with respect to  $\theta = 90^\circ$  is obtained.

### 3.1.2 Experimental Results

To check the applicability of the model, gold nanoparticles were manipulated on flat and patterned silicon surfaces under ambient conditions (RH 40%). Substrate and sample preparation method is similar to the procedure described in chapter 2. The surface morphology and overall shape of the features were studied by in situ high-resolution SEM, and by ex situ Atomic Force Microscopy (AFM). The surface pattern consisted of an array of nanopits (fig. 3.5(a)) and nanogrooves (fig. 3.5(b)) created by focused ion beam milling technique [Chapter 1]. The width and depth of the pits are 50 nm and 5 nm respectively, and the distance between adjacent pits is 125 nm. The grooves are 5nm deep and the distance between adjacent grooves is 125nm.

The silicon substrates were cleaned by cycles of acetone (10 min) and ethanol (2–10 min) in ultrasonic bath. After that a flux of nitrogen was used to dry the sample surface. The average diameter of the particles, as determined from SEM images, was  $25 \pm 5$ nm. The manipulation experiment was performed using a commercial AFM. Rectangular silicon cantilevers with resonance frequency of 190 kHz and spring constant of  $48Nm^{-1}$  have been used.



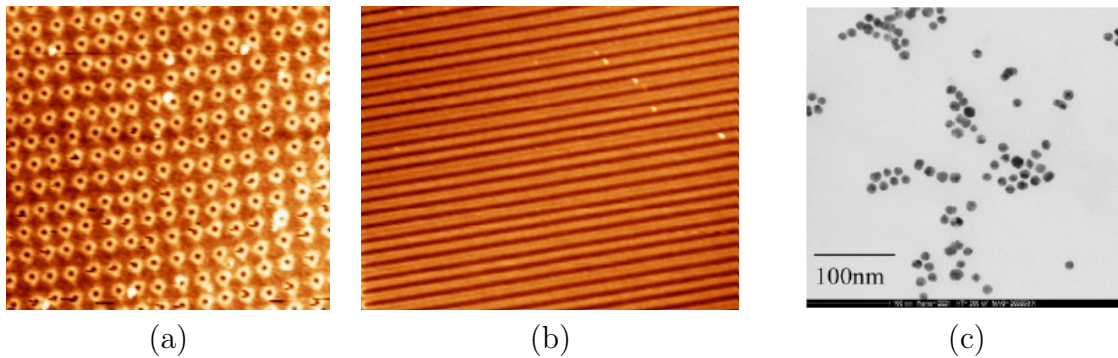


**Figure 3.5:** AFM images of patterned (a) Si-pits, (b) grooves, (c) SEM image of Au nanoparticles.

### Manipulation on flat or slightly nanostructured surfaces

On flat silicon surfaces, the direction of motion of the particles were initially well defined, but changed after acquiring a few images and also made it much more difficult to move the particles even at higher values of the drive amplitude, possibly due to tip contamination. Hence, it was not possible to do a large series of images with the same tip. Due to this reason patterned substrates were chosen. Fig. 3.6 shows the manipulation of gold nanoparticles on plain Si with different spacing (b), it can be seen that the tip has deteriorated from image (a) to (d).

On the patterned surface, the mean direction of motion remains defined even after long time of acquisition, which we attribute to "self-cleaning" of the tip crossing the shallow pits. Considering also that the pits had scarce influence on the particle direction (fig. 3.7(a)), and that this influence was anyway removed in the averaging process which determines the deflection angle, patterned surface was chosen, rather than the flat silicon surfaces, to test the applicability of equations (3.6) and (3.8). To estimate the angle of deflection  $\theta$  with the best accuracy, it was determined from 2D self-correlation of fig. 3.7(b), and of similar images taken for different values of the spacing  $b$ . Instead of the topography, the phase signal has been used, as a better contrast between particles and substrate was observed in such case [59]. Finally, the angle  $\theta$  was deduced by the orientation of the bright stripe passing through the center of the 2D correlation images.

Shown in fig 3.8 are a series of images taken by varying the spacing between scan lines to note the change in the angle of deflection. Images are taken with the same tip The spacing

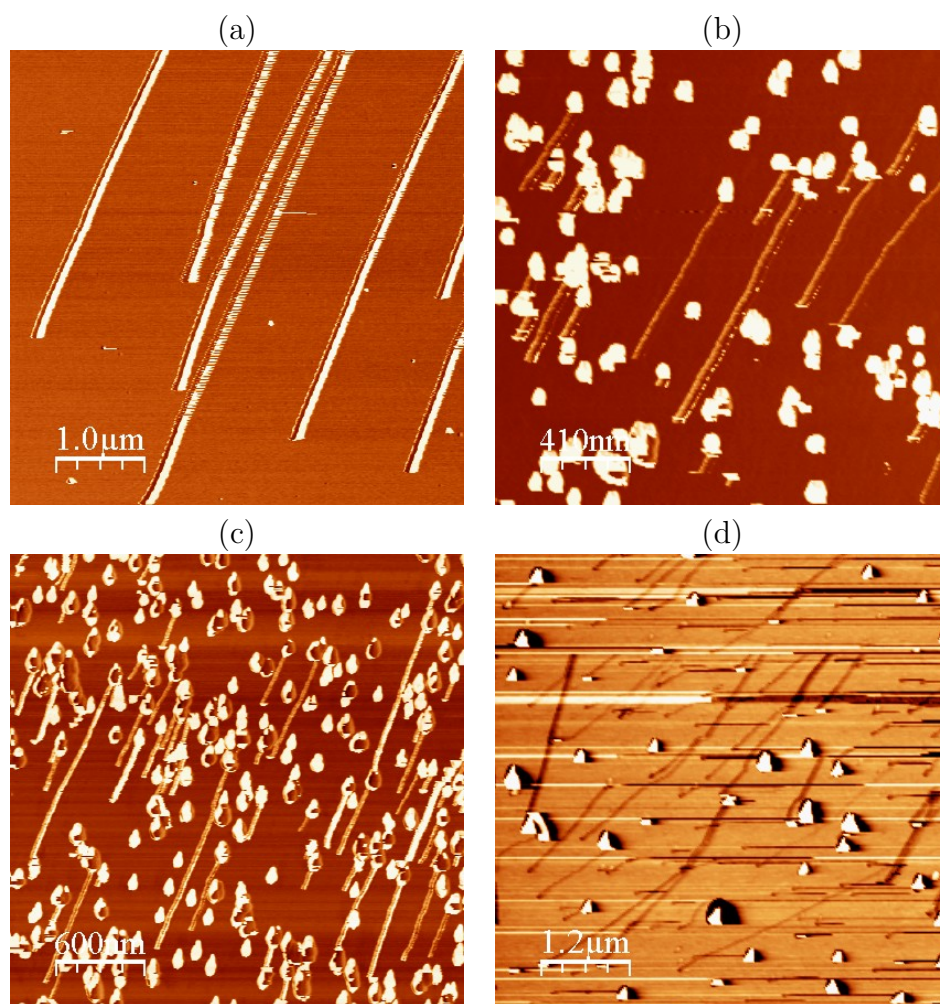


**Figure 3.6:** Manipulation of Au particles on plain Si with different spacings. (a)spacing - 9.7nm. (b)spacing - 3.9nm. (c) spacing - 5.8nm. (d)spacing -11.7nm

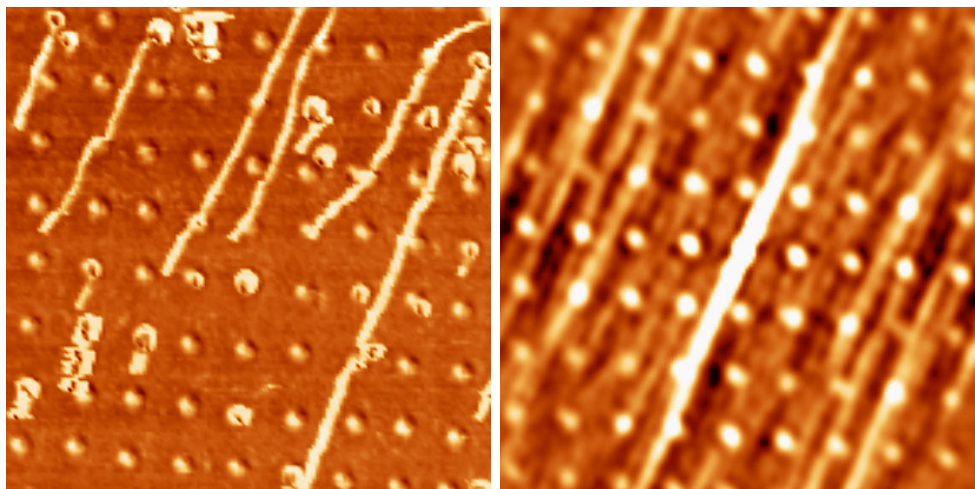


**Figure 3.7:** (a) Phase contrast of the gold nanoparticles manipulated on the surfaces patterned with pits. The spacing  $b$  between consecutive scan lines is 7.8 nm. (b) 2D self-correlation image obtained by numerical integration of (a). Size of the images:  $1\mu\text{m}$ .

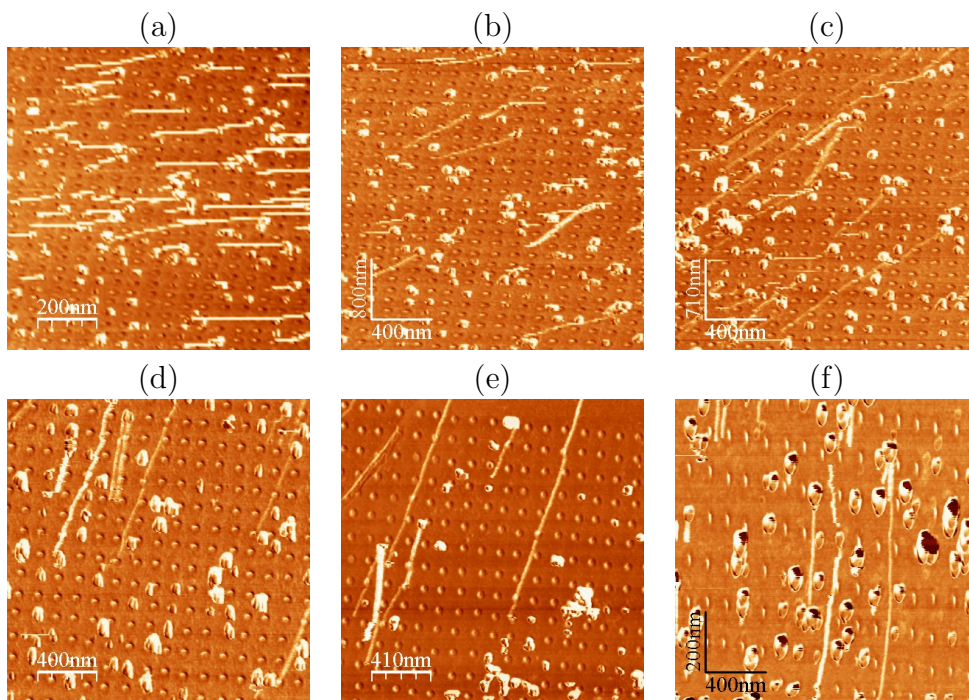


**Figure 3.8:** Manipulation of Au nanoparticles on pits with different spacings: (a) 21nm, (b) 16nm, (c) 9.7nm, (d) 5nm, (e) 3.9 and (f) 1.9nm

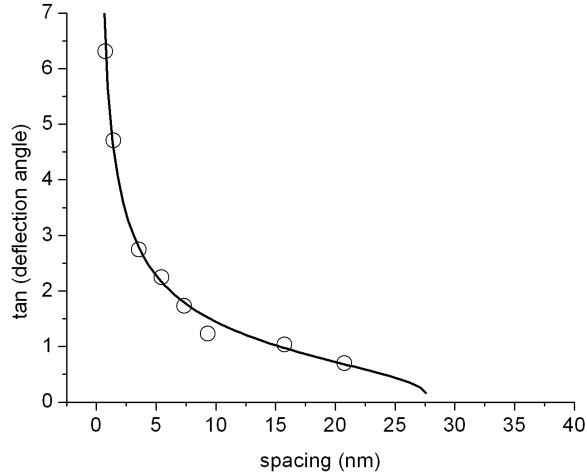


**Figure 3.9:** Experimental angle of deflection (open circles) and best fit of the experimental data (continuous line) obtained using equations (3.6) and (3.8)

is decreased from fig. 3.8(a) to fig. 3.8(f). The trend of higher angles with lower spacing is clear. To find the relation between the deflection angle and the spacing between the scan lines, the measured angles from fig. 3.8 were plotted against the spacing (*b*). The open circles in fig. 3.9 shows the trend of the tangent of the deflection angle with respect to the spacing between the scan lines and the solid line represents the theoretical fit using equations (3.6) and (3.8). The experimental results seem to be in good agreement with the theoretical calculations. To test this model further, Au nanoparticles were manipulated on different substrates.

### Manipulation on parallel grooves and HOPG surfaces

To further verify the model, particles were manipulated on the grooves (introduced in Chapter 1). The sample was rotated and manipulation experiments were repeated to check the influence of the deep grooves on the trajectory of the moving particle. It was found that even though the deep grooves slightly influence the direction of the particle movement, the particles tend to follow their preferential angle. This is in agreement to that predicted by our model. Fig. 3.10 shows AFM images of Au nanoparticles manipulated on patterned grooves. Similar situation was found in the case of nanoparticles moving on HOPG, the particles do not seem to be greatly influenced by the step edges but continued following the preferential angle during movement. Fig. 3.11 shows AFM images of Au nanoparticles manipulated on HOPG[91, 92].

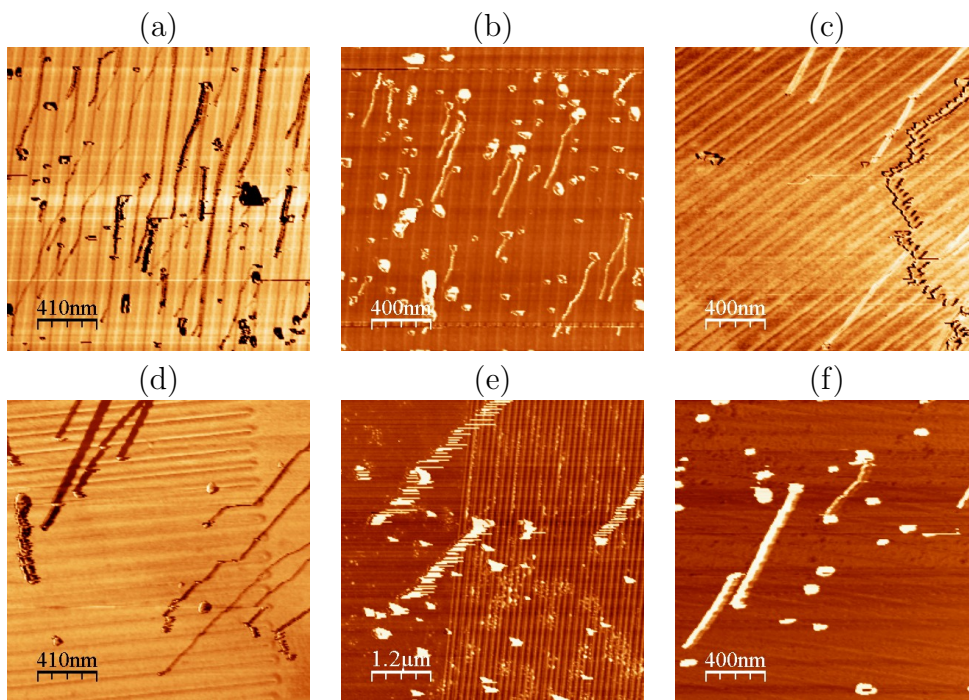


**Figure 3.10:** Phase images of nanoparticles manipulated on patterned Si by rotating the sample to check the influence on the trajectories.

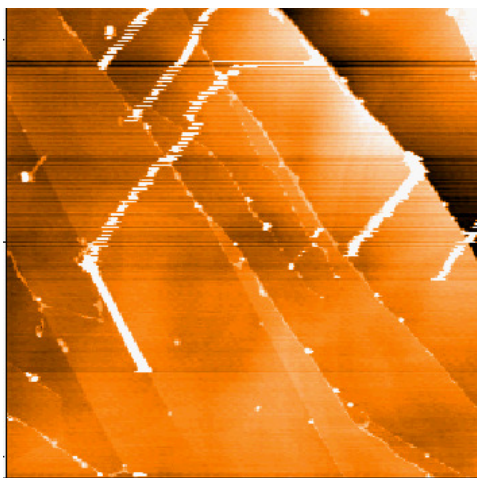


**Figure 3.11:** Nanoparticles moving on HOPG

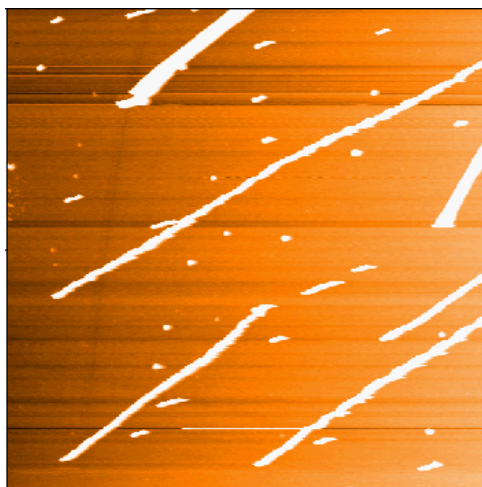


**Figure 3.12:** Manipulation of 50 and 100 nm Au particles (in equal proportion) on Si.

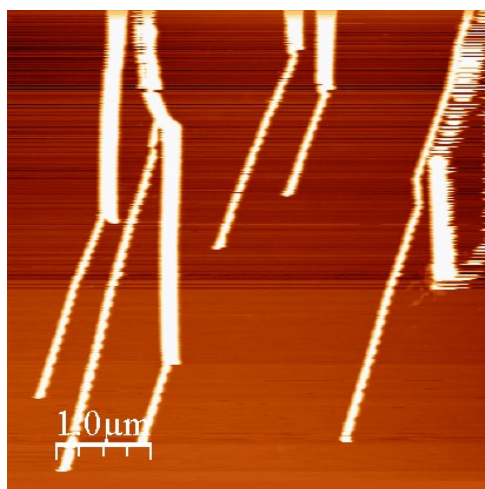


**Figure 3.13:** Movement of 100 nm Au particles on Si. Spacing 9.7 nm

### 3.1.3 Manipulation of a nanoparticle mixture

A sample containing an equal ratio of 50 and 100 nm Au nanoparticles was prepared to check the difference in their trajectories after moving. Fig. 3.12 shows that 50 nm particle moves at a smaller angle as compared to 100 nm particle. It was also seen in many cases that two particles collide at a point and move together as a single larger particle. Fig. 3.13 shows that the single Au particle (thinner line) moves at a smaller angle as compared to when it meets another particle (thicker line). The reason for this can be explained from eq. 3.8, which shows that the trajectories of the particles depends on the spacing as well as the parameter ' $R$ ' which is the sum of the radii of the tip and the particle. This means that particles with different radii would be displaced by a different angle.

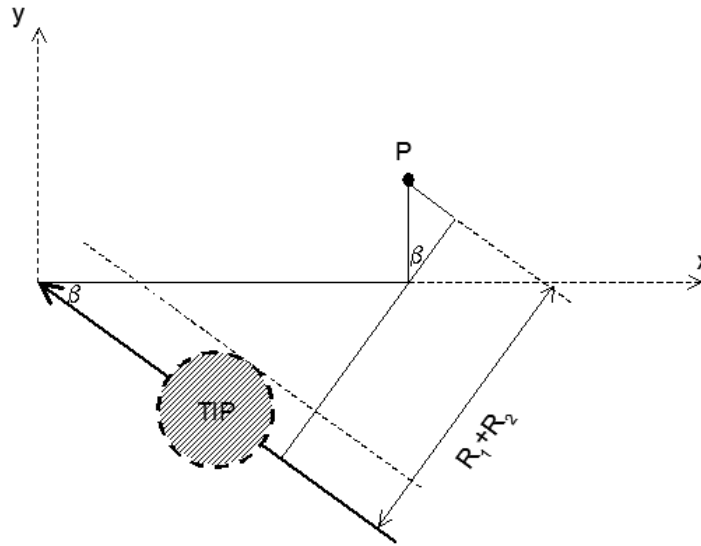


**Figure 3.14:** Position of a particle (P denotes its center) at the end of a backward scan. The angle  $\beta$  is exaggerated.

### 3.1.4 Angle of deflection in case of zigzag scanning path

In applying this method, one should be aware that some commercial instruments adopt a zigzag scanning path different from the typical pattern in fig. 3.1(a). In such cases, the angle of deflection of the particles (with the same size) will not be the same, but will depend on the coordinate  $x$  of the particle along the fast scan direction. An example is given in fig. 3.14, where the angle of deflection continuously increases from right to left. The direction of motion of the tip ( $x'$ ) is tilted of an angle  $\beta = \arctan(b/2L) \simeq (b/2L)$  with respect to the fast scan direction  $x$ , where  $L$  is the scan size. At the first impact with the tip, the coordinates  $x$  and  $y$  of the particle are related by

$$y = R - \frac{bx}{2L} \quad (3.12)$$

(see fig. 3.14). In a frame of reference tilted of an angle  $\beta$  with respect to  $xy$ :

$$x' = x \cos \beta + y \sin \beta$$

$$y' = -x \sin \beta + y \cos \beta$$

and taking into account the relation (3.12):

$$x' = x + \frac{Rb}{2L}$$

$$y' = R - \frac{bx}{L}$$

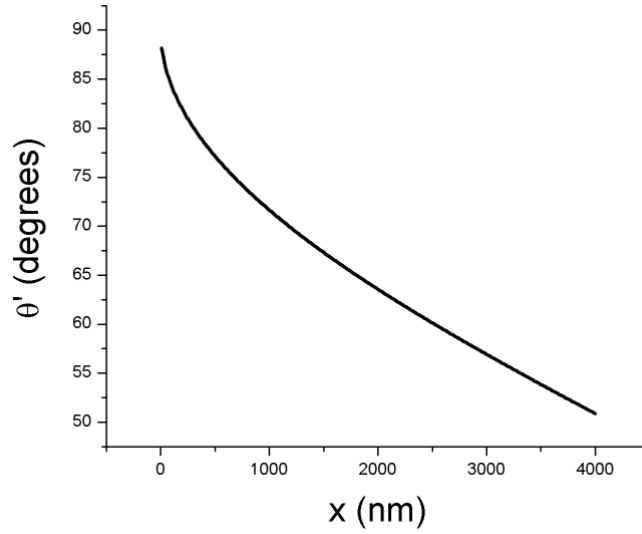


**Figure 3.15:** Angle of deflection of a nanosphere pushed in the forward segment of a zigzag scan path. Here  $R = 22.5$  nm,  $L = 4$   $\mu\text{m}$  and  $b = 10$  nm

The angle between tip and particle at the first impact,  $\alpha_0$ , is now replaced by the angle

$$\alpha'_0(x) = \arcsin\left(1 - \frac{b}{R} \cdot \frac{x}{L}\right)$$

The displacement  $\Delta x'$  of the particle along  $x'$  is still given by (3.7), whereas the displacement  $\Delta y' = R - y' = bx/L$ . As a result, the particle is deflected by an angle

$$\tan \theta' \equiv \frac{\Delta y'}{\Delta x'} = -\frac{b(x/L)}{R \left( \cos \alpha'_0(x) + \log \tan \frac{\alpha'_0(x)}{2} \right)}$$

with respect to the direction  $x'$ . This angle depends on the particle position. The function  $\theta'(x)$  is plotted in fig. 3.15 for the case  $R = 22.5$  nm,  $L = 4$   $\mu\text{m}$  and  $b = 10$  nm. It tends to  $90^\circ$  when  $x \rightarrow 0$  and to  $\theta(b)$  when  $x \rightarrow L$ . In the same way we can estimate the angle of deflection  $\theta''(x)$  with respect to the backward scan direction. From the vectorial sum of the particle deflection in forward and backward direction we can finally determine the total angle of deflection  $\theta(x)$ . The angle distribution of  $\theta$  is centered around  $\theta = 90^\circ$ , and reaches the extreme values  $\theta_{min} = 180^\circ - \theta(b)$  and  $\theta_{max} = \theta(b)$  when  $x \rightarrow 0$  and  $x \rightarrow L$  respectively as shown from fig. 3.15. With the spacing used in fig. 3.16 ( $b = 11.7$ nm) and  $R = 22.5$ nm, we estimate  $\theta_{min} = 61^\circ$  and  $\theta_{max} = 119^\circ$ . These values are in qualitative agreement with the experiment.



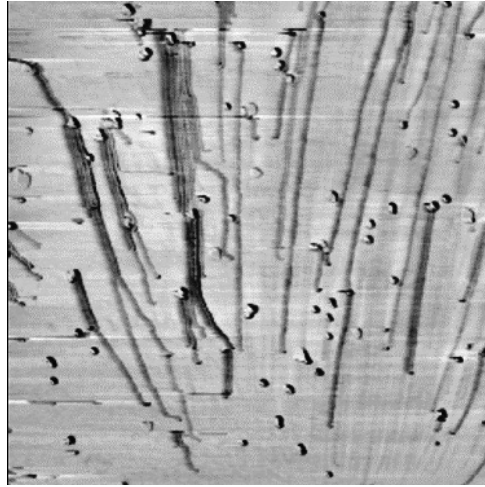


**Figure 3.16:** Typical trajectories of gold nanoparticles on a silicon substrate observed when the probing tip moves along a zigzag path. Scan size:  $3\mu\text{ m}$ .

## 3.2 Trajectory fluctuations accompanying the manipulation of spherical nanoparticles

In the previous section, the relation between the trajectories of the moving particles with the spacing between scan lines was described by using a model. Now we extend the use of this model to study the influence of friction on the trajectories of nanoparticles pushed by an AFM tip. In tapping mode AFM, the probing tip oscillates at a certain frequency close to the resonance of the free cantilever support and provided that the oscillation amplitude is high enough, the particle is displaced after collision with the tip. This displacement could vary depending on the friction between the particle and the surface which is influenced by the nature of the substrate, particle and the energy dissipated by the tip to the particle etc. Nanotips sliding on NaCl(100) surface (without particles) usually jump with the periodicity of the lattice constant of the substrate [62]. Ritter et al performed manipulation experiments of antimony particles on graphite and molybdenum disulfide [56] where they assumed that the distance of a jump of the particle corresponds to the lattice constant  $a$  of the substrate. However, it is questionable whether nanoparticles, pushed by a vibrating tip on a silicon oxide surface, should behave in the same way as the above cases.

In order to answer this question, a different approach to precisely determine the mean displacement  $d$  of spherical nanoparticles pushed by an AFM tip in tapping mode was adopted. The trajectories of the nanoparticles were reproduced by computer simulations and the effect of friction on them was studied. This was experimentally verified.

### 3.2.1 Simulations

Trajectories of the particles in two dimensions were reproduced by computer simulations. For this, only the sections of the tip and the particle at their point of contact was considered. The model which was introduced in the first section of the chapter was extended to study the influence of friction on trajectories. Listed below are the basic assumptions of the model which will be used for the simulations.

It was assumed that

- (1) The AFM is operated in tapping mode, and that the oscillation amplitude of the tip is large enough to set the nanoparticles into motion[59].
- (2) Due to the finite friction force  $f$ , a particle is displaced of a quantity  $d$  at each collision with the tip apex.
- (3) The particle slides without rolling[63]

In order to reproduce the trajectories, the values of radius of the tip and sample were taken such that they are comparable to the experimental values. On the first scan line, the particle is positioned such that its distance from the first scan line takes a random value between 0 and  $R$ . The tip moves forth and back along the  $x$  axis, and it is shifted of a quantity  $b$  (spacing between scan lines) along the  $y$  direction at each scan line. At each collision with the tip, the particle is displaced of a quantity  $d$  along the straight line joining the centers of tip and particle. The displacement  $d$  can be simply related to the kinetic energy  $E_{kin}$  acquired by the particle by the relation  $mv^2 = 2f$ , where  $m$  is the particle mass and  $v$  is the velocity of the particle immediately after the collision with the tip. Depending on the value of  $d$ , the oscillation frequency  $\omega$  of the cantilever, the scan velocity  $v_s$ , and the tip and particle size, the particle will experience a certain number of collisions along each scan line, varying between zero and  $\sim \omega R/v_s$ , where  $R$  is the sum of the radii of the tip and particle sections taken at the contacting point. If the particle radius  $R_p < R_t(1 - \sin \gamma)$ , where  $R_t$  is the tip radius and  $\gamma$  is the semi-aperture angle of the tip cone, the quantity  $R$  is twice the geometric average of tip and particle radii:  $R = 2\sqrt{R_p R_t}$ . Otherwise, a more complicated relation can be found, as described in the first section of the chapter.

The trajectories were plotted for different values of the parameter  $d$ . Fig. 3.17 shows two trajectories corresponding to different values of the parameter  $d$ . For the spacing between consecutive scan lines a typical value  $b = 15$  nm was chosen. If  $d \ll b$  the particle trajectory is quite regular, except for the first scan line, where the tip touches the particle at an arbitrary angle (fig. 3.17(a)). However, the situation changes when  $d$  is in the order of  $b$  or larger. In such a case, the particle trajectory is fluctuating and apparent discontinuities, i.e. scan lines without collisions between tip and particles, can be observed

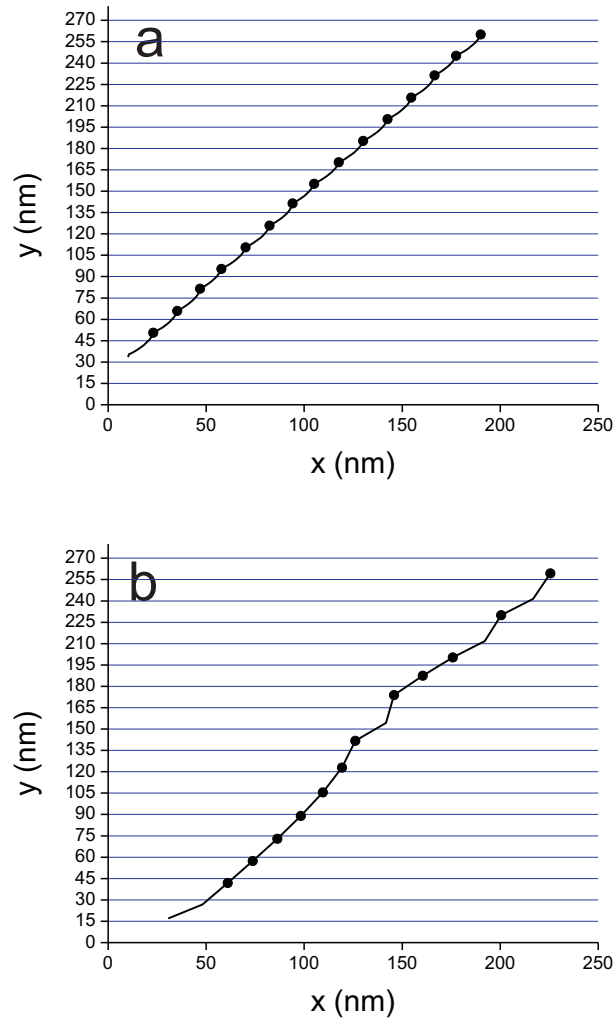


**Figure 3.17:** Simulated trajectories of a nanosphere pushed by an AFM tip in tapping mode. The center of the tip follows the horizontal lines which are separated by a distance  $b = 15$  nm. The sum of the radii of the sections of tip and particle (at their contact point) is  $R = 35$  nm and the displacement of the particle after collision is (a)  $d = 2$  nm and (b)  $d = 20$  nm. The black dots represent the particle position at the end of each scan line.

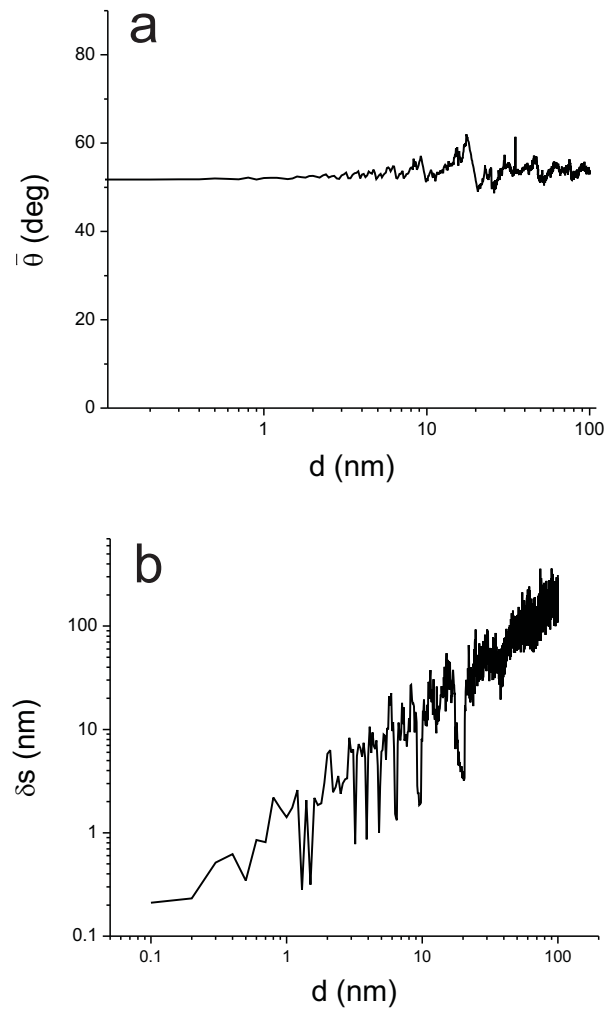


**Figure 3.18:** (a) Average angle of deflection and (b) fluctuations of the trajectories of spherical particles plotted as a function of the 'mean path'  $d$  of the nanoparticles. The parameters  $R$  and  $b$  have the same values as in fig. 3.17

(fig.3.17(b)). In order to have a better understanding of the influence of friction on the trajectories, average slope and fluctuations were plotted as a function of  $d$ . fig. 3.18(a) shows the average slope of the particle trajectory as a function of the displacement  $d$  (with the same values of  $R$  and  $b$  used in fig. 3.17). With these parameters, the average value of the deflection angle  $\bar{\theta}$ , takes always a value of about  $52^\circ$ , except in the range  $b \sim d$ . The deflection angle is not influenced by the value of  $d$ . The fluctuations of the particle direction from the straight line defined by  $\bar{\theta}$  have also been calculated. In fig. 3.18(b) the fluctuations are defined by the root mean square  $\delta s$  of the distance between the points forming the trajectory and the straight line, which is plotted as a function of the displacement  $d$ . In contrast to the average direction  $\bar{\theta}$ , the fluctuations  $\delta s$  present a strong dependence on  $d$ . As shown in fig. 3.18(b), the fluctuations  $\delta s$  are proportional to the displacement  $d$  in the range of values considered in the simulation (up to  $d = 100$  nm). From a fit of the curve shown in fig. 3.18(b) it turns out that  $\delta s \simeq d$ . However, this is not the case in a few isolated dips and in the region  $d \sim b$ , where the fluctuations are significantly smaller. In case of infinitely large friction, the trajectories are well reproduced by an analytical formula, which was introduced in the first section of this chapter. and it was seen that the fluctuations of the trajectories (but not their average directions) are significantly affected by friction. The larger the friction force  $f$  between particles and surface, the more regular the trajectories.

The angle of deflection of a spherical particle has been calculated the first part of the chapter, in the limit case  $d \rightarrow 0$ . For the sake of completeness it is shown below. Assuming that the adhesion between substrate and particles is strong enough to prevent any further displacement of the particle after the collision with the tip, it is showed that

$$\tan \theta = -\frac{b}{R \left( \cos \alpha_0 + \log \tan \frac{\alpha_0}{2} \right)},$$

where  $\alpha_0$  is the impact angle between tip and particle. For a raster scan path the impact angle

$$\alpha_0 = \arcsin \left( 1 - \frac{b}{R} \right),$$

except for the very first scan line.

The results in fig. 3.18(a) show that the average deflection of the particle does not change by increasing  $d$ , except in the region  $d \sim b$ . We can explain this result as follows. When  $d \rightarrow 0$  the particle and tip meet each other at the same relative position, defined by the impact angle  $\alpha_0$ , in every scan line except the first one. By increasing  $d$  the impact angle is different in every scan line. Depending on  $b$ , angles below and above  $\alpha_0$  are expected. As it turns out from our numeric results, the distribution of the impact angles around  $\alpha_0$  is well balanced, except when  $d \sim b$ . Other simulations have showed that, when  $b \ll R$  significant deviations are observed if  $d = nb$  or  $d = b/n$ , where  $n$  is a small integer number. In such a case, the tip and particle will meet each other at an angle  $> \alpha_0$ , which is approximately the same in every consecutive line. When  $b \sim R$ , as in fig. 3.18, this ‘interference’ effect is still present, although it is significantly smoothed out. Without

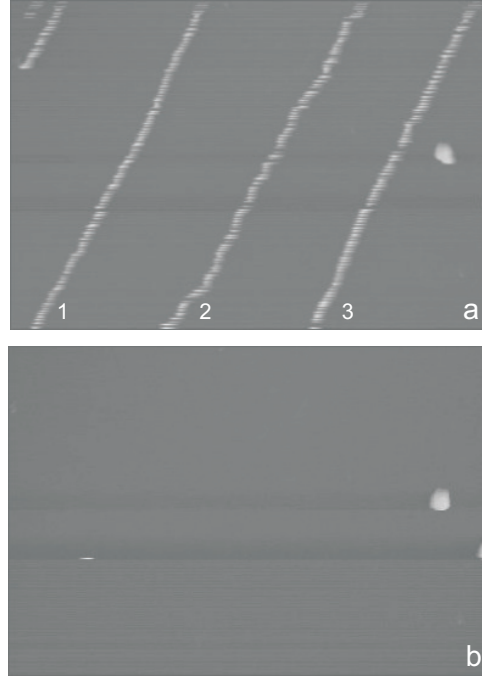


**Figure 3.19:** (a) Forward and (b) backward topography images showing the trajectories of gold nanospheres pushed by an AFM tip on a silicon surface in tapping mode (frames size:  $3.85 \times 2.65 \mu\text{m}^2$ ). The particles have a radius of 25nm and the distance between consecutive scan lines is  $b = 7.8\text{nm}$ .

knowing the friction force, the mean distance  $d$  travelled by the particles after a collision can be simply estimated from the fluctuations observed in the AFM measurements.

### 3.2.2 Experimental Results

In order to test the model and to estimate the parameter  $d$  in real cases, gold nanoparticles with 50 nm diameter (PGO-50, G. Kisker GbR, Germany) were manipulated on flat silicon surfaces under ambient conditions (RH 40%). A commercial AFM (Nanite™, Nanosurf AG, Switzerland) operated in tapping mode has been used.

The nanoparticles move with the same angle of deflection (as shown in the first section of the chapter) but there are discontinuities and fluctuations in the trajectories. The path of the nanoparticles is clearly revealed in the forward traces of the topography signal (fig. 3.19(a)). In fig. 3.19(a) the nanoparticles have an apparent height of 30-35 nm, indicating that they are displaced before the tip reaches the top of the particles. When the tip is scanned backwards, the mobile particles do not appear at all (fig. 3.19(b)), meaning that they are completely pushed away from the scan 'corridor' when the tip moves forwards. The mean angle of deviation  $\bar{\theta}$  of the three particles enhanced in fig. 3.19 is  $62^\circ$  and their trajectory fluctuations  $\delta s$  are 19.5, 22.8 and 20.4 nm respectively. From the value of (with  $b = 7.8\text{nm}$ ), the value of  $R$  is estimated to be 64 nm using Eq. 3.6 and 3.8, and, running

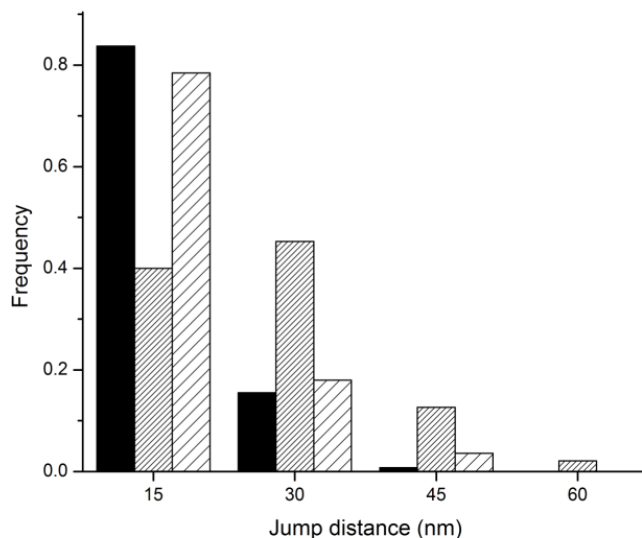


**Figure 3.20:** Statistic distribution of the discontinuities in the trajectories of the three particles enhanced in fig. 3.20(a). The average value of the discontinuities is 20.6nm.

simulations with these values of  $\delta s$  and  $R$ , value of  $d = 20$  nm is obtained for the mean displacement of the particles. It can be noted that this value is much higher than the lattice constant of the substrate ( $\sim 0.5$  nm).

Several discontinuities can also be noticed in the particle trajectories. The exact condition for the appearance of a discontinuity is,

$$D(i) = [y_{i+1}/b] - [y_i/b] > 1 \quad (3.13)$$

where  $i$  enumerates the collisions between tip and nanoparticles and the square bracket denotes the integer part of a real number.

In fig. 3.20 the histograms of the functions  $D(i)$  corresponding to the three particles in fig. 3.19(a) is shown. The average values of the discontinuities are 17.6, 26.5 and 18.8 nm respectively, i.e. in the same range of the displacement  $d$ . From numeric simulations with  $d = 20$  nm,  $R = 64$  nm and  $b = 7.8$  nm we obtain a value 15.6 nm for the average discontinuity. Although measuring the apparent discontinuities in the particles trajectories may be an easier method to evaluate the mean path of the nanoparticles after collision, it appears less reliable than measuring the fluctuations.

### 3.3 Conclusions

In the first part of the chapter an analytical formula, which relates the angle of deflection of spherical nanoparticles pushed by an AFM tip to the geometry of tip and particles, and

the pattern followed by the tip in the most common cases of raster scan path and zigzag scan path was introduced. This formula can be applied to separate nanoparticles according to their size, with potential applications in drug delivery, nano-optics, catalysis and environmental issues. In the second part of the chapter, effect of friction on the trajectories of spherical nanoparticles pushed by an AFM tip on a flat surface was studied. The model introduced in the first part of the chapter has been applied to determine the mean path of gold particles on silicon in air, which turned out to be significantly larger than the lattice constant of the substrate. Since the velocities of the particles immediately after a collision are basically unknown, the friction force between particles and surface could not be quantified. This drawback may be overcome once the collision process between tip and particle is better understood, for instance by measuring the amplitude variations of the cantilever oscillations in real time and/or by modeling the tip-particle-interactions by combinations of molecular dynamics and continuum mechanics. The assumption that the particles slide without rolling needs also be better established. Ritter et al. showed that this hypothesis that the particle slides without rolling is valid in the case of latex nanospheres (with radii of a few tens of nm) manipulated on HOPG after the orientation of the spheres had been marked by slight indentations made by the AFM tip [63]. Unfortunately, this cannot be done on gold nanoparticles. Furthermore, smaller objects such as C60 molecules were reported to roll in STM manipulation experiments on Si(100) [64]. Ongoing theoretical works on spherical clusters have shown that both sliding and rolling regimes are expected, depending on a delicate balance between the model parameters [65, 66]. Manipulation experiments on particles with different shapes may help to shed light into this puzzling question. Apart from the shape of the nanoparticles, surface and environmental properties like roughness [67], humidity [68], and chemical functionalization [59] play an important role in manipulation experiments at room temperature. For instance, a moderate adhesion between tip and particle may increase the value of the parameter  $d$ . Altogether, these effects must be taken into account in future extensions of our model.





# Chapter 4

## Manipulation of Gold Nanoparticles: Influence of Surface Chemistry, Temperature, and Environment

Mechanical control of nanometer size objects and the dynamic behavior at this length scale are subjects of growing interest. One promising approach to operate and perform quantitative measurements in this regime is to use dissipation processes in atomic force microscopy. In this chapter, different factors which affect the manipulation of gold nanospheres will be studied. Manipulation of gold nanospheres on silicon dioxide and a measurement of the energy depinning threshold as a function of surface chemistry, temperature and humidity was done by using the AFM microscope in dynamic mode[59]. For these studies, Au nanospheres either raw or coated with self-assembled monolayers ending with a hydrophobic (methyl, -CH<sub>3</sub>) or hydrophilic group (hydroxyl, -OH) were used. The role of the environment and thermal activation on the mobility of the nanospheres was studied by performing manipulation experiments in ultra high vacuum conditions, ambient conditions and also at different temperatures, ranging from 20° up to 150° C. Described below is the nature of the nanoparticles used.

### 4.1 Nanoparticles Used : Raw vs Functionalized nanoparticles

In order to study the influence of the surface chemistry of Au nanoparticles on manipulation, two different kinds of nanoparticles were used, which are described below.

#### 1. Raw Gold Nanoparticles:

The colloidal suspension was made by reduction of an aqueous solution of nanogold

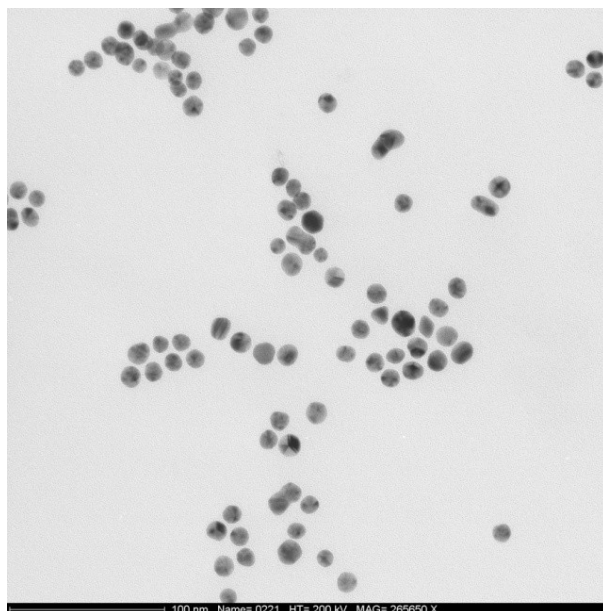


**Figure 4.1:** TEM image (400 nm  $\times$  400 nm) of 25 nm diameter gold nanoparticles.

particles (as described in chapter 2 ) by Dr. K. Mougin. The average size of these nanogold particles, as determined from transmission electron microscopy (TEM) images, was  $25 \pm 5$  nm (fig. 4.1). In the following sections, these nanocolloidal particles directly obtained from synthesis will be referred to as raw nanoparticles (raw NPs), although they bear some residual stabilizing citrate ions which impart to them a net hydrophilic nature.

## 2. Functionalized Gold Nanoparticles:

Dodecanethiol for methyl-terminated monolayers (referred to as  $CH_3$ ) and 11-mercapto-1-undecanol for the hydroxyl groups (referred to as OH) were provided by Sigma-Aldrich and used as received. Hydroxyl-stabilized or methyl-thiol-stabilized gold nanospheres were synthesized according to a modified version of two common synthesis.[69] The raw nanosphere solution was centrifuged at 7000 rpm for 20 min to pellet the nanoparticles, decanted, and then resuspended in 1 ml of DI water to reduce the citric acid concentration. The nanoparticles were then purified from surfactant excess and other reactants by dialysis during one week. Finally, the dialyzed solution was centrifuged and particles were redispersed in tetrahydrofuran. An amount of 300  $\mu$ L of the expected thiol (methyl- or hydroxyl-terminated) was added to the solution. It was sonicated and stirred for approximately 2 h to allow the grafting reaction to reach completion. The solution resulted in a slow color change from yellow to

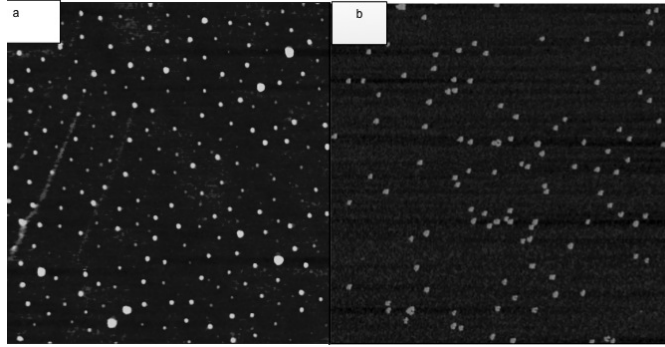


**Figure 4.2:** AFM images of 25 nm diameter gold nanoparticles deposited onto a silicon wafer: (a) controlled organization as described in the text and (b) random distribution. Frame sizes: 3 and 1  $\mu\text{m}$ , respectively.

transparent, and then it was stored at  $4^\circ\text{C}$  until use. The average diameter of the synthesized nanoparticles is  $25 \pm 5$  nm.

## 4.2 Nanoparticle Adsorption : Random vs Geometrical organization

In order to study the influence of the organization of the nanospheres on their mobility, two different techniques were used to adsorb the gold nanospheres on the substrate.

### 1. Random Adsorption:

For the adsorption experiments, a unique concentration of 0.03 wt % nanoparticles in the aqueous or organic dispersion was used. The experimental protocol basically involved particle adsorption by immersing the samples for around 20 min in the suspension bath, whose temperature was maintained at  $20 \pm 1^\circ\text{C}$ . Upon this initial adsorption stage, the samples were removed from the bath, and the thick dispersion film remaining on the substrates was allowed to dry.

### 2. Geometrical Organization:

Samples were provided by McFarland's group at the University of California Santa Barbara (UCSB). The 25 nm diameter Au nanoparticles were synthesized as discussed previously [73, 74, 75]. The Au NP-coated silicon wafer was prepared using a micelle encapsulation method [70, 71]. Au nanoparticles were encapsulated by the diblock copolymer polystyrene-block-poly(2-vinylpyridine). The solution was deposited onto the silicon wafer and dried under nitrogen flow. After being dip-coated, the polymer was removed using an oxygen plasma treatment (fig. 4.2).

## 4.3 Manipulation Setup : Air vs UHV

The influence of humidity was studied by performing manipulation experiments in air and UHV.

### 1. Air Measurements:

The images in air were acquired with two commercial atomic force microscopes (Multimode, Nanoscope IV from Veeco and Mobile S from Nanosurf). Rectangular silicon cantilevers with resonance frequencies,  $f_0$ , around 120 and 190 kHz, quality factors around 800 and 600, and nominal spring constants of 5 and 48 N/m (respectively, MPP12100 from Veeco and PPP-NCLR from Nanosensors) were used.

### 2. UHV Measurements:

The images in UHV were acquired with a home-built atomic force microscope [72]. The base pressure was below  $10^{-9}$  mbar. Due to the high quality factor in UHV, the frequency shift from the out-of-contact resonance, and not the oscillation amplitude of the tip, was used as the imaging parameter (NC-AFM). Measurements in the contact mode were also done, where the set point is determined by the normal load acting between the tip and sample. PPP-NCLR and CONT cantilevers from Nanosensors were used in the two cases.

## 4.4 Experimental Results

### 4.4.1 Effect of surface chemistry on the manipulation of nanoparticles

Manipulation of both raw and functionalized Au nanoparticles was done to study the influence of the nature of nanoparticle surface.

- **Manipulation of raw Particles on Silicon**

In the first series of measurements, a silicon sample was dipped into a colloidal solution of raw nanoparticles, dried, and repeatedly scanned at increasing excitation amplitude (fig. 4.3). When a certain value of the amplitude was overcome, the particles started to move. The motion of the particles consisted of either abrupt jumps along the fast scan direction (circle in fig. 4.3(b)), smooth translation almost along the slow scan direction (ellipse in fig. 4.3(c)), or a combination of both (ellipse in fig. 4.3(b)). As a result, the gold particles were found to be aligned at two edges of the scanned area (fig. 4.4). Fig. 4.5 shows the phase shift images corresponding to fig. 4.3. According to eq. (1.4), the brighter and darker areas in fig. 4.5 correspond

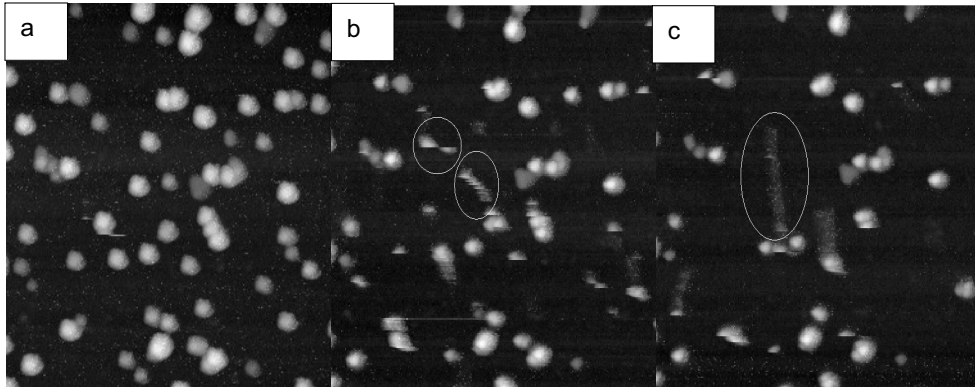


**Figure 4.3:** Gold particles on silicon. The same area was imaged several times while increasing the excitation amplitude of the cantilever between each scan. When the particles move smoothly, only the upper part of them is imaged, which results in an apparent lower height of them. Frame size:  $2 \mu\text{m}$

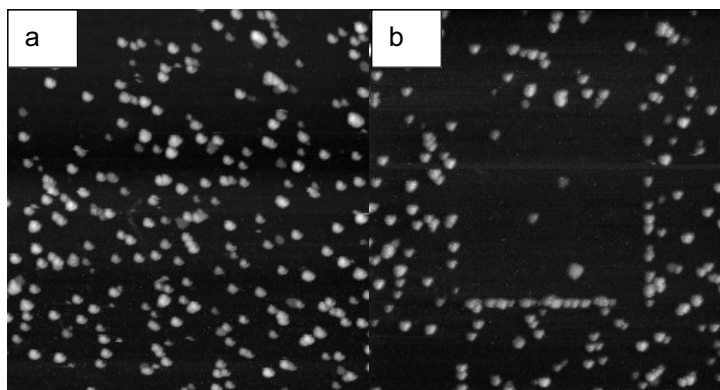


**Figure 4.4:** Zoom out of the area in fig. 4.3(a) before and (b) after scanning downward, starting from left to right. The particles accumulate at two edges of the area. Frame size:  $4 \mu\text{m}$ .

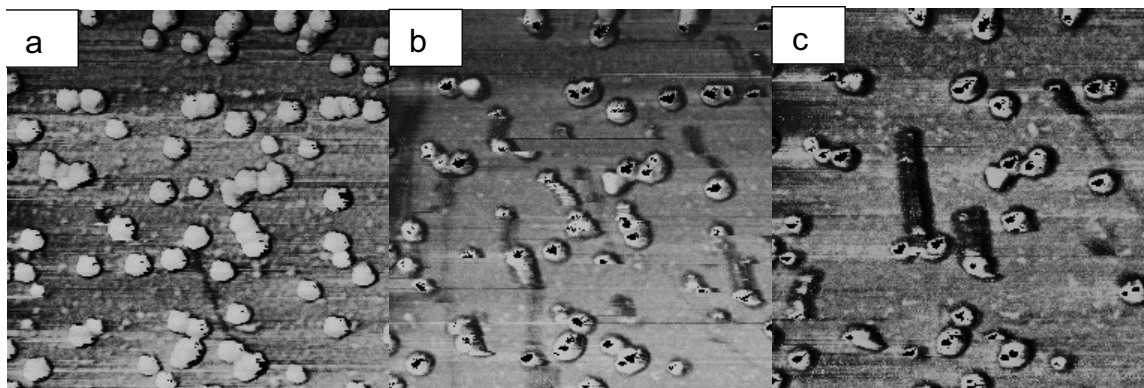


**Figure 4.5:** Phase shift images corresponding to fig. 4.3. The dark spots on the top of the particles correspond to the phase signal switching from  $+180^\circ$  to  $-180^\circ$  and do not have any special physical meaning.

to regions with higher and lower power dissipation, respectively. From the images, it turns out that the power dissipation is higher on the fixed particles compared to the silicon substrate. However, the dissipation becomes much lower when the particles start moving. This can be understood assuming that the particles sticking on the substrate are not rigidly fixed and that they dissipate energy in the vibrations induced by the AFM tip. From eq. (1.4), we estimated an average power dissipation of  $8 \times 10^{-11}$  W/particle, which is consistent with the values reported by Ritter et al. on flat antimony particles.[56]. For these raw NPs bearing residual stabilizing citrate ions, one can reasonably suppose the existence of an adsorbed thin water film at the NP/substrate interface under ambient conditions which acts as a lubricant layer, lowering the adhesion and therefore the energy required (dissipated) in moving these particles. As compared to these ambient humidity results, the absence of humidity while working under ultrahigh vacuum rather favors the adhesion of raw (citric-coated) nanoparticles with the silicon substrate, leading to a higher dissipated energy.

- **Manipulation of functionalized Particles on Silicon**

As a next step, we investigated the role of hydrophobicity in the manipulation process by coating the gold nanoparticles with OH- and CH<sub>3</sub>-terminated thiol groups, as described in the previous section, and moving the particles again on a flat silicon substrate. The results summarized in fig. 4.6, which shows the average power dissipation required to start the motion of the particles, indicate that the presence of a hydrophobic interface significantly enhances the mobility of the particles. The energy required to move OH-coated nanogold particles is more than 10 times higher than the energy required to move CH<sub>3</sub>-coated particles. We also observed that the manipulation of hydrophilic coated nanoparticles often results in damage to the tip due to the high adhesion forces at the interface. This strong adhesion between the

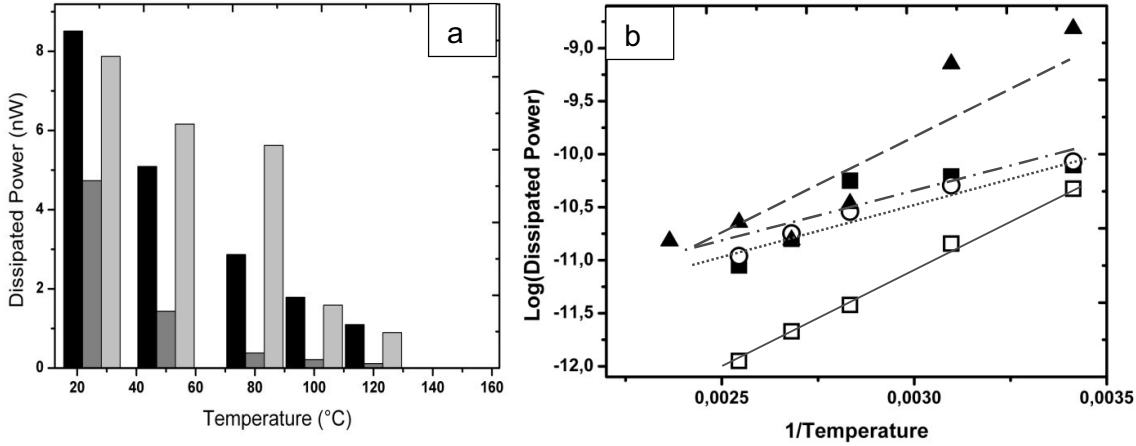


**Figure 4.6:** (a) Average power dissipation accompanying the onset of motion of raw and coated nanoparticles on silicon in air versus temperature: (black column) raw NPs that are uniformly distributed on the substrate, (dark gray column) CH<sub>3</sub>-coated NPs, and (light gray column) raw NPs that are randomly distributed on the substrate. (b) Logarithm of the dissipated power in moving raw and coated NPs on a silicon wafer versus the inverse of temperature for (■) raw nanoparticles, (○) raw nanoparticles geometrically organized, (□) CH<sub>3</sub>-coated nanoparticles, and (▲) OH-coated nanoparticles.

silicon substrate and hydrophilic coated nanoparticles which primarily arises from intermolecular interactions may also involve a contribution from capillary bridges which form under ambient conditions between the substrate and the NPs on one hand, and between the NPs on the other hand. In contrast, the thin adsorbed water film which forms on the silicon wafer acts as a lubricant when confined between the hydrophobized CH<sub>3</sub>-coated nanoparticles and the hydrophilic substrate, as has already been observed.[76, 77, 78, 79]

#### 4.4.2 Temperature Effects

Fig. 4.6(a) represents a histogram of the raw data of power dissipation versus temperature, for temperature ranging from 20 to 150°C. This figure shows in all cases that power dissipation decreases with temperature, and this effect appears to be stronger on hydrophilic particles. Intuitively, one could expect this result, since the temperature (thermal energy  $kT$ ) acts as an obstacle in forming stable intermolecular bonds and water bridges between the particles and substrate, reducing the adhesion between them. Similar kinetic effects have been recognized in friction on hydrophilic surfaces measured with different scan velocities.[76, 77] It is worth noting that, during this temperature-dependent manipulation, no evident damage was observed on the working areas. Fig. 4.6(b) corresponds



to a logarithm plot of the dissipated power as a function of the inverse of temperature ( $1/T$ ). These experimental data display a good linear fit with  $R^2$  values higher than 0.90 for all NP/substrate couples, except for raw NPs (randomly distributed) for which the  $R^2$  value is 0.78. This linear behavior of  $\log(\text{dissipated power})$  versus  $(1/T)$  actually corresponds to an exponential decay of the dissipated power with  $T$  which accounts for a thermally activated process[80]. The slopes of these linear fits correspond to  $\Delta E_{act}/k$ , where  $\Delta E_{act}$  represents the variation of the activation energy  $\Delta E_{act}(T)$  with respect to a reference state  $E_0$ ,  $\Delta E_{act} = (E_0 - E_{act})$ , and  $E_{act}(T)$  represents the energy input involved in the motion of the particle. This energy variation (slope) is higher for the methyl-coated NPs, indicating a stronger decrease of the input energy with temperature, as one could expect for the lowest nanoparticle substrate adhesion. More surprising is the behavior of the OH-coated NPs which show a similar sensitivity of their mobility to temperature (strong decrease of input energy with  $T$ ). An explanation for this less expected behavior may come at least partly from the sensitivity of the adsorbed water layer to temperature in this more hydrophilic system. Finally, the raw particles have an activation energy lying in between those of the more hydrophilic and hydrophobic nanoparticles.

### 4.4.3 Organization Effects

The first and third columns in the series in Fig. 4.6(a) show the power threshold accompanying the motion of the randomly and geometrically organized distributions of nanoparticles, obtained as described previously. The power dissipation at different temperatures is comparable in both cases. This result can be explained by the average distance between nano-objects, which is 70 nm for the random distribution and 100 nm for the ordered one. At such a scale, the interparticle forces are of the order of long range interactions. The mobility of particles is essentially affected in this limit by electrostatic interactions arising from the residue of the synthesis of citric acid that may be adsorbed on the particles. It is thus normal in the absence of both physical contact and notable intermolecular forces between the particles that their mobility is independent of their organization (random or geometrically ordered). In other words, this result means that so long as the particle number density  $n_p$  is such as the interparticle distance  $d_p \sim (n_p)^{-1/2}$  is larger than the range of short-ranged forces, their mobility is not affected by their mutual interaction and is thus independent of their organization.

### 4.4.4 Vacuum Effects

Finally, we have investigated how the nanomanipulation process changes in the absence of humidity. The topography image in fig. 4.7 shows the gold particles on silicon after the sample was transferred in UHV without any further treatment, which could have changed the arrangement of the particles. The shapes of the particles are well defined, and the

structure of some aggregates can be recognized, due to the absence of convolution effects coming from the water layer which covers the particles under ambient conditions. In these conditions, the particles could not be moved, even when imaged at the maximum amplitude applicable with our system (in the order of 100 nm). Also, in contact mode, with forces of a few nanonewtons applied between the tip and particles, no motion was observed. This result particularly illustrates the lubricating role of the adsorbed water layer between the particle and the substrate in both the free (Brownian) and externally driven motion of the nanoparticles.

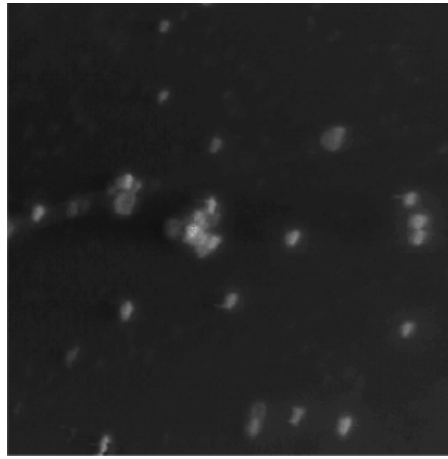


**Figure 4.7:** Gold nanoparticles on Si measured in UHV

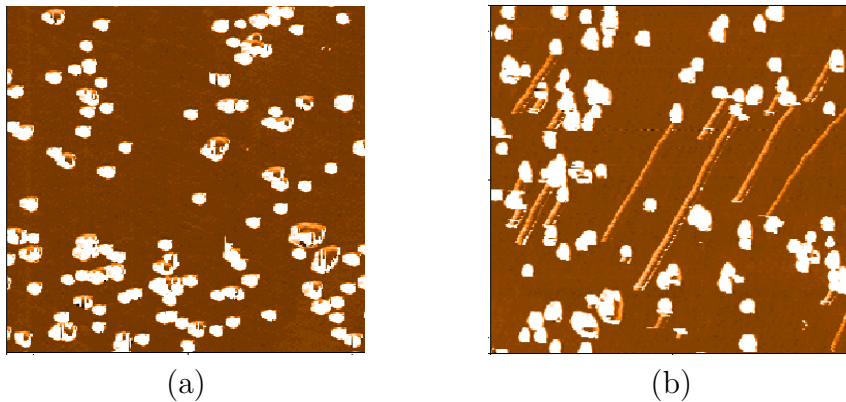


**Figure 4.8:** AFM images of Au nanospheres on Si (a) Imaged at 20nm and (b) Imaged at 24nm

## 4.5 Power dissipation : Moving vs Fixed nanoparticle

In order to verify whether fixed particles dissipate higher energy as compared to a moving particle during manipulation, some more experiments were done. Raw nanospheres were manipulated on Si and the energy dissipated by the tip on fixed and moving particles was calculated. The dissipation values obtained, was higher for the non-mobile particles as compared to the mobile ones. These results are not surprising because the movement is induced by operating the AFM in tapping mode with amplitude feedback (AM-AFM) and by using a tip amplitude oscillation intentionally larger than that optimized for imaging purpose. The extra energy transferred to the cluster physisorbed on the surface may cause its detachment and displacement. Whereas, in the case of non-mobile particle this energy is stored in the particle. Fig. 4.8 shows AFM images of Au nanoparticles on silicon dioxide surface. It can be seen that with a drive amplitude of 20nm (fig. 4.8(a), the particles do not move i.e. this amplitude is enough for imaging the nanoparticles but not for manipulation. Fig. 4.8(b) shows that with an amplitude of 24nm some of the particles start moving.

Using the same sample and tip, few more measurements were done by keeping all the

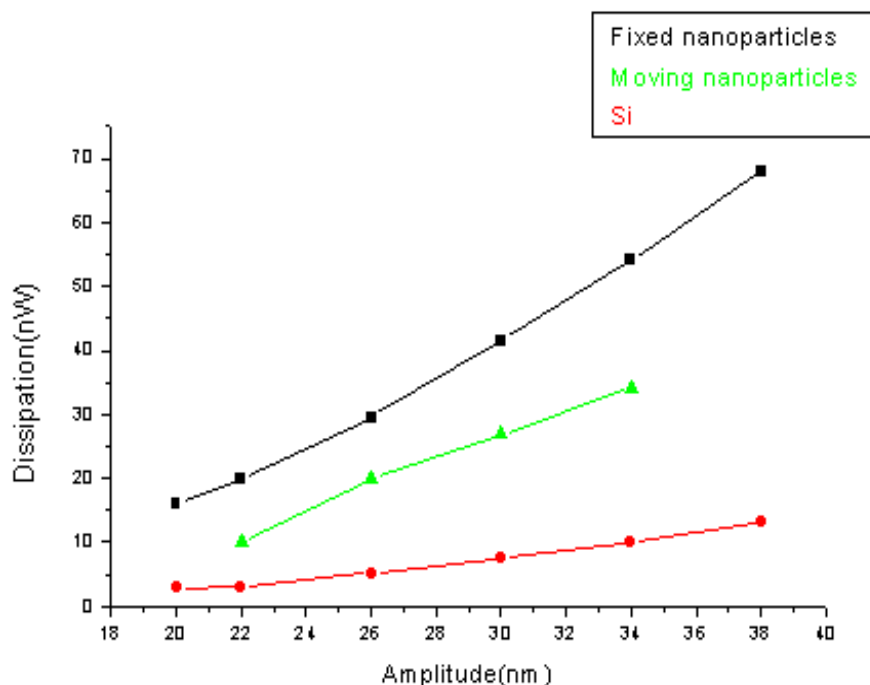


**Figure 4.9:** The energy dissipated by the tip during the manipulation of the nanoparticles is plotted as a function of amplitude.

---

other parameters constant but increasing the drive amplitude. In fig 4.9, the energy dissipation by the tip is plotted as a function of the drive amplitude. The red, green and the black curves represent the energy dissipated by the tip on the substrate, moving particles and fixed particles respectively . These measurements from fig. 4.9 systematically confirm the fact that the moving particles produce lower dissipation. However, theoretical (computational) work is needed to understand this behavior.

## 4.6 Conclusion

We performed systematic studies of the manipulation of gold nanoparticles considering different coatings, environments, and temperatures. In ambient conditions, the mobility of the particles is greatly enhanced by hydrophobic interlayers, formed by organic coatings deposited on the particles. In the absence of humidity, the gold particles strongly adhered to the silicon substrate, and manipulation could not be achieved. Thermal activation plays an opposite role, reducing adhesion between the particles and substrate. No effects coming from the ordering of nanoparticles on large scales (well above the particle size) were observed. It was also showed that the during manipulation, moving particles dissipate lower energy as compared to a fixed particle.



# Chapter 5

## Controlled Manipulation of asymmetric nanoparticles by Atomic Force Microscopy

In this chapter, the manipulation of asymmetric nanoparticles by AFM is discussed. The particles with elongated shapes were used to investigate the rotational effects in the manipulation process. This study opens the path to understanding and controlling the motion of arbitrarily shaped nanoparticles. In the first part, motion of rigid nanorods caused by a nanotip rastered on a flat surface is described within an original collisional model. Provided that friction between nanorods and surface is sufficiently high, the direction of motion and the orientation of the nanorods are determined by two pairs of differential equations. In order to compare the numeric solutions of the model with experiments, gold nanorods were manipulated on a silicon oxide surface. In the second part of the chapter, the model was extended to study the motion of dendritic ‘nanoflowers’. Antimony islands on HOPG were used for the experimental study.

### 5.1 Manipulation of rigid gold nanorods

The mechanics of elongated objects like nanotubes, nanowires is attracting interest, for instance, due to their anisotropic friction properties [87]. When the lateral force exerted by the probing tip overcomes a certain threshold, these objects can be irreversibly deformed [88] or pushed away [89], depending on their hardness and adhesion to the substrate. In any case, the influence of rotational effects needs to be investigated. This was done on rigid nanorods and, results show that the main conclusion of our previous studies on nanospheres [Chapter 3], i.e. a one-to-one relation between the direction of motion and the density of scan lines, remains valid, although the analytic expressions become more

complex. The torque applied by the probing tip simply results in a wobbling motion of the rods, which does not change the average direction of the nanoparticles.

### 5.1.1 The Model

One can consider a rigid nanorod, formed by a cylinder with radius  $a$  and length  $L$  ended by two hemispherical caps with radius  $a$  (fig. 5.1). The rod axis is rotated by an angle  $\beta$  with respect to the fast scan direction  $x$  of the AFM. The nanorod can slide or roll (or both) on the plane  $xy$ , where the axis  $y$  is directed along the slow scan direction. Since the probing tip has a conical shape, it can transfer momentum to the nanorod both parallel to the  $xy$  plane or in the perpendicular direction  $z$ . We thus distinguish between the components  $F_{\parallel}$  and  $F_{\perp}$  of the average force applied by the tip, respectively parallel and perpendicular to the  $xy$  plane. Since the component  $F_{\perp}$  is balanced by the normal reaction of the substrate, this component can only be responsible for the rolling motion of the nanorod. The component  $F_{\parallel}$  causes both rolling and sliding. In the rest, we want to neglect the rolling motion, which, with few noticeable exceptions [90], is not detected by AFM, and we consequently limit our analysis to the plane defined by the directions  $x$  and  $y$  passing through the point of contact between nanorod and tip. The projections of the nanorod and tip centers on this plane are located at  $P \equiv (x, y)$ , and at  $O \equiv (x_0, y_0)$  respectively. A straight line traced from the point  $O$  perpendicularly to the rod axis crosses this axis in the point  $C \equiv (x_C, y_C)$  at a distance  $r$  from  $P$ . The distance between the points  $C$  and  $O$  will be denoted by  $R$ . This quantity is related to the tip radius  $R_t$  and the cylinder radius  $a$  by the same formulas introduced in Ref. [85] for a nanosphere. In particular, if  $a < (1 - \sin \gamma)R_t$ , where  $\gamma$  is the semi-aperture angle of the tip cone,  $R = 2\sqrt{R_t a}$ . If the AFM is operated in tapping-mode, the nanorod is repeatedly hit by the tip along each scan line. The collision time  $\Delta t$  is in the order of  $1/f_{\text{res}}$ , where  $f_{\text{res}} \sim 10^5$  Hz is the resonance frequency of the flexible cantilever holding the tip. The corresponding (average) force  $F_{\parallel}$  applied on the rod is oriented as in fig. 5.1. Due to the action of the force  $F_{\parallel}$ , the nanorod acquires a velocity  $\Delta v$  and an angular velocity  $\Delta \omega$ , according to the equations of motion of a rigid body:  $F_{\parallel} = M\Delta v/\Delta t$  and  $\rho F_{\parallel} = -MI\Delta \omega/\Delta t$ . Here,  $M$  is the mass of the nanorod,  $I$  is the moment of inertia of the rod with respect to the  $z$  axis passing through its center, and  $\rho$  is the distance between the point  $P$  and the line  $OC$ . In the collision time  $\Delta t$  the center of the rod  $P$  moves by a distance  $\Delta s = (F_{\parallel}/2M)(\Delta t)^2$  (not shown) in the direction of  $F_{\parallel}$ . In the same time, the nanorod rotates by an angle  $\Delta \beta = -(\rho F_{\parallel}/2I)(\Delta t)^2$  about the  $z$  direction. Dividing side by side we get a relation between the linear and the angular displacements of the nanorod:

$$\frac{\Delta \beta}{\Delta s} = -\frac{M}{I}\rho. \quad (5.1)$$

The moment of inertia of each hemispherical cap with respect to the point  $P$  is simply determined using Steiner's theorem:  $I_{\text{cap}} = m_{\text{cap}}(2a^2/5 + L^2/4)$ . Here,  $m_{\text{cap}} = (2/3)\pi a^3 \cdot \rho_m$  is the mass of each cap,  $\rho_m$  is the density mass of the rod, and we have used the formula

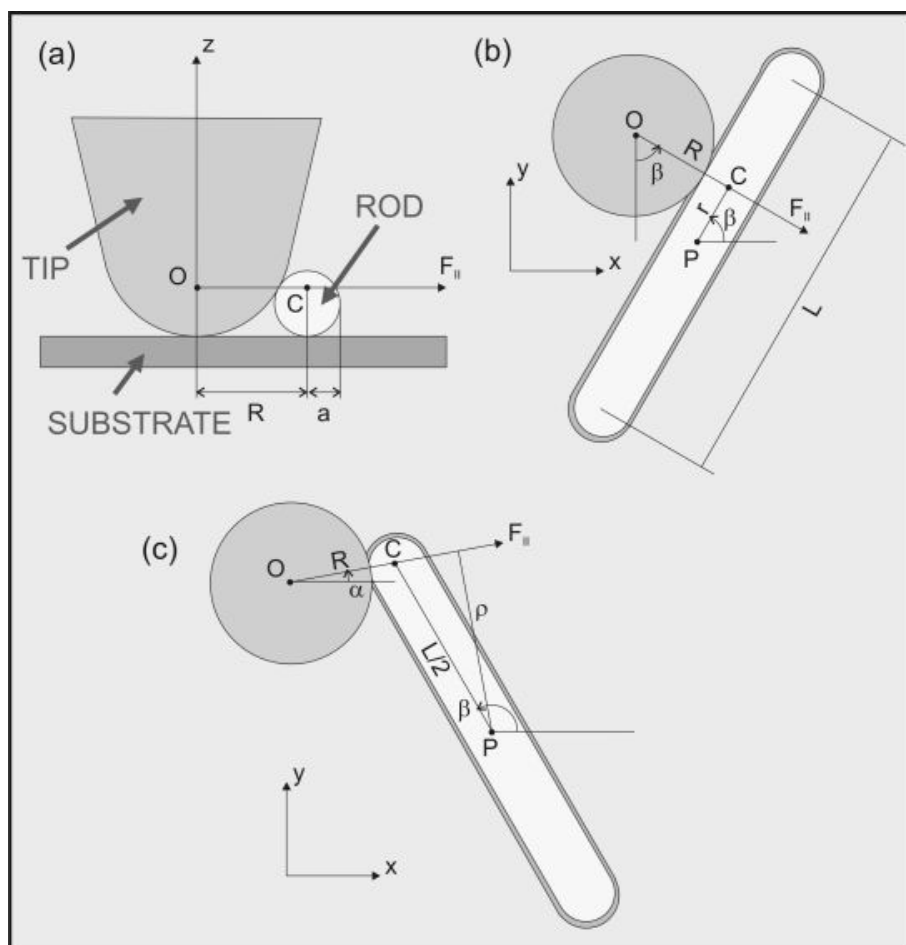


**Figure 5.1:** (a) Contact between a probing tip and a nanorod (side view). (b) The tip touches the cylindrical core of the rod (top view). (c) The tip touches the upper hemispherical cap of the rod (top view).



$I_{0,\text{cap}} = (2/5)m_{\text{cap}}a^2$  for the moment of inertia of a hemisphere with respect to the center of its base. The moment of inertia of the cylinder is  $I_{\text{cyl}} = m_{\text{cyl}}(L^2/12 + a^2/4)$ , where  $m_{\text{cyl}} = \pi a^2 L \cdot \rho_m$  is the cylinder mass. Since  $M = m_{\text{cyl}} + 2m_{\text{cap}}$  and  $I = I_{\text{cyl}} + 2I_{\text{cap}}$ , the ratio  $I/M$  appearing in Eq. (5.1) is thus given by

$$\frac{I}{M} = \frac{L \left( \frac{L^2}{12} + \frac{a^2}{4} \right) + \frac{4a}{3} \left( \frac{2a^2}{5} + \frac{L^2}{4} \right)}{L + \frac{4a}{3}}. \quad (5.2)$$

If  $r < L/2$  the tip collides with the cylindrical part of the nanorod. From fig. 5.1(b) it can be seen that  $y_0 - y_C = R \cos \beta$  and  $y_C - y = r \sin \beta$ , so that  $r = (y_0 - y - R \cos \beta) / \sin \beta$ . The displacement of the rod center  $P$  is given by  $\Delta y = -\Delta s \cos \beta = -\Delta x / \tan \beta$ . Substituting in (5.1), with  $\rho = r$ , and letting  $\Delta t$  tend to zero, we get the two differential equations:

$$\frac{d\beta}{dy} = \frac{2M(y_0 - y - R \cos \beta)}{I \sin 2\beta} \quad (5.3)$$

and

$$\frac{dy}{dx} = -\cot \beta. \quad (5.4)$$

When  $r > L/2$ , the tip does not collide with the cylindrical part of the rod, but it can still touch one of the two hemispherical caps. The situation in fig. 5.1(c) corresponds to the tip in contact with the upper cap of the rod. It is not difficult to see that  $y_C - y_0 = R \sin \alpha$  and  $y_C - y = (L/2) \sin \beta$ . Thus,  $\sin \alpha = [y - y_0 + (L/2) \sin \beta] / R$ . The distance  $\rho$  between the point  $P$  and the line  $OC$  is given by  $\rho = (L/2) \sin(\beta - \alpha)$ . In the collision time  $\Delta t$ , the point  $P$  is displaced by  $\Delta y = \Delta s \sin \alpha = \Delta x \tan \alpha$  and, when  $\Delta t \rightarrow 0$ , we get:

$$\frac{d\beta}{dy} = \frac{\rho M \sin(\beta - \alpha)}{2I \sin \alpha}, \quad (5.5)$$

$$\frac{dy}{dx} = \tan \alpha. \quad (5.6)$$

Thus, the two pairs of equations (5.3), (5.4) and (5.5), (5.6) describe the motion of the nanorod in the  $xy$  plane when the rod is pushed on its straight side or, respectively, on one of its two ends.

We have solved the equations (3-6) numerically assuming that the probing tip follows a raster scan path, i.e. it is scanned back and forth along the  $x$  axis (while oscillating in the  $z$  direction), then suddenly moved of a quantity  $b$  along the  $y$  axis and the scan is repeated. We used the values  $R_t = 10$  nm,  $a = 8$  nm,  $L = 100$  nm and  $b = 20$  nm,

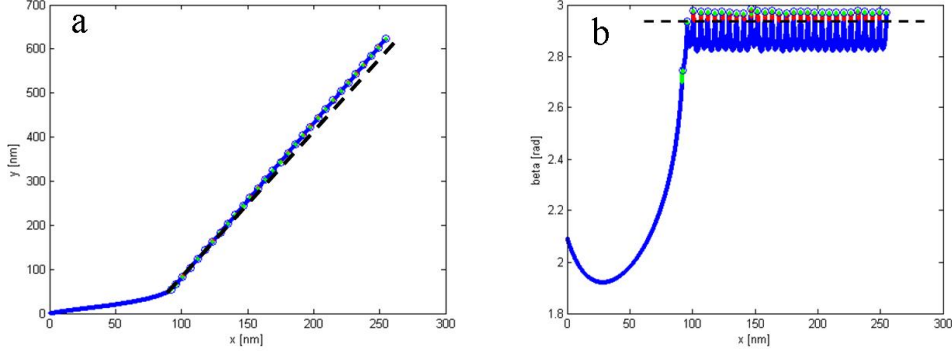


**Figure 5.2:** Simulated motion of a nanorod pushed by an AFM tip in tapping mode. (a)  $y$ -coordinate of the rod center and (b) angle of orientation  $\beta$  of the nanorod. The blue lines correspond to the tip colliding with a straight side of the rod. The red and green lines correspond to collisions with the upper and lower caps respectively. The circles indicate the end of each scan line. The parameter values are  $R_t = 10$  nm,  $a = 8$  nm,  $L = 100$  nm and  $b = 20$  nm. The straight lines correspond to the values expected in the nanowire approximation ( $a \rightarrow 0$ ).

with the nanorod initially displaced by  $y = -5$  nm from the first scan line and tilted by an angle  $\beta = 2\pi/3$ . The  $y$  coordinate of the rod center  $P$ , and the angle  $\beta$  defining the rod orientation, are plotted in fig. 5.2 as functions of the  $x$  coordinate of  $P$ . As a result, the direction of motion of the nanorod becomes well-defined after the first two scan lines, and it is given by an angle  $\theta \simeq 72^\circ$ . At the same time, the rod wobbles around the angle  $\bar{\beta} \simeq 164^\circ$ . A similar trend is observed in a large range of values of  $R$ ,  $L$  and  $b$ , with different initial positions of the nanorods (provided that the nanorod doesn't move downwards at the end of the scan line).

The previous conclusions can be made quantitative in the limit case  $a \rightarrow 0$ , when the motion is described by Eqs. (5.3) and (5.4) only. If we consider the average values of the parameters  $x$ ,  $y$  and  $\beta$ , Eq. (5.4) implies that

$$\tan \theta \equiv \frac{d\bar{y}}{d\bar{x}} = -\cot \bar{\beta}, \quad (5.7)$$

i.e.  $\theta = \bar{\beta} - 90^\circ$ . This means that the average orientation of the rod is perpendicular to its direction of motion. Eq. (5.3), with  $\bar{\beta} = \text{const.}$ , gives  $y_0 - \bar{y} = R \cos \bar{\beta}$ . Observing that the rod center  $P$  is located at  $y = y_0 - b + R + (L/2) \sin \bar{\beta}$  at the beginning of each scan line, and it is shifted upwards by the distance  $b$  at the end, we get  $\bar{y} = y_0 - b/2 + R + (L/2) \sin \bar{\beta}$  so that

$$R \cos \bar{\beta} + \frac{L}{2} \sin \bar{\beta} = \frac{b}{2} - R. \quad (5.8)$$

With the values used to produce fig. 5.2, Eqs. (5.7) and (5.8) give  $\bar{\beta} = 169^\circ$  and  $\theta = 79^\circ$ ,

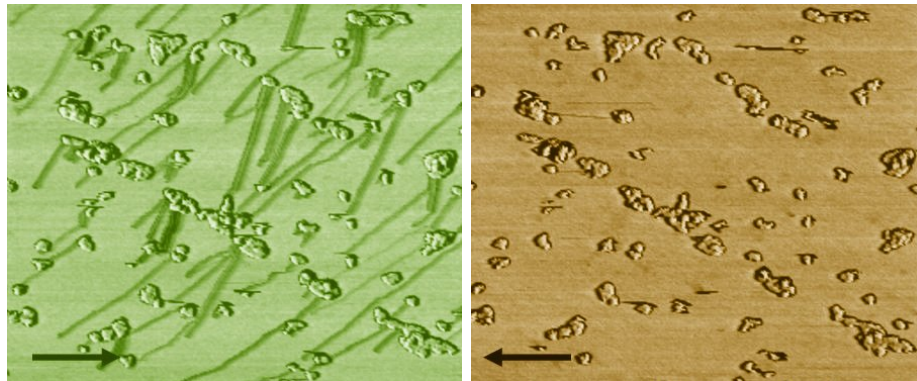


**Figure 5.3:** (a) Forward and (b) backward phase image of gold nanorods manipulated on a silicon oxide surface in ambient conditions. The black arrow shows an anomalous trace, possibly due to an aggregate of two nanorods moving together. The spacing between consecutive scan lines is  $b = 15.6$  nm and the images are  $4.2 \times 1.6 \mu\text{m}^2$  in size.

which is roughly in agreement with the numerical results (for a thick wire). On the other side, when  $L \rightarrow 0$  the rod reduces to a nanosphere. This case was studied in Chapter 3 (ref. eq. (3.8)).

### 5.1.2 Experimental Results

We have tested our model on gold nanorods manipulated by tapping-mode AFM (Nanite™, Nanosurf AG, Switzerland) on silicon oxide. Their nominal length and diameter were 29 nm and 10 nm, corresponding to the parameter values  $a = 5$  nm and  $L = 19$  nm in the model. The solution was deposited on a silicon wafer, which was previously cleaned with ethanol and acetone. The substrate temperature was kept at 160 °C during deposition, then washed with distilled water and blown with nitrogen. This procedure resulted in a well-separated and easily mobile distribution of nanorods. Fig. 5.3 shows two forward and backward scan images of the nanorods manipulated in tapping mode under ambient conditions (RH  $\simeq$  40%). We have plotted the phase shift of the cantilever oscillations, since this signal gave a better contrast compared to the topography. The traces corresponding to the moving nanoparticles are only visible in the forward image. Furthermore, no discontinuities are observed in the rod trajectories, which means that the friction force between particles and substrate is quite high [86]. The hypotheses of our model are thus verified. The average angle of motion  $\theta$  of the nanorods can be estimated by taking the self-correlation of fig. 5.3(a) [85]. In such a way, spurious traces due to multiple collisions between nanorods and agglomerates of particles occasionally moving as a whole can be excluded. Incidentally, we note that the particles tend to be trapped along a straight line, corresponding to a step edge of the substrate, which has been also reported in similar studies on gold nanospheres manipulated on graphite [91]. Fig. 5.4 shows the average angle  $\theta$  so determined as a function of the parameter  $b$ . The values were obtained from

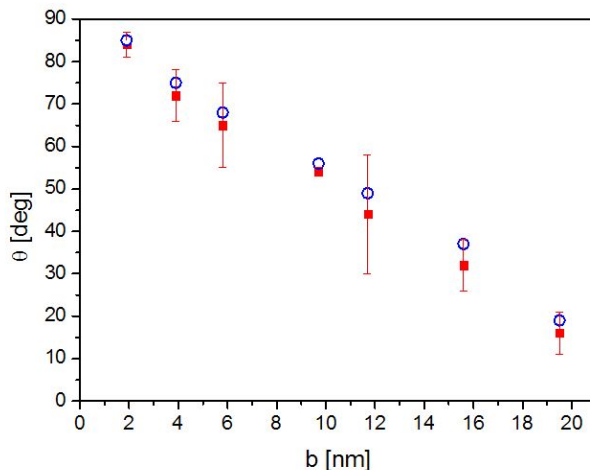


**Figure 5.4:** Average angle of motion of the nanorods as a function of the spacing  $b$ . The red squares correspond to the experimental results. The blue circles are obtained from the model with the fit parameters  $R_t = 10$  nm,  $a = 5$  nm and  $L = 19$  nm.

a series of images acquired on different areas in the same region of the sample. Since the rods are quite thick, we have reproduced their behavior using the complete model (i.e. not with the nanowire approximation). The experimental results are well fitted using the nominal value  $R_t = 10$  nm for the tip radius, which is also shown in fig. 5.4.

## 5.2 Manipulation of asymmetric “Nanoflowers”

After examining the case of rigid nanorods, we were interested to know if we could extend and generalize the model to study the motion of other (asymmetric) shapes of particles. Due to the Nanoparma project we got a chance to collaborate with the group of Dr André Schirmeisen, Centech, Germany. His group had reported the use of highly ramified antimony islands on HOPG. Since these islands were relatively flat, asymmetric and easily mobile, they were perfect candidates for studying the rotational effects during manipulation. The aim was to try to ‘tune’ the motion of these particles by adjusting the spacing. The author spent few days in the lab of Dr André to perform some manipulation experiments using the Nanonis, UHV system.

## 5.3 The Model

Deducing a model for irregular shaped particles was initially a challenge. But, thanks to Dr. Enrico Gnecco the problem was solved. He was successful in deriving the model,

described below :

Equations of motion(during a short time interval  $\Delta t$ ), corresponding to the tip particle collision is given by,

$$\begin{aligned}\vec{F} &= M \frac{d^2 \vec{R}}{dt^2} \\ \vec{r} \times \vec{F} &= I \frac{d^2 \vec{\theta}}{dt^2}\end{aligned}\tag{5.9}$$

Assuming a constant force  $\vec{F}$ , it can be seen that

$$\frac{\Delta\theta}{\Delta s} = \frac{Mr \sin \alpha}{I}\tag{5.10}$$

A ‘manipulation protocol’ was defined and applied to the asymmetric particle. Thus, the routine is

- (1) Fix the initial position of the particle (i.e.  $\vec{R}$  and  $\vec{\theta}$  and fix  $b$ )
- (2) Find  $r$  and  $\alpha$
- (3) Calculate  $\Delta y$  and  $\Delta\theta$  corresponding to a small displacement along the fast scan direction
- (4) Translate the particle by (  $\Delta x$ ,  $\Delta y$  ) and rotate it by  $\Delta\theta$
- (5) Repeat (2-4) until the particle has not crossed by the scan line
- (6) Translate the tip along a quantity  $b$  along the slow scan directional
- (7) Repeat (2-6)

To use the protocol on antimony nanoparticles, a single antimony island was chosen and its profile was digitalized (using Matlab with Image Processing Toolbox) and converted into polar coordinates.

Using the above mentioned protocol and the profile of the particle, the trajectory in  $XY$  plane and the orientation of the antimony particle as a function of  $X$ -axis is plotted (see fig. 5.7). It can be seen from the figure that the motion of the particle tends to become regular, independently of the shape. In order to verify the results from the model antimony islands were manipulated on HOPG.

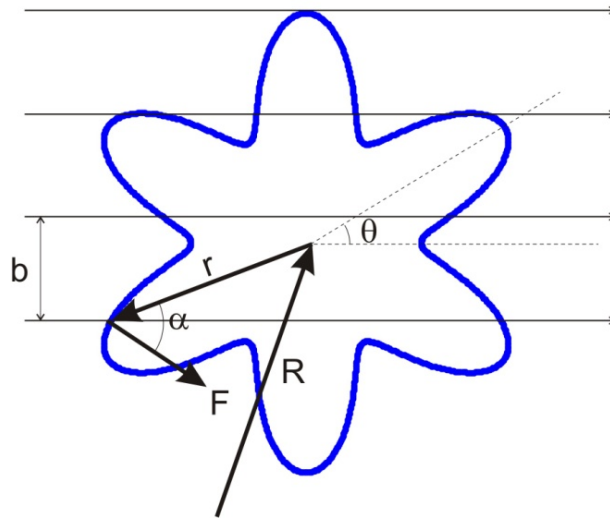
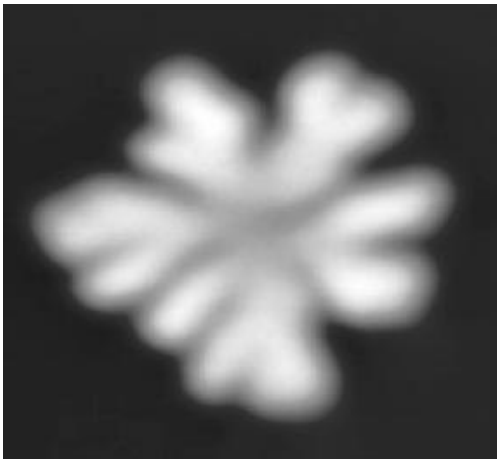
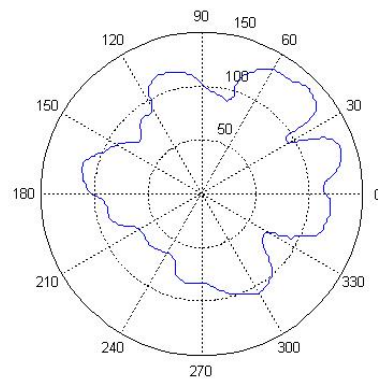


**Figure 5.5:** An asymmetric nanoparticle in the  $XY$  scan path of the tip.



(a)



(b)

**Figure 5.6:** (a) Shows a single antimony island and (b) Profile of the nanoparticle created by matlab and converted into polar coordinates,  $r = r(\theta)$

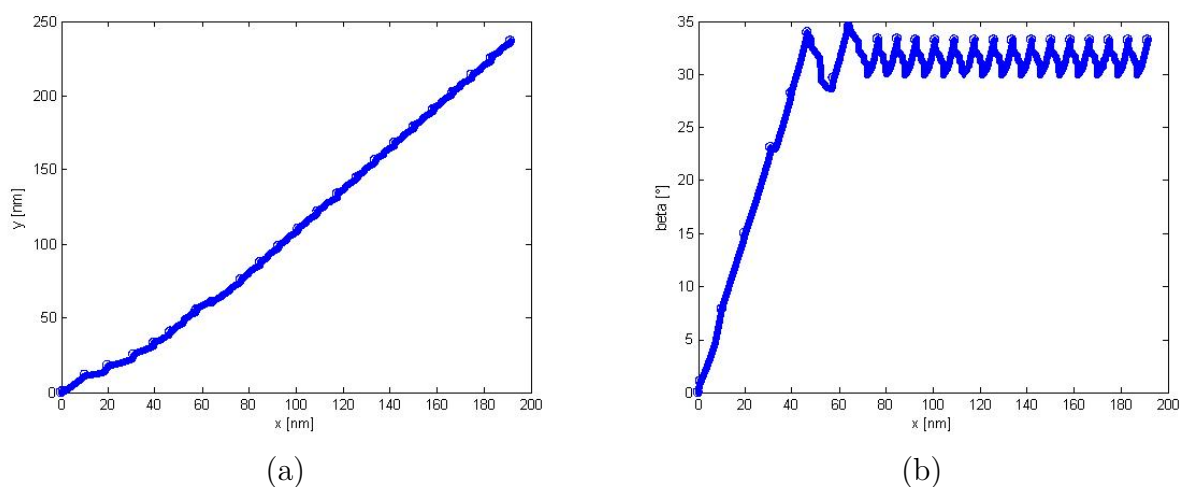


**Figure 5.7:** Trajectory of the antimony particle in XY plane (b) Orientation of the particle (beta) with respect to the X-axis.

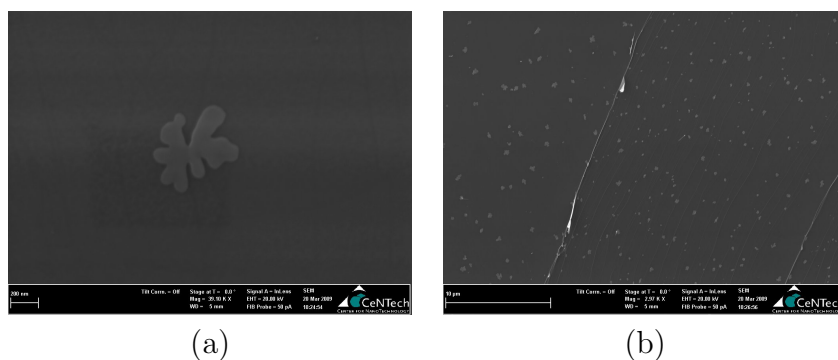


**Figure 5.8:** SEM images of antimony islands on HOPG

### 5.3.1 Sample Preparation

The sample preparation was done by Dr Dirk Dietzel. HOPG samples were cleaved in vacuum and heated in-situ to 350°C for 1hour in order to ensure clean surface conditions. Antimony was evaporated from the solid phase at 370°C for 3 minutes. Nanometer-sized particles would then spontaneously be formed by diffusion and aggregation of the deposited material on the surfaces. This procedure resulted in highly ramified islands of 100-350 nm in diameter and up to 80nm in height. SEM images of the sample fig. 5.8 were taken to get an overview of the area and to verify the size and distribution of the particles.

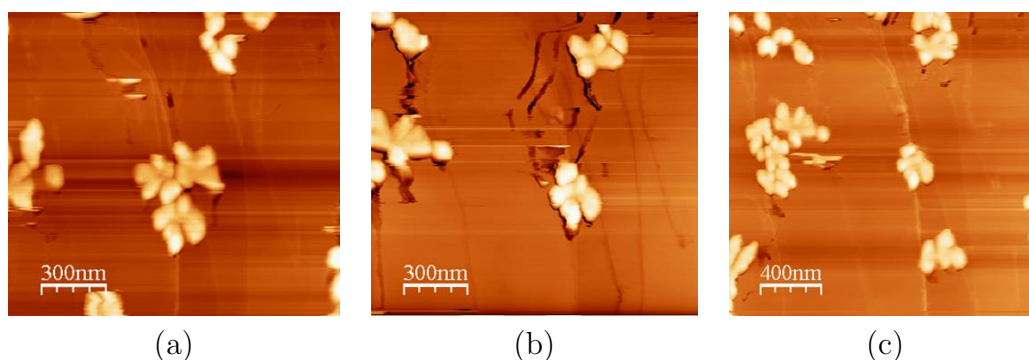


**Figure 5.9:** AFM images of antimony islands on HOPG. (a) before manipulation (b) during manipulation (c) after manipulation.

### 5.3.2 Experimental Results

The initial idea was to image the nanoparticles in tapping mode, but the islands were quite large which lead the tip to crash several times into the surface. This made it very difficult to image in tapping mode and so the measurement had to be done in contact mode. The measurement was first done with a low load fig. 5.9(a) so as to locate the position of the particle and then increased in the second scan such that the particle starts to move fig. 5.9(b). The final scan was done again with a low load so as to locate the final position of the particle fig. 5.9(c). It can be seen from fig. 5.9 that the particle translates as well as rotates during manipulation. More systematic measurements by varying the spacing between the scan lines have to be done. Work related to this is under progress.

In conclusion, a model describing the manipulation of rigid nanorods in tapping-mode AFM was introduced and extended to particles of other shapes. A set of two differential equations was derived, which can be used to reproduce the trajectories and the oscillations of the nanorods. The equations can be exactly solved in the limit case of nanospheres and thin nanowires. In the last case, we predict that the direction of motion of the nanorods and their average orientation are given by the equations (5.7) and (5.8). The results of the model are well supported by a series of measurements on gold nanorods in ambient conditions. It was also shown that the direction of the other asymmetric shaped particles can also be predicted using the model. Some more planned measurements are required for the experimental verification .





# Chapter 6

## Conclusions and Outlook

In this thesis, several aspects of characterization and manipulation of nanoparticles by tapping mode AFM were studied. The role of an AFM as a characterizing and manipulation tool was demonstrated.

The study of nanoparticles by AFM required them to be well dispersed on a substrate and this was the main issue addressed in chapter 1. It was shown that the density of particles on the substrates were influenced by the nature of the nanoparticle and the substrate. An ideal way to have a reduced density of particles is by increasing the hydrophobicity of the surface. It was also seen that the nanoparticles that had a chemically modified surface (capping agent) were easier to deposit and image as they formed lesser agglomerates as compared to bare nanoparticles. In order to gain representative information on the form, size and/or size distribution of the nanoparticles and agglomerates on the surface, an appropriate tip characterizing sample was used to determine the true size of the nanoparticles independently of the tip. Tip functionalization was done to determine the adhesion of the nanoparticles. The studies revealed that the adhesion of the nanoparticles to the substrate decreases with the increase in the hydrophobicity of the surface and vice versa. Some more planned measurements are required to measure the adhesion forces between nanoparticle-nanoparticles and nanoparticle-substrate as we had difficulties in gluing a single nanoparticle to the tip and also in some cases to determine whether there was an agglomerate of nanoparticle attached to the tip or it was just plain glue. KPFM imaging of a mixture of nanoparticles is an idea for future experiments as it would be interesting to see the difference in the contact potentials depending on the size of the particles. Also, the electric contact properties of nanoparticles on substrates and/or between nanoparticles/agglomerates can be determined.

In Chapter 3, the controlled manipulation of Au nanoparticles was discussed. Instead of a single nanoparticle, ensembles of nanoparticles were used for manipulation. An original

model was proposed which relates the trajectory of the moving particle with the density of the scan lines. The motion of the nanoparticle can be ‘tuned’ by adjusting the pathway of the probing tip and the radius of the particle and tip. The radius of the particle can also be estimated if the radius of the tip is known or vice versa. Assuming that friction between the particle and the substrate is high enough, the direction of motion of the nanospheres was related to the density of the scan lines by an analytical formula. It was showed how lowering friction between the particles and substrate results in enhanced fluctuations of the particle trajectories, without significant changes in the average direction of motion.

In chapter 4, different factors which effect the mobility of the nanoparticles during manipulation by AFM were studied. This was done by manipulation of gold nanoparticles by varying the surface chemistry, environment, and temperature. Energy dissipation during manipulation was calculated. Systematic measurements revealed that in ambient conditions, the mobility of the particles is greatly enhanced by hydrophobic interlayers, formed by organic coatings deposited on the particles. In the absence of humidity, the gold particles strongly adhered to the silicon substrate, and manipulation could not be achieved. Thermal activation plays an opposite role by reducing adhesion between the particles and substrate. The ordering of nanoparticles on large scales (well above the particle size) played no role on the mobility of particles.

In chapter 5, the model introduced in the earlier part of the thesis was extended for the study of motion of asymmetric nanoparticles. The model introduced in Chapter 3 was extended to predict the motion of the nanorods as well as arbitrary flower shaped particle. It was showed that the asymmetric particles follow a defined path although they wobble around a fixed angle. Experimental verification was done by manipulating Au nanorods on Si and Sb islands on HOPG. It was also shown that the values of the deflection angle from the experiment and model matched well.

A future goal would be to reduce friction between particles and substrate by excluding the mechanical resonances of the sliding system (tip) perpendicular to the contact plane, thus switching on and off friction between tip and particles. This would help in reducing the wear of the tip which would increase the lifetime of the probing tip. It would also be interesting because then exchange from manipulation to imaging modes would be possible by alternating between dynamic superlubricity and normal friction regimes [93]. Another idea would be to image and manipulate nanoparticles in liquid, as this will address important questions related to microfluidics, etc. Controlling the trajectory of a nanoparticle sliding on a solid surface is extremely important in applications ranging from drug delivery to environmental control. In both cases it would be highly desirable to develop methods for characterizing mobility of tiny objects (aggressive particulates or beneficial nanocapsules).

# Bibliography

# Bibliography

- [1] G.Binnig and H.Rohrer, *Helv.Phys.Acta* 55, 726-735 (1982)
- [2] G. Binnig, H.Rohrer, Ch. Gerber, and E.Weibel, *Phys.Rev.Lett.*50(2), 120-123 (1983)
- [3] G.Binnig, C.F. Quate, and Ch. Gerber: , *Phys.Rev.Lett.*56 (9), 930-933 (1986)
- [4] R. Bennewitz, M.Reichling, and E.Matthias, *Surface Science* 387, 69 (1997)
- [5] M. Saint Jean, S. Hudlet, C. Guthmann, and J Berger, *J.Appl.Phys.* 86 (9), 5245 (1999)
- [6] F.J. Giessibl. *Phys.Rev. B*, 45(23), 13815-13818, (1992)
- [7] A.W Adamson: *Physical chemistry of surfaces*(John Wiley Sons, (1976)
- [8] E.Riedo, F. Levy, and H. Brune, *Phys. Rev Lett.* 88, 185505 (2002)
- [9] HallMark VM, Chiang S., Rabolt JF, Swalen JD, Wilson RJ, *Phys Rev Lett*, 59(25), 2879-2882, (1987).
- [10] F.J. Giessibl, Ch. Gerber, G. Binnig, *J Vac Sci. Tech, B* 9, 984 (1991)
- [11] Y. Martin, C.C. Williams, H.K. Wickramasinghe. *J. Appl. Phys.* 61, 4723(1987)
- [12] Q. Zhong, D. Innis, K. Kjoller, V.B. Elings. *Surf. Sci. Lett.* 290, L688 (1993)
- [13] T.R. Albreth, P. Grutter, D.Horne, D.Rugar. *J. Appl. Phys.* 69,668 (1991)
- [14] F.J. Giessibl. *Jpn. J. Appl. Phys.*33,3726 (1994)
- [15] F.J. Giessibl, B.M. Trafas. *Rev.Sci.Instrum.*65, 1923 (1994)
- [16] F.J. Giessibl. *Science* 267, 68 (1995)
- [17] I.Yu. Sokolov, G.S. Henderson, F.J Wicks. *Appl. Surf. Sci.* 140, 362 (1999)
- [18] R.Garcia and Ruben Perez: *Surface Science Reports* 47, 197 (2002)

- 
- [19] Q. Zhong, D. Inniss, K. Kjoller, and V.B. Elings. *Surface Science* 290, L688 (1993)
- [20] O.P. Beherend, L. Odoni, J.L.Loubet, and N.A Burnham. *Appl. Phys. Lett.* 75, 2551 (1999)
- [21] R. Garcia and A.San Paulo. *Phys.Rev. B* 60, 4961 (1999)
- [22] J.Tamayo and R. Garcia, *Appl.Phys.Lett.* 71,2394 (1997)
- [23] Dirk Dietzel, Tristan Mönninghoff and Lars Jansen, Claudia Ritter and Udo D. Schwarz, *J Appl Phys*, 102, 084306 (2007).
- [24] Dirk Dietzel, Michael Feldmann, Harald Fuchs, Udo D. Schwarz and André Schirmeisen, *Appl Phys Lett*, 053104 (2009)
- [25] M. Nonnenmacher, M. P. O'Boyle, and H. K. Wickramasinghe . *Appl. Phys. Lett.* 58: 2921 (1991)
- [26] J. Turkevich, P. C. Stevenson, and J. Hillier. *Discussions of the Faraday Society*, 11:55-75, (1951)
- [27] G. Schmid. Metal nanoparticles, synthesis of. In *Encyclopedia of inorganic chemistry*. John Wiley & Sons, Ltd., (2006)
- [28] M. C. Daniel and D. Astruc. *Chemical Reviews*, 104:293-346, (2004)
- [29] M. Wirtz, C.R.M., *Advanced Materials*, 15(5): p. 455-458. (2003)
- [30] Yu, Y.Y., et al., *J. Phys. Chem. B*, 101(34): p. 6661-6664. (1997)
- [31] Kim, F., J.H. Song, and P. Yang, *J. Am. Chem. Soc.*, 124(48): p. 14316-14317. (2002)
- [32] Nikhil R. Jana, L.G., and Catherine J. Murphy, *J. Phys. Chem.*, 105: p. 4065-4067. (2001)
- [33] El-Sayed et al.,*Chem. Mater*, 15: p. 1957 -1962. (2003)
- [34] Kyumin Lee, M. Duchamp, G. Kulik, A. Magrez, J. W. Seo, S. Jeney, A. J. Kulik, L. Forro, R. S. Sundaram, and J. Brugger. , *Applied Physics Letters*, 91:173112, (2007)
- [35] J. Melngailis, *Focused ion beam technology and applications*, *J. Vac. Sci.Technol. B* 5 469-495 (1987)
- [36] J. Gierak, E. Bourhis, M.N.Merat Combes, Y. Chriqui, I. Sagnes, D. Mailly, P. Hawkes, R. Jede, L. Bruchhaus, L. Bardotti, B. Prevel, A. Hannour, P.Melinon, A. Perez, J. Ferre, J.-P. Jamet, A. Mougin, C. Chappert, V. Mathet, *Microelectron. Eng.* 78-79, 266-278. (2005)

- [37] P. Hoffmann, G. Kulik, and L Barbieri, Swiss Patent Applications #DE10248775-A1 (18 October 2002); WO2004037446-A1 ( 2003).
- [38] Y L LYyubchenko, P I Oden, D Lampner, S M Lindsay and K A Dunker , *Nucleic Acids Research* 21 [5] 1117-1123 (1993)
- [39] J. A. Stroschio and D. M. Eigler, *Science*, vol. 254, pp. 1319-1326, (1991)
- [40] H. C. Manoharan, C. P. Lutz, and D. M. Eigler, *Nature*, vol. 403, pp. 512-515, (2000)
- [41] M. F. Crommie, C. P. Lutz, and D. M. Eigler, *Nature*, vol. 363, pp. 524-527, (1993)
- [42] I.W. Lyo and P.Avouris, *Science*, vol. 253, pp.173-176, (1991)
- [43] T. A. Jung, R. R. Schlitter, J. K. Gimzewski, H. Tang, and C. Joachim, *Science*, vol. 271, pp. 181-184, (1995)
- [44] S. Maruno, K. Inanaga, and T. Isu, *Appl. Phys. Lett.*, vol. 63, pp. 1339-1341, (1993)
- [45] P. H. Beton, A. W. Dunn, and P. Moriarty, *Appl. Phys. Lett.*, vol. 67, pp. 1075-1077, (1995)
- [46] Cuberes, M. T.; Schlitter, R. R.; Gimzewski, J. K. *Appl. Phys. Lett.* 69, 3016. (1996)
- [47] T. Junno, K. Deppert, L. Montelius, and L. Samuelson, *Appl.Phys. Lett.*, vol. 66, pp. 3627-3629, (1995)
- [48] D. M. Schaefer, R. Reifenberger, A. Patil, and R. P. andres, *Appl. Phys. Lett.*, vol. 66, pp. 1012-1014, (1995)
- [49] A. A. G. Requicha, C. Baur, A. Bugacov, B. C. Gazen, B. Koel, A. Madhukar, T. R. Ramachandran, R. Resch, and P. Will, in *Proc. IEEE Int. Conf.Robotics and Automation*, Leuven, Belgium, pp. 3368-3374 (1998)
- [50] C Baur, A Bugacov, B E Koel, A Madhukar, N Montoya, T R Ramachandran, A A G Requicha, R Resch and P Will, *Nanotechnology*,vol 9,360-364. (1998)
- [51] L. T. Hansen, A. Khle, A. H. Sorensen, J. Bohr, and P. E. Lindelof, *Nanotechnology.*, vol. 9, pp. 337-342, (1998)
- [52] M. Sitti and H. Hashimoto, in *Proc. IEEE/RSJ Int. Conf. Intelligent Robots and Systems*,Victoria, BC, Canada, pp. 1739-1746 (1998)
- [53] Lüthi, R.; Meyer, E.; Haefke, H.; Howald, L.; Gutmannsbauer, W.;Güntherodt, H.-J. *Science* 1994, 266, (1979)
- [54] TR Ramachandran, C Baur, A Bugacov, A Madhukar, A Requicha, *Nanotechnology*, 9, 237-245 (1998)

- 
- [55] R Resch, A Bugacov, C Baur, B E Koel, A Madhukar, A Requicha and P Will, *Appl Phys A*, 67, 265-271, (1998)
- [56] Ritter, C.; Heyde, M.; Stegemann, B.; Rademann, K.; Schwarz, U. *D.Phys. ReV. B*, 71, 085405 (2005)
- [57] Landau L D and Lifshitz E M, *Course of Theoretical Physics: Mechanics* (Oxford: Butterworth-Heinemann) (1976)
- [58] Meyer E, Hug H J and Bennewitz R, *Scanning Probe Microscopy: The Lab on the Tip* (Berlin: Springer) (2003)
- [59] Mougín K, Gnecco E, Rao A, Cuberes M T, Jayaraman S, McFarland E W, Haidara H and Meyer E 2008 *Langmuir* 24 1577 (2008)
- [60] Melngailis J J. *Vac. Sci. Technol. B* 5 469 (1987)
- [61] Marchetto D, Rota A, Calabri L, Gazzadi G C, Menozzi C and Valeri S, *Wear* 265 577 (2008)
- [62] E. Gnecco, R. Bennewitz, T. Gyalog, Ch. Loppacher, M. Bammerlin, E. Meyer, and H.-J. Güntherodt, *Phys. Rev. Lett.* 84, 1172 (2000).
- [63] C. Ritter, M. Heyde, U.D. Schwarz, and K. Rademann, *Langmuir* 18, 7798 (2002)
- [64] N. Martsinovich, C. Hobbs, L. Kantorovich, R.H.J. Fawcett, M.J. Humphry, D.L. Keeling, and P.H. Beton, *Phys. Rev. B* 74, 085304 (2006).
- [65] M. Evstigneev, priv. Comm. (2009).
- [66] M.H. Korayem and M. Zakeri, *Int. J. Adv. Manuf. Techn.*, 41, 714 (2009).
- [67] M. Göttinger and W. Peukert, *Langmuir* 20, 5298 (2004).
- [68] M. Palacio and B. Bhushan, *Nanotechnology* 19, 315710 (2008).
- [69] Yee, C. K.; Ulman, A.; Ruiz, J. D.; Parikh, A.; White, H.; Rafailovich, M. *Langmuir*, 19, 9450. (2003)
- [70] Jaramillo, T. F.; Baeck, S.-H.; Cuenya, B. R.; McFarland, E. W. *J. Am. Chem. Soc.*, 125, 7148. (2003)
- [71] Cuenya, B. R.; Baeck, S.-H.; Jaramillo, T. F.; McFarland, E. W. *J. Am. Chem. Soc.* 125, 12928. (2003)
- [72] Howald, L.; Meyer, E.; Lüthi, R.; Haefke, H.; Overney, R.; Rudin, H.; Güntherodt, H.-J. *Appl. Phys. Lett.* 63, 117. (1993)



- [73] Grabar, K. C.; Allison, K. J.; Baker, B. E.; Bright, R. M.; Brown, K. R.; Freeman, R. G.; Fox, A. P.; Keating, C. D.; Musick, M. D.; Natan, M. J. *Langmuir*, **12**, 2353.
- [74] Kunz, M.; Shull, K. R.; Kellock, A. J. *J. Colloid Interface Sci.* **1993**, *156*, 240 (1996)
- [75] Liu, J.; Zhang, L.; Mao, P.; Chen, D.; Gu, N.; Ren, J.; Wu, Y.; Lu, Z. *J. Chem. Soc. Jpn.*, 1147 (1997)
- [76] Riedo, E.; Levy, F.; Brune, H. *Phys. Rev. Lett.*, **88**, 185505. (2002)
- [77] Mougín, K.; Castelein, G.; Haidara, H. *Tribol. Lett.*, **17**, 11. (2004)
- [78] Yoshizawa, H.; Chen, Y.-L.; Israelachvili, J. *J. Phys. Chem.*, **97**, 4128. (1993)
- [79] Israelachvili, J. *Intermolecular & Surface Forces*; Academic Press: San Diego, CA, (1992)
- [80] Meredith, J. C.; Smith, A. P.; Karim, A.; Amis, E. J. *Macromolecules*, **33**, 9747 (2000)
- [81] V.L. Colvin, *Nat. Biotechnol.* **21**, 1166 (2003).
- [82] C. Sealy, *Nano Today* **4**, 286 (2009).
- [83] H.K. Patra, S. Banerjee, U. Chaudhuri, P. Lahiri, A.K. Dasgupta, *Nanomed.* **3**, 111 (2007).
- [84] D. Dietzel, C. Ritter, T. Mönninghoff, H. Fuchs, A. Schirmeisen, and U.D. Schwarz, *Phys. Rev. Lett.* **101**, 125505 (2008).
- [85] A. Rao, E. Gnecco, D. Marchetto, K. Mougín, M. Schönenberger, S. Valeri, and E. Meyer, *Nanotechnology* **20**, 115706 (2009).
- [86] A. Rao, M.L. Wille, E. Gnecco, K. Mougín, and E. Meyer, *Phys. Rev. B*, **80**, 193405 (2009)
- [87] M. Lucas, X. Zhang, I. Palaci, C. Klinke, E. Tosatti, and E. Riedo, *Nat. Mat.*, accepted (2009).
- [88] G. Conache, S.M. Gray, A. Ribayrol, L.E. Froberg, L. Samuelson, H. Pettersson, and L. Montelius, *Small* **5**, 203 (2009).
- [89] E. Tranvouez, A. Orieux, E. Boer-Duchemin, C.H. Devillers, V. Huc, G. Comtet, and G. Dujardin, *Nanotech.* **20**, 165304 (2009).
- [90] M.R. Falvo, R.M. Taylor II, A. Helsen, V. Chi, F.P. Brooks Jr, S. Washburn, and R. Superfine, *Nature* **397**, 236 (1999).

- [91] G. Paolicelli, M. Rovatti, A. Vanossi, and S. Valeri, *Appl. Phys. Lett.* **95**, 143121 (2009).
- [92] E. Meyer, R. Lüthi, L. Howald, M. Bammerlin, M. Guggisberg, and H.-J. Güntherodt, *JVST B*, 14, 1285. (1996)
- [93] A Socoliuc, E Gnecco, S Maier, O Pfeiffer, A Baratoff, R Bennewitz, E Meyer, *Science*, 313, 14, (2006).

# Acknowledgment

*The world is round and the place which may seem like the end may also be the beginning*  
- Ivy Baker Priest

These words articulate at best, how I feel at the end of my PhD. This journey has been a very enriching experience and for this I ought to thank a number of people who made this possible.

First of all, I would like to thank Prof. Ernst Meyer who gave me an opportunity to work in his lab and introducing me to the fascinating world of microscopy. I am grateful for his help and for providing the possibility of working within an easy environment.

I am indebted to my co-advisor Dr. Enrico Gnecco for his optimism, enormous patience, very caring nature, vast knowledge and trust in me. 'Thanks' would indeed be a small word to express my gratitude. His guidance and motivation at every stage of my thesis made this journey very smooth.

I would like to thank Dr Monica Schönenberger for always being supportive and helpful during the time together.

I am also thankful to Dr Thilo Glatzel, who was always ready to help and troubleshoot.

I would like to thank all the former and present members of the group.

I am grateful to the secretaries for helping me with administrative things and for assisting me in many other different ways. G. Weaver, B. Kammermann and A. Kalt.

I also thank Dr Karine Mougin for her help at every point of the thesis , right from providing samples or helping out with the visa formalities.

I would like to thank Dr André Schirmeisen for agreeing to be the co-referee of this thesis and also for letting me work in his lab, it was indeed an interesting experience.

I would like to thank my father for his constant love and support, without which this thesis would have been impossible. Thank you Daddy, you are the best!!

I would like to thank my husband, Shantanu Roy. His constant motivation and positive criticism inspired me to learn from my failures and work towards my goal. Also, scientific discussions with him are acknowledged.

Last but not the least I thank God for always being there for me!!

# Curriculum Vitae

## Akshata Rao

Gujerstrasse 2  
Zürich 8050  
Switzerland  
Email: akshata.rao@mat.ethz.ch  
Ph : +41446336833  
Birhdate : March 18, 1982

Nanometallurgy  
ETH Zürich  
Wolfgang-Pauli-Str. 10  
Zürich 8093  
Switzerland  
Cell : +41787334291

## Education

- **University of Basel** Basel, Switzerland  
*PHD* Dec 2005- Dec 2009  
– Research Topic in PhD : **Controlled Manipulation of Nanoparticles : Scanning Probe Measurements and Modelling of Trajectories and Dissipative Effects**
- **University of Pune** Pune, India  
*M.Sc(PHYSICS)* 2005
- **Fergusson College, University of Pune** Pune, India  
*B.Sc(HONS. in PHYSICS)* 2002

## Publications

1. **Friction and Pathway fluctuations of spherical nanoparticles manipulated by tapping-mode AFM**  
*A. Rao*, M-L Wille, E Gnecco, K Mougín, and E Meyer,  
Phys. Rev. B **80**, 193405 (2009)
2. **Analytical relations between particles and probe trajectories in AFM nanomanipulation**  
*A. Rao*, E. Gnecco, D. Marchetto, K. Mougín, M.Schönenberger, S. Valeri and E. Meyer,  
Nanotechnology, **20**, 115706 (2009)
3. **Manipulation of Gold nanoparticles: Influence of surface chemistry, temperature, and environment (Vacuum versus Ambient Atmosphere)**  
K. Mougín, E. Gnecco, *A. Rao*, M. T. Cuberes, S. Jayaraman, E. W. McFarland, H. Haidara, and E. Meyer,  
Langmuir, **24**, (4), 1577-1581 (2008)
4. **Characterization of nanoparticles using the atomic force microscopy**  
*A. Rao*, M. Schoenenberger, E. Gnecco, Th. Glatzel, E. Meyer,  
Journal of Physics - Conference Series. **61**, 971976 (2007)
5. **Manipulation of rigid nanorods by atomic force microscopy**

E. Gnecco, **A. Rao**, G. Chandrasekar, K. Mougín, and E. Meyer, *Nanotechnology*, **21**, 215702 (2010).

**6. Manipulation of gold colloidal nanoparticles with atomic force microscopy in dynamic mode: influence of particle-substrate chemistry and morphology, and of operating conditions**

S. Darwich, K. Mougín, **A. Rao**, E. Gnecco, S. Jayaraman and Hamidou Haidara, *Beilstein J. Nanotechnol.*, **2**, 8598 (2011).

### Oral Presentation

- International Conference on Nanoscience and Technology (ICN&T 2006) Basel, Switzerland : Title - “Characterization and manipulation of gold nanoparticles”
- 2nd International Seminar on Teaching Scanning Probe Microscopy and Nanotechnology (TSPM+N2), 2006 organized by Nanosurf AG in Basel, Switzerland : title - “New experiments for students using AFM”
- 6th ESF Nanotribology Workshop, Santa Margherita di Pula, 2007, Sardinia (Italy) : Title - “Manipulation of nanoparticles on patterned silicon surfaces”
- Frontiers Workshop, Zermatt , 2007 : Title - “Hydrophobic Effects in Manipulating Au Nanoparticles ”
- Swiss Physical Society Meet, 2008, Geneva : Title - “Scanning probe scattering of gold particles on nanopatterned surfaces”
- ICTP-FANAS Meeting, Trieste, 2009 : Title - “Trajectory Fluctuations Accompanying the Manipulation of Nanoparticles”

### Poster Presentation :

- International Conference on Nanoscience and Technology (ICN&T 2006) Basel, Switzerland - Poster Title : “Characterization and manipulation of nanoparticles by atomic force microscopy”
- 5th ESF Nanotribology Workshop, 2006, Antalya, Turkey - Poster Title : “Manipulation of gold nanoparticles using the AFM”
- Swiss Workshop on Nanoscience, 2008, Davos - Poster Title : “New trends in Nanotribology : Scanning Probe Scattering”